Development of solid-state Fluoride-ion Batteries : cell design, electrolyte characterization and electrochemical mechanisms

Antonin Grenier

Thèse de doctorat

Pour l'obtention du grade de Docteur

de l'Université Pierre et Marie Curie

École doctorale de Chimie Physique et Chimie Analytique de Paris Centre
Laboratoire de physicochimie des électrolytes et nanosystèmes interfaciaux

Development of solid-state Fluoride-ion Batteries: cell design, electrolyte characterization and electrochemical mechanisms

Présentée par Antonin Grenier

Dirigée par Damien Dambournet et Henri Groult

Présentée et soutenue publiquement le 23 Mai 2016

Devant un jury composé de :

M.	Pr.	Mickaël	DOLLÉ	Rapporteur
M.	Pr.	Marc	DUBOIS	Rapporteur
M.	Dr.	Christian	JORDY	Examinateur
Mme.	Pr.	Christel	LABERTY-ROBERT	Examinatrice
Mme.	Dr.	Encarnación	RAYMUNDO-PIÑERO	Examinatrice
Mme.	Dr.	Virginie	VIALLET	Examinatrice
M.	Dr.	Damien	DAMBOURNET	Directeur de thèse
M.	Dr.	Henri	GROULT	Directeur de thèse

Table of contents

Acknowledgments

This thesis was carried out at the PHENIX laboratory of the University Pierre and Marie Curie, within the "*Électrochimie et Liquides Ioniques*" (ELI) team. I thank Pierre Levitz, the lab director, for welcoming me in the lab. I acknowledge the French National Research Agency (ANR) for their financing through the FLUOBAT project.

I would like to thank the members of the jury, and particularly the referees Mickael Dollé and Marc Dubois for their comments and their report, and thanks to Christian Jordy, Christel Laberty-Robert, Encarnación Raymundo-Piñero and Virginie Viallet for their involvement. Your input allowed me to take an additional step back and look at the overall picture.

Obviously, I would like to thank my tutors, Damien Dambournet and Henri Groult, with whom I have learned more about science and life than I ever could imagine before starting this thesis. Working on the Fluobat project was a process full of pitfalls but they were always there to support and encourage me. I sincerely hope I will have the opportunity to keep on working with them in the future.

I would also like to thank the whole ELI team of the lab for their benevolence. A few people deserve particular mentions: Didier Devilliers, with whom I have gladly shared an office for more than 3 years and who has been constantly available for assistance; Sandrine Leclerc, who helped me fit into the team and getting my bearings in my new work environment, and with whom it was a pleasure to work and laugh for the past years; Eric Mahé, for sharing some of his work space, which was almost life-saving in the last days before the relocation of the laboratory in May 2016; and last, but most certainly not least, I would like to express my deepest gratitude to Ana-Gabriela Porras-Gutierrez, whose helpfulness will be forever remembered. The two interns I worked with, Antoine Desrues and Ludivine Maurieres, also deserve my gratitude. It was a pleasure to work with them and I wish them the best of luck for the future, even though I am confident they will not need luck considering their talent.

Many thanks to José Gomes, the machinist/electrician/handyman/Inspector Gadget who largely contributed, amongst many other things, to the development of the development of the electrochemical cell presented in this manuscript.

My gratitude also goes towards to the (ex-)members of PHENIX (in a total disorder) with whom I shared many things, including a few chilled beverages for some of them (they will recognize

General introduction

The global warming generated by the emission of greenhouse gases due to the use of fossil energies has been a growing concern for human societies during the last century. We are now in 2016 and our CO_2 emissions will keep increasing for several decades according to the most optimistic prediction[a].

The 21st Conference of the Parties (COP21) held by the United Nation Framework of the Convention on Climate Change (UNFCCC) took place in late 2015 in Paris, 18 years after the COP3 and the adoption of the Kyoto Protocol in 1997. The COP21 lead to the adoption of the Paris agreement[b], recognizing that the climate change represents an urgent and potentially irreversible threat to human societies, necessitating deep reductions in global greenhouse gas emissions. This lead to multiple commitments of 195 nations, supported by their public and some of their private partners, to accelerate the decarbonization of our energy production by investing in research and development of clean energy innovations. In particular, the parties have set the target of keeping the rise in temperature well below 2 °C, with the ambition to retain it below 1.5 °C[c].

The improvement of energy storage systems is of crucial importance to reach the goals we have set. The growth of renewable sources, especially solar, wind and tidal energies, requires efficient storage methods. Indeed, these three types of renewable energies are inherently intermittent and to further implement those as major energy sources, efficient energy storage must completed. There exist myriads of techniques to store energy under various forms (chemical, electrical, mechanical, magnetic, potential, kinetic…) in order to return it when we need it the most. In this regard, electrochemical energy storage and conversion is of prime interest due to the relative high efficiency attainable, the versatility in the form and volume it can take, and the flexibility of the performances it can exhibit in function of the desired application.

This is particularly the case of rechargeable batteries, also named secondary batteries. These electrochemical devices can either be designed as massive high energy stacks for grid storage or as microbatteries in futuristic credit cards with flexible LCD screens. But they are better

---

[a] http://www3.epa.gov/climatechange/science/future.html

[b] http://www.cop21.gouv.fr/en/more-details-about-the-agreement/

[c] http://newsroom.unfccc.int/unfccc-newsroom/finale-cop21/

known for powering portable electronic devices such as (smart)phones, tablets, laptops, tools etc. They are also the most promising candidates to replace our vehicles' combustion engines by electric ones. Besides, they are already increasingly used as complementary energy source in hybrid electric vehicles. Although fuel cells may also appear as attractive contenders for electric propulsion, they are facing criticism in terms of efficiency, price and sustainability[d].

Many chemistries of secondary battery exist but only a few have been implemented commercially with success. For instance, lead-acid batteries, invented in 1859 by French physicist Gaston Planté, are still widely used for their low cost and high surge current required by automobile starter motors. Nevertheless, the market is largely dominated by the lithium-ion batteries (LIB) thanks to their superior energy density, even if it often comes at a higher price. The first Li-ion technology was first introduced by Sony in the early nineties thanks to the work of John Goodenough developing $LiCoO_2$[e] and Rachid Yazami developing graphite[f]. Today, commercial LIB still rely on the reversible insertion of lithium ions in the layered structure of host electrodes, the so-called rocking-chair batteries, and $LiCoO_2$ is now replaced by the safer $LiFePO_4$[g].

However, what is of increasing concern is the limited availability of lithium resources in the long-term. Indeed, lithium is only present to trace levels in Earth's crust and in the sea[h], and its extraction is highly expensive. It is extracted from lithium minerals or salts (brines), the majority coming South America, Australia and China[i]. In the event of a large implementation of lithium batteries in the automotive industry, and considering the increasing demand of portable electronics, it remains unsure if worldwide lithium reserves will be sufficient to supply the demand in the upcoming decades. Although, it is believed that the establishment of proper recycling networks could be sufficient to supply this demand.[j] What remains quite alarming is the possible skyrocketing prices of lithium-based materials.

---

[d] https://en.wikipedia.org/wiki/Fuel_cell_vehicle#Criticism (*January 2016*)

[e] K. Mizushima, P. C. Jones, P. J. Wiseman and J. B. Goodenough, *Mater. Res. Bull.*, 1980, **15**, 783–789.

[f] R. Yazami and P. Touzain, *J. Power Sources*, 1983, **9**, 365–371.

[g] A. Padhi, K. Nanjundaswamya and J. Goodenough, *J. Electrochem. Soc.*, 1997, **144**, 1188–1194.

[h] T.G. Goonan, 2012, Lithium use in batteries: U.S. Geological Survey Circular 1371, 14 p.

[i] D. Bradley, B. Jaskula, 2014, Lithium—For harnessing renewable energy: U.S. Geological Survey Fact Sheet 2014–3035, 2 p., *http://dx.doi.org/10.3133/fs20143035*.

[j] J.-M. Tarascon, Is lithium the new gold? *Nat. Chem.* **2,** 510 (2010).

This statement justifies the need to develop a panoply of battery chemistries relying on cheap and abundant materials which will allow our modern societies to progressively decarbonize our energy and cope with our growing energy demand.

In this regard, fluoride-ion batteries (FIBs) are promising candidates within the frame of the development of new battery concepts with high energy densities. Indeed, new battery systems must deliver/store higher energy at low cost and low weight, in particular for mobile applications. The chemistry of FIBs relies on the shuttle on the fluoride ion F^- between a metal and metal fluoride electrode, through a fluoride-ion conducting solid electrolyte. In other words, fluoride anion acts as the charge transfer ion during the charge/discharge procedure. These reactions can be seen as conversion reactions since they are multi-electronic processes and do not rely on the insertion of F^-. Coupled with the large change in free energy allowed by the high electronegativity of the fluoride ion, they offer outstanding theoretical energy densities. Values above 1500 $Wh.kg^{-1}$ or 5000 $Wh.L^{-1}$ can be calculated for some of the best electrode combinations.

Although the study of these electrochemical systems first started in the seventies upon the development of fast fluoride conducting electrolytes, in 2011, a scientific publication demonstrated the proof of concept of reversible fluoride cells.[k] Consequently, the interest for such systems was renewed and the French National Research Agency (ANR) decided to financially support this original and innovative program focused on the possible use of such F-ion batteries instead of Li-ion batteries. The project involves 4 academic laboratories and 2 industrial partners: SAFT and Solvay and is entitled FLUOBAT (Batteries tout solide à ions fluorures). The program enabled me to perform this thesis carried out at the "*Physicochimie des électrolytes et nanosystèmes interfaciaux*" (PHENIX) laboratory at the Pierre and Marie Curie University.

As emerging battery chemistries, the advance of such electrochemical systems is faced with severe challenges that will be discussed to some extent in this thesis work.

This manuscript is divided into four chapters:

---

[k] M. Anji Reddy and M. Fichtner, *J. Mater. Chem*, 2011, **21**, 17059.

The first chapter provides a bibliographic overview of FIBs and reviews the challenges inherent to the study of such systems. First, generalities and fundamental notions of battery operation are given and applied to the study of FIBs. Analogies with LIBs will be useful to illustrate the challenges met by the operation of solid-state systems, particularly FIBs. The preparation of the electrode and the effect of the electrochemical reactions on its integrity will be particularly discussed. This knowledge will then be applied to review the state of the art of FIBs. Finally, the need to develop a reference electrode adapted to the study of FIBs will be discussed to conclude this chapter.

The second chapter is dedicated to the electrolyte. Fundamental notions explaining the electrical conductivity in solids will be used to review the use of Ba-doped LaF_3, $La_{1-x}Ba_xF_{3-x}$, the fluoride-conducting solid electrolyte used in modern FIBs. The electrical properties of $La_{1-x}Ba_xF_{3-x}$ (LBF) are studied using electrochemical impedance spectroscopy. The influence of an addition of carbon on the electrical properties and electrochemical activity of the electrolyte is investigated using lithium as counter electrode. The results suggest the possible formation of carbon fluoride due to the interaction of carbon with fluoride ions and bring new insights on the mechanisms underlying the operation of FIBs.

The third chapter describes the development of an electrochemical cell which allowed the operation of FIBs at elevated temperature. The rapid and easy modification of traditional coin-cells with high-temperature epoxy resin allows hermetical sealing for long period of time. The modified-cells can then be conveniently investigated under air thanks to a custom made electrochemical test bench placed in an oven. Experimental results on a symmetrical cell employing a mixture of Bi and BiF_3 illustrate the hermetical sealing of the modified coin-cells.

The fourth and last chapter focusses on the investigation of the electrochemical reaction taking place in a symmetrical cell employing a mixture of Bi and BiF_3 as electrode. Atomic pair distribution function is used to probe the local and intermediate range structure of the materials before and after operation of the FIB. Results bring new insights on the electrochemical mechanisms involved in the operation of FIBs. The good reversibility obtained for such electrode opens a new way in the development and study of other electrode materials for FIBs.

Chapter I. Fluoride-ion batteries: introduction and state of the art

To understand the challenges inherent to the study of fluoride-ion batteries (FIBs), it is necessary to put into perspective how battery research is usually being done. In order to do so, the basic concepts and operation of batteries are explained and applied to FIBs. When it is relevant, physico-chemical analogy with the study on lithium-ion batteries (LIBs) will be done to shed light on some challenging aspects of FIBs.

Then, the state of the art of FIBs will be presented, accompanied by focusses on details that will be relevant to the following chapters, such as the need of a reference electrode.

Please note that the primary focuses of this chapter are the general properties of FIBs with an emphasis on the electrochemical reactions and the properties of the electrode. Chapter II is almost entirely dedicated to the electrolyte and most points discussed about the electrolyte in this chapter will be further discussed in **Chapter II**.

The electrochemical mechanisms on which FIBs rely are still unclear, and one of the objectives of this thesis is to clarify those mechanisms. Therefore, the reaction mechanisms that can be found in current LIBs, i.e. insertion and conversion reactions, will be presented and discussed for FIBs.

Finally, the fundamental notions and performances of batteries applied to fluoride ion batteries will be presented.

1. Generalities and fundamental notions

The working principle of FIBs is first exposed. To facilitate the comprehension of the state of the art, fundamental notions (e.g. potential, capacity, energy), including thermodynamic considerations, are presented and applied to FIBs.

1.1. Definition and working principle

1.1.1. Definitions and basic concepts

A battery is an electrochemical device that allows conversion of the chemical energy into electrical energy. The most common classification of battery is dictated by their ability to be recharged or not. A primary battery is non rechargeable. After discharge, it is not possible to

recharge it as the electrochemical reactions taking place are irreversible, and the battery is discarded. A secondary battery is rechargeable and several charge discharge cycles can be performed until significant loss of performance is experienced.

Strictly speaking, a battery is a package constituted of one or more electrochemical cells that are in series and/or in parallel. For instance, in a typical LIB used in laptops, the Li-ion cells are in series or parallel to modulate the battery's output voltage and capacity, respectively. Some batteries can be constituted of a single cell, such as the well-known AA alkaline batteries for instance. For this reason they are often referred as AA cells.

An electrochemical cell, or galvanic cell, is composed of two half cells, each composed of an electrode in contact with an electrolyte. The conversion of the energy from chemical to electrical is made possible through electrochemical reactions also called redox (contraction of reduction-oxidation) reactions taking place simultaneously at the cathode and anode. These chemical reactions take place in the bulk, or at the surface, of the electrodes which are in contact with the electrolyte, and generate electricity (electrons) that is directed in the external circuit, connected to the appliance. The electrolyte is an ionic conductor. It ensures the shuttling of ions from one electrode to the other during the discharge or charge processes, and must be electronically insulating to avoid short-circuits. In a LIB, the electrolyte ensures the movement of the lithium ion Li^+. In a FIB, it is the fluoride ion F^- that is transported in the electrolyte. The concept of FIBs will be further detailed in the next section.

Another difference that will be of particular interest in this manuscript is the "state" of the battery, usually defined by the liquid state or solid state in which the electrolyte can be found. On one hand, most of battery technologies use liquid electrolytes and are therefore generally referred as *conventional batteries*. On the other hand, solid-state batteries are composed of solid electrolytes. *All-solid-state batteries*, like the FIBs on which this manuscript focusses, are solely composed of solid materials for both the electrolyte and the electrodes. This particular solid configuration leads to some advantages, notably in terms of security, as the risk of leakage or short-circuit can be easily avoided. However, they present serious challenges like for instance the lower ionic conductivity of the solid electrolyte, or the large volumetric variations expected to be observed upon cycling.

1.1.2. Working principle

The FIBs studied in this thesis are classified as all-solid-state batteries. For this reason, a FIB's electrode contains solid electrolyte. (N. B.: The purpose of adding electrolyte in the electrode is addressed in **2.1.1.2. S**uch approach does not apply to microbatteries.)

One of the key components of the battery is the *active material* (AM) which allows producing electrical energy through redox reactions. In FIBs, the AM is either a metal (M) or a metal fluoride (MF_x) or even a mixture of both. They undergo redox reactions within the electrode to yield electrons (e^-) or fluoride ions (F^-) as presented in **Figure I.1**.

Upon discharge, the metal fluoride cathode MF_x (positive electrode) undergoes reduction while the metal anode M' undergoes a simultaneous oxidation according to the reactions presented below.

<div align="center">Discharge</div>

At the cathode :	$MF_x + xe^- \rightarrow M + xF^-$	1.
At the anode :	$M' + xF^- \rightarrow M'F_x + xe^-$	2.
Total :	$M' + MF_x \rightarrow M'F_x + M$	3.
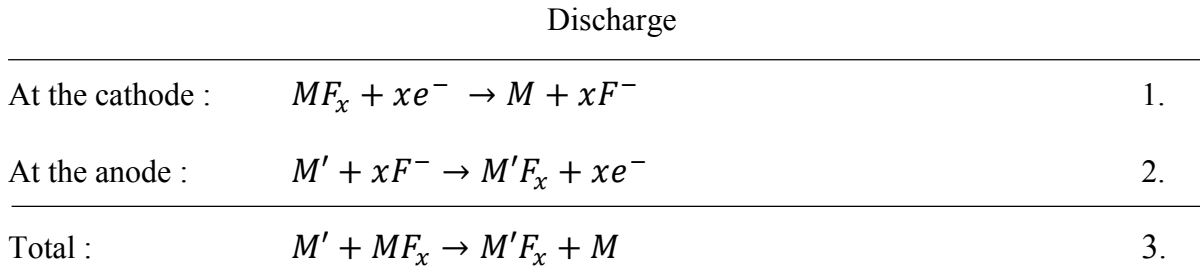
The fluoride ions flow through the electrolyte while a similar charge of electrons passes simultaneously through the external circuit. Upon charge, the reactions occur in the opposite direction. The previously reduced metal M (positive electrode) is now the anode and undergoes oxidation to yield back the metal fluoride. Simultaneously, the previously oxidized $M'F_x$ is now the cathode and undergoes reduction to yield back its corresponding metal M'.

<div align="center">Charge</div>

At the anode :	$M + xF^- \rightarrow MF_x + xe^-$	4.
At the cathode :	$M'F_x + xe^- \rightarrow M' + xF^-$	5.
Total :	$M'F_x + M \rightarrow M' + MF_x$	6.
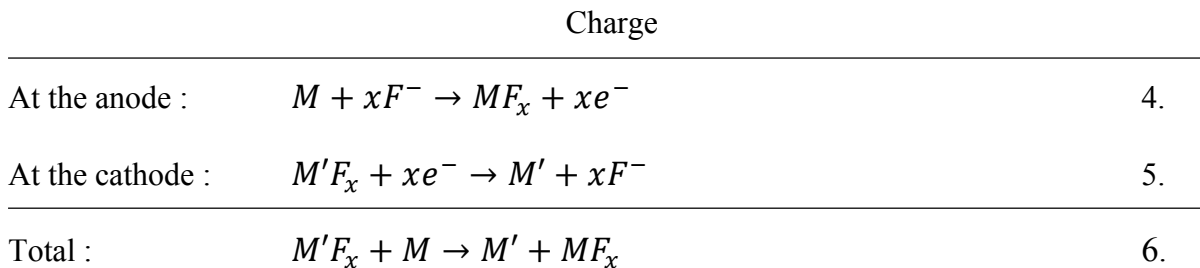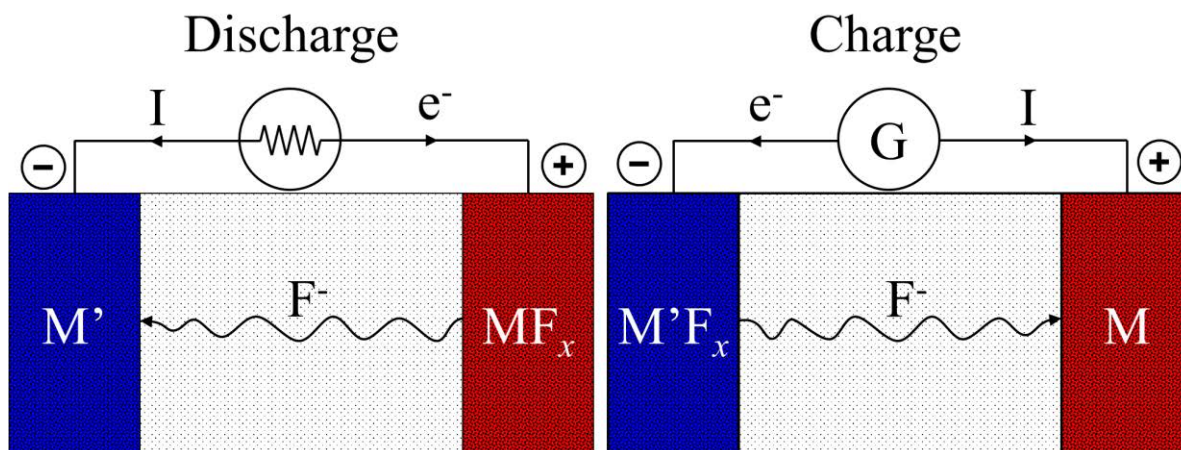
Figure I.1. *Illustration of a fluoride-ion battery upon discharge (left) and charge (right).*

The anode is always associated to the oxidation process while the cathode is always associated to the reduction process. In a secondary battery, during successive discharge and charge processes, each electrode is alternatively the anode and the cathode. To distinguish the electrodes, one must observe the potential of their respective redox reactions. The electrode with the higher potential will be called the positive electrode and the other electrode the negative. This concept will be further explained in section **1.2.1**.

In the above equations (1→6), *x* indicates the number of fluoride ions exchanged per mole of metal ion and is consequently indicative of the oxidation state of the metal. These reactions are only applicable if the metal ions do not oxidize or reduce to intermediary oxidation states (i.e. $M^{3+} \leftrightarrow M^{2+}$, $M^{2+} \leftrightarrow M^{+}$ etc). For example, in the case of FeF_3 (Fe^{3+}), one can imagine an intermediary FeF_2 (Fe^{2+}) step before the full reduction to Fe°, as in LIBs[1]. Equation 1 would then be written as follow:

At the cathode: $\qquad MF_y + xe^- \rightarrow MF_{y-x} + xF^- \qquad\qquad$ 7.
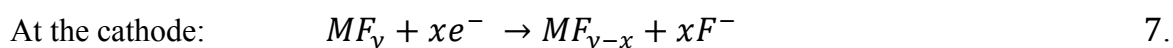
With $2 \leq y \leq 5$ and $1 \leq x \leq 4$, even if assembly of practical cells with MFy (y ≥ 4) could be extremely delicate, as MF_4's and MF_5's are in most cases metastable, powerful oxidizing agents, and liquid, gaseous or extremely volatile at room temperature and ordinary pressure.

1.2. Fundamental notions

1.2.1. Theoretical cell potential – thermodynamic considerations

The calculation of the theoretical cell potential of a redox reaction is useful to assign redox reactions to experimental results. The cell potential or cell voltage E (expressed in Volts) is determined by the potential difference ΔE between the redox couples that are involved in each half-cell:

$$\Delta E = E_+ - E_-$$
<div align="right">8.</div>

where $E_{positive}$ and $E_{negative}$ are the potential of the positive and negative electrodes, respectively. This potential difference is sometimes referred as the electromotive force (emf) as the motion of electrons through the external circuit rises from this potential difference. Since tables of thermodynamic properties are given in the standard state, calculation of theoretical cell potential are done assuming the standard state (298 K, 1 bar). When the conditions are other than in the standard state, the potential is given by the Nernst equation:

$$E = E^0 + \frac{RT}{nF}\ln\frac{(ox)}{(red)}$$
<div align="right">9.</div>

Where (ox) and (red) are the activities of the redox species, R is the gas constant, T the absolute temperature and E^0 the standard potential. If the redox species are pure solids (i.e. not alloys or solid solutions), the electrode potential can be roughly estimated to the standard potential, as the activity of pure solids is unity. The standard potential of a cell is linked to the change of standard free energy, also called Gibbs free energy, ΔG^0 according to the follow equation:

$$\Delta G^0 = -nF\Delta E^0$$
<div align="right">10.</div>

where n is the number of moles of electrons exchanged and F the Faraday's constant ($F = 96485\ C.mol^{-1}$). Finally, ΔG^0 is linked to the standard enthalpy change ΔH^0 and standard entropy change ΔS^0 by the formula:

$$\Delta G^0 = \Delta H^0 - T.\Delta S^0$$
<div align="right">11.</div>

It is thus possible to calculate the theoretical cell potential, at 298 K, for various redox couples by knowing their standard enthalpy of formation $\Delta_f H^0$ and standard entropy S^0 of their respective fluorides.

$$\Delta H^0 = \sum n\ \Delta_f H^0_{products} - \sum m\ \Delta_f H^0_{reactants}$$
<div align="right">12.</div>

$$\Delta S^0 = \sum n\, S^0_{products} - \sum m\, S^0_{reactants} \qquad\qquad 13.$$

Where n and m are the stoichiometric coefficients of the relevant species. Values of $\Delta_f H^0$ and S^0 can be found in reference tables for most inorganic fluorides.

Even if experimental potentials sometimes differ from the calculated ones, the latter remain very useful to determine the most interesting redox couples that could deliver the highest cell voltage.

These thermodynamic considerations are also of interest to calculate the decomposition potential of some solid fluoride electrolytes (e.g. PbF_2, LaF_3) as discussed in **Chapter II.3.5**.

1.2.2. Effect of current on the cell potential

The equilibrium potential of a cell is defined in open circuit conditions (i.e. no electrons move through the external circuit). It is identically referred as the open circuit potential or open circuit voltage (denoted OCP and OCV, respectively).

In our case, the OCP observed before operation of the cell is usually close to the $\Delta E°$ corresponding to the two redox couples (one redox couple present at each electrode). This cell voltage can typically be measured by a voltmeter, or in our case, with a potentiostat. In these conditions, no ions move through the electrolyte and no chemical reactions take place in the electrodes. Strictly speaking, there is only a little current that flows through the external circuit through the high impedance voltmeter. However, this little charge exchange doesn't induce any relevant change in the potential of the electrodes and the OCP thus remains substantially constant.

1.2.2.1. Potential-composition dependence

Upon polarization of the cell, which is generally done through the application of a constant current (i.e. galvanostatic experiments), electrons are allowed to flow through the external circuit. Charge neutrality is achieved by ions simultaneously flowing through the electrolyte. In the case of pure solids, the cell potential will remain constant to a value close to the potential difference given by the redox couples present at the electrodes. This is characterized by a voltage plateau, as illustrated by **Figure I.2**.

In the case of alloys or solid solutions, the potential will vary with the change in composition created by the electrochemical reactions taking place at the electrode. This behavior is characterized by a pseudo plateau (i.e. with a slope) in the potential-composition curve. Since

discharge or charge experiments are usually performed under constant current, composition of the electrode is dependent on the time, so that the potential-time curve will also exhibit this slope.

The plateau will remain present as long as some redox species available for reaction are available at the electrode. At some point, all redox species are consumed and the cell voltage drops dramatically.
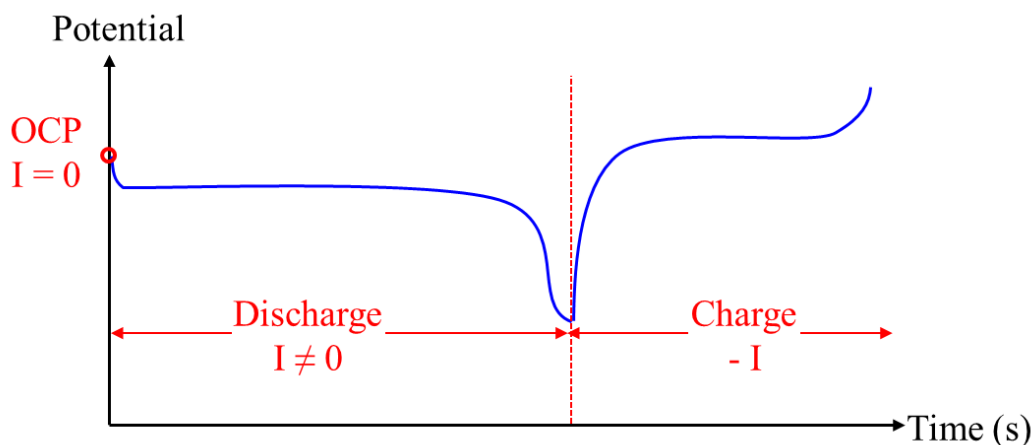
Figure I.2. *Schematic representation of a galvanostatic discharge/charge curve.*

During discharge, the potential decreases towards 0 V. At 0 V, both electrodes have the same potential and no energy can be extracted from the cell anymore. Upon charge, the inverse reactions take place, and the difference in potential of the electrodes increases. Both discharge and charge curves exhibit pseudo-plateaus characteristic of an electrochemical reaction.

1.2.2.2. Voltage efficiency, overpotential and ohmic drop

The cell's voltage efficiency depends on the electrodes overpotentials and the ohmic drop. It is characterized by a difference between the potential at which the electrochemical reactions should theoretically occur, $\Delta E_{I=0}$, as defined by thermodynamics, and the potential at which the electrochemical reactions are experimentally observed, $\Delta E_{I\neq0}$.

$$\Delta E_{I\neq0} = \Delta E_{I=0} - \eta_a - |\eta_c| - IR \qquad\qquad 14.$$

with η_a and η_c the anodic and cathodic overpotentials, and IR the ohmic drop. Electrode overpotentials rise from a variety of electrochemical and chemical processes, such as the activation energy of the electrochemical reactions. The ohmic drop is defined as the product of the current applied on the cell and its overall resistance, which is the sum of the resistances

present in the cell R_{cell} (e.g. electrolyte and interfaces) and the experimental setup R_{setup} (e.g. current collectors, connectors and current leads).

$$R = \sum R_{cell} + \sum R_{setup} \qquad\qquad 15.$$

The IR drop is almost instantaneous. Upon polarization, the output voltage will suddenly drop proportionally to this resistance. This reduction of the output voltage is proportional to the current, according to Ohm's law:

$$V = R.I \qquad\qquad 16.$$

Both phenomena are illustrated by **Figure I.3**.
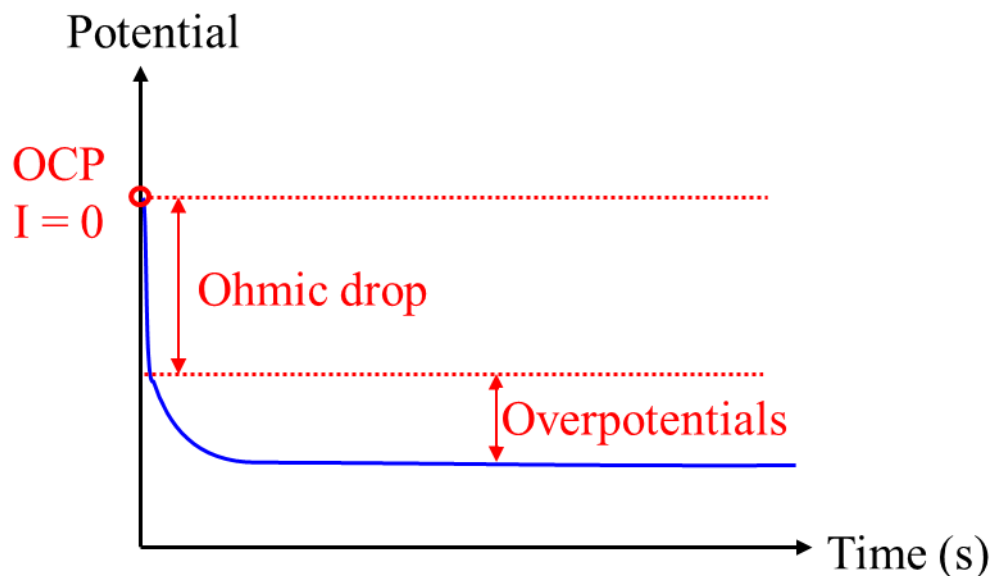
Figure I.3. *Schematic representation of the beginning of a discharge curve exhibiting the effect of the ohmic drop and electrode overpotentials on the discharge potential.*

Similar phenomena occur during charging. Generally, in all-solid-state batteries such as our FIBs, the contribution of resistances coming from the setup (typically about a few dozen ohms) to the overall resistance is negligible compared to that of the electrolyte (typically about several hundred ohms). This phenomenon alone justifies the need to develop electrolytes with high conductivity reaching those of liquid electrolytes. It also justifies the use of heightened temperatures as the conductivity of a solid electrolyte increases with increasing temperature following Arrhenius' law, as will be discussed in **Chapter II**.

It is also of crucial importance to maintain the integrity of the electrode-electrolyte and electrode-current collector interfaces during operation of the battery. The degradation of the interface during cell operation leads to a dramatic increase of the ohmic drop which can eventually render the cell inoperable.

1.2.3. Cell capacity

For an electrochemical cell, the capacity Q (Ah) is the quantity of electric charges stored in the cell. It can be expressed by Faraday's law as the quantity of charges exchanged for a certain period of time:

$$Q = \int_0^t I(t)dt \hspace{8cm} 17.$$

Where I is the current (A) and t the time (h). In the case of a constant current experiment, as it is the case in galvanostatic experiments, this expression can be reduced to:

$$Q = I.t \hspace{9cm} 18.$$

1.2.3.1. Specific capacity

It is convenient to express the specific capacity which is the capacity per gram or volume of equivalent. Two terms are typically employed, the specific gravimetric capacity Q_m (Ah.g^{-1}) or the specific volumetric capacity Q_v (Ah.cm^{-3})

$$Q_m = \frac{Q}{m} \hspace{8.5cm} 19.$$

$$Q_v = \frac{Q}{v} \hspace{8.7cm} 20.$$

$$Q_v = Q_m.\rho \hspace{8.3cm} 21.$$

With m the mass (g), v the volume (cm^3), and ρ (g.cm^{-3}) the volumetric mass density of the active material, the electrode, or even the whole cell. The notion of specific capacity is however generally used to compare the performance of active materials.

Finally, it is important to note that for kinetic reasons, the experimental capacity of a battery depends on the discharge rate which is defined by the extent of the current applied.

1.2.3.2. C-rate

This raises the notion of C-rate. A 1C discharge rate would deliver the rated capacity in 1h, 2C in 30 min and 60C in 1 min. A C/2 discharge rate would deliver the rated capacity in 2h, C/10 in 10 hours.

This is convenient to classify battery chemistries when the experimental capacity of the battery is known. These notions can however be applied to theoretical capacities. The C-rate will then define at which rate the battery will be charged or discharged considering the theoretical capacity of the active material contained in one electrode.

Due to the relatively low conductivity of the electrolyte, and to maximize the capacity for further characterization purposes, typical C-rates in FIB are well below C/100 (0.01 C).

1.2.3.3. Theoretical capacity

The theoretical specific capacity (capacity per unit of mass, also called gravimetric capacity) $Q_{th,m}$ (mAh.g^{-1}) of an active material can be calculated using the following relation:

$$Q_{th,m} = \frac{F.n_{e^-}}{3.6M}$$
22.

With F is the faraday constant (F = 96485 C.mol^{-1}), n_{e^-} the theoretical number of moles of electron exchanged, and M is the molar mass of the active material. The coefficient of 3.6 is used here to convert the capacity in Coulomb (C) to milliampere-hour (mAh). In a FIB, n is directly related to the expected change in valence of the metal or metal fluoride studied and can be considered as such.

It is also possible to calculate the theoretical volumetric capacity $Q_{th,v}$ (mAh.cm^{-3}) knowing the volumetric mass density ρ (g.cm^{-3}) of the active material.

$$Q_{th,v} = Q_{th,m} \cdot \rho$$
23.

The theoretical specific capacity of some materials is reported on **Table I.1**. Looking at the capacities, materials constituted from elements presenting low molar masses are naturally interesting candidates as active materials for FIBs and for batteries in general, as they store more capacity for a fixed amount of mass. However, they are not necessarily promising for FIBs as their corresponding fluoride can be insulating from both an ionic and electronic point of view, like LiF for instance.

	M (g.mol^{-1})	Valence variation	Q$_{th,m}$ (mAh.g^{-1})
C	12.0	1	2233.4
CF	31.0	1	864.3
Li	6.9	1	3861.3
LiF	25.9	1	1033.2
Ca	40.1	2	1337.5
CaF$_2$	78.1	2	686.6
La	138.9	3	578.8
LaF$_3$	195.9	3	414.4
Ce	140.1	3	573.8
CeF$_3$	197.1	3	407.9
Bi	209.0	3	384.7
BiF$_3$	266.0	3	302.3
Mg	24.3	2	2205.4
MgF$_2$	62.3	2	860.4
Mn	54.9	2	975.7
MnF$_2$	92.9	2	576.8
MnF$_3$	111.9	3	718.3
Fe	55.8	2	479.9
FeF$_2$	93.8	2	571.2
FeF$_3$	112.8	3	712.5
Cu	63.5	2	421.8
CuF$_2$	101.5	2	527.9
Pb	207.2	2	258.7
PbF$_2$	245.2	2	218.6

Table I.1. *Theoretical specific capacities of some metals and metal fluorides to be used as active materials in FIBs.*

It is convenient to express the theoretical capacity of a cell from the combination of its two electrodes' active material capacity:

$$Q_{th}(M'/MF_x) = \frac{1}{\frac{1}{Q_{th}(M')} + \frac{1}{Q_{th}(MF_x)}}$$

24.

The theoretical capacity of the cell can then be used to calculate the theoretical energy.

1.2.4. Cell energy density and power

The specific energy $\varepsilon_{th,m}$ (Wh.kg^{-1}) and energy density $\varepsilon_{th,v}$ (Wh.cm^{-3}) correspond to the amount of electrical energy stored in the cell per unit mass or volume, respectively. The theoretical specific energy is the product of the cell voltage by the specific capacity.

$$\varepsilon_{th,m}(M'/MF_x) = E°.Q_{th,m}(M'/MF_x)$$

25.

Table I.2 shows the calculated potential, specific capacity and specific energy of some cell reactions that will be relevant in the state of the art section or experimental results. Negative potentials signify that the cell reaction is not spontaneous and can therefore be considered as cells being in the discharged state. Negative values of specific energy should not be considered as such, only their absolute value is meaningful.

The table does not necessarily represent the most interesting electrode combinations. Such approach has already been undertaken by the work of Gschwind *et al.*[2]. Still, the theoretical specific energies presented in this table make FIBs attractive systems for the long term replacement of current lithium technologies. For comparison, the theoretical specific energy of conventional Li-ion batteries is around 580 Wh.kg^{-1} for commercial systems (e.g. $LiFePO_4$), and that of Li-air is about 11,680 Wh.kg^{-1}[3],[4].

Cell reaction	$\Delta E°$ (V)	$Q_{th,m}$ (mAh.g^{-1})	$\varepsilon_{th,m}$ (Wh.kg^{-1})
$Bi + LaF_3 \rightarrow La + BiF_3$	-2.827	198.6	-561.5
$3\ Mn + 2\ LaF_3 \rightarrow 2\ La + 3\ MnF_2$	-1.558	288.9	-450.2
$3\ Mg + 2\ LaF_3 \rightarrow 2\ La + 3\ MgF_2$	-0.178	346.0	-61.5
$2\ Bi + 3\ MnF_2 \rightarrow 3\ Mn + 2\ BiF_3$	-1.269	230.8	-292.9
$2\ Bi + 3\ MgF_2 + \rightarrow 3\ Mg + 2\ BiF_3$	-2.650	265.9	-704.4
$2\ C + MnF_2 \rightarrow Mn + 2\ CF$	-2.636	458.4	-1208.5
$2\ C + MgF_2 \rightarrow Mg + 2\ CF$	-4.008	621.1	-2489.4
$3\ C + BiF_3 \rightarrow Bi + 3\ CF$	-1.367	266.3	-364.0
$3\ Li + LaF_3 \rightarrow La + 3\ LiF$	0.415	371.0	153.8
$Pb + CuF_2 \rightarrow Cu + PbF_2$	0.722	173.6	125.3
$3\ Pb + 2\ BiF_3 \rightarrow 2\ Bi + 3\ PbF_2$	0.369	139.4	51.5
$Ce + BiF_3 \rightarrow Bi + CeF_3$	2.832	198.0	560.8
$2\ Ce + 3\ CuF_2 \rightarrow 3\ Cu + 2\ CeF_3$	3.185	275.0	875.7
$2\ Ce + 3\ SnF_2 \rightarrow 3\ Sn + 2\ CeF_3$	2.323	214.3	497.8
$3\ Ca + 2\ BiF_3 \rightarrow 2\ Bi + 3\ CaF_2$	3.199	246.6	788.8

Table I.2. *Theoretical potential, specific capacity and specific energy for various cell reactions. The potentials were calculated using thermodynamic data collected from materialsproject.org, except for CF (Valerga et al.[5]) and SnF$_2$ (OECD chemical thermodynamics[6]).*

The specific power P_m (W.kg^{-1}) is the rate at which the cell can be discharged. It depends on the experimental conditions and cannot be theoretically calculated. Considering the state of advancement of FIBs, with the relatively low conductivity of the electrolyte, and no real optimization of the electrode composition, very low values are expected. Similar considerations are made for the volumetric power P_v (W.cm^{-3}).

It is important to emphasize that these theoretical values are superior to the experimental observations. For instance, LiCoO$_2$ has a theoretical specific energy of 1041 Wh.kg^{-1} while the typical value observed in commercial systems is 551 Wh.kg^{-1} [3] (for an average voltage of 3.8 V.)

These calculations (specific energies) are useful to compare active materials and demonstrate the attractiveness of FIBs, but are of a little relevance for most practical devices. Indeed, the FIBs contain various additives that greatly influence the total mass or the volume of the cell.

2. Electrodes for fluoride ion batteries

Electrodes for battery application are rarely composed of a single material. Various additives are needed to ensure efficient operation of the cell upon successive charge-discharge cycles.

2.1.1. Electrode composition

Excluding microbatteries, where electrodes are only a few micrometers thick and the active material can therefore be used alone, electrodes for solid state devices can be seen as composite materials. These composites are multifunctional architectures where electronic and ionic transport must be achieved in order for the redox reactions to occur in the bulk of the electrode (**Figure I.4**.)

Unlike conventional batteries where the liquid electrolyte wets the electrode porosity to ensure ionic conductivity, addition of electrolyte in the electrode is required to ensure the transport of fluoride ions through the electrode. In a similar manner, an electronic additive such as carbon is necessary to create electronic percolation within the electrode.
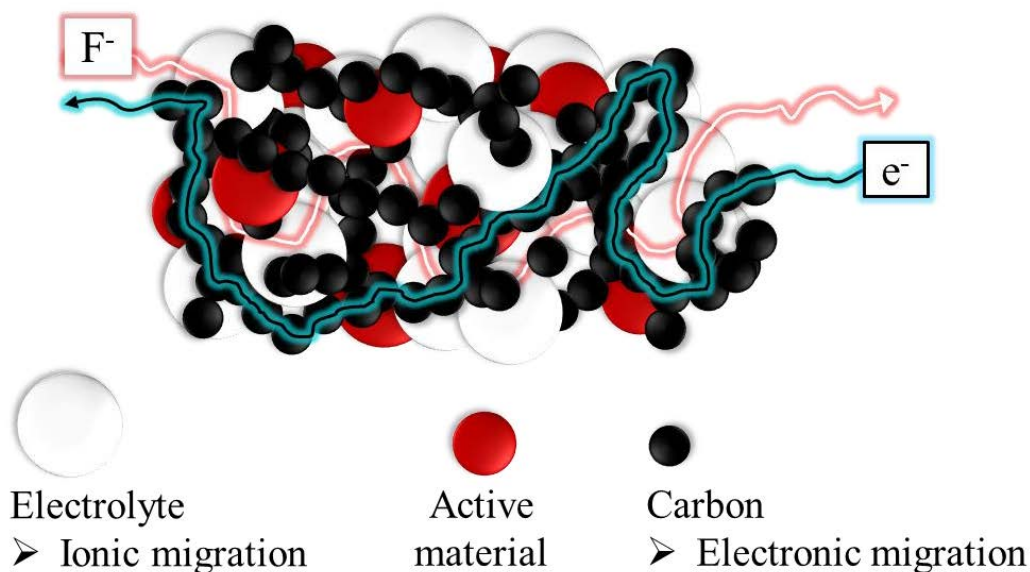
Figure I.4. Schematic representation of a composite electrode where both electrolyte and carbon must be present to ensure ionic and electronic percolation throughout the electrode.

2.1.1.1. Electronic conduction in the electrode

The electronic additive used in electrode composites is generally carbonaceous materials which can be found under various forms:

- carbon black
- graphite
- carbon nanotubes
- graphene

The carbon additive ensures the migration of the electrons through the electrode, to the current collector. The electrons gathered by the current collector can then flow through the external circuit. Transport of electrons within the bulk of the electrode is referred as electronic percolation.

It is crucial that a sufficiently large quantity of carbon is added to ensure the percolation of the electrons throughout the electrode. If an insufficient quantity of carbon is employed, electronic conduction pathways will not be provided, and electrons will not be able to reach the active material. The minimum quantity of carbon for which percolation is achieved is called the electronic percolation threshold. The electronic percolation of a composite electrode is

characterized by a steep increase of the measured electrical conductivity of the composite in function of the quantity of carbon present in the composite.

The addition of carbon is particularly important when metal fluorides are used as active material since metal fluorides are generally electronic insulators due to their large band gaps (e.g. ≈ 6 eV for LaF_3). Even if the active material is in its metallic state and can therefore ensure electronic conduction by itself, it will then become partially or totally insulating upon successive charge/discharge cycles.

2.1.1.2. Ionic conduction in the electrode

The movement of electronic charges through the external circuit is balanced by the movement of the ionic charges through the electrolyte. It is thus necessary to ensure the ionic migration within the electrode, to the active material. Indeed, the redox reactions are expected to occur at the three-phase junction where both ion and electron transport are achieved. As previously mentioned, the ionic conductivity is ensured by the wetting of the electrode porosity by the liquid electrolyte in a conventional cell. In an all-solid-state cell, it is the solid electrolyte that ensures this ionic conductivity.

For the same reason as to why electronic additive must be added to a metal-based electrode, electrolyte must also be added to the metal-fluoride-based composite electrode, even if the active material also shows ionic conductivity properties. Indeed, the active material which can be at first a fluoride conductor (e.g. BiF_3 [7]) will be rendered insulative (from an ionic perspective) upon reduction to its metallic state (i.e. Bi). Further charging might be impossible as no ionic conduction pathways will be available anymore.

Such approach implies that the electrolyte is electrochemically stable and does not decomposes (i.e. electrolysis of the electrolyte). Consequently, studies about all-solid-state batteries generally address the electrochemical stability of the relevant solid electrolyte. Chapter II, dedicated to the study of solid fluoride electrolytes, will particularly address this issue.

2.1.1.3. Fabrication of the electrode

In the simplest approach, the mixture is thoroughly mixed to obtain a fine dispersion of each component. Sufficient quantities of electrolyte and carbon must be added to the active material in order to reach the ionic and electronic percolation thresholds.

Ball-milling is a common method to obtain such mixtures at the nanometer scale, but careful considerations must be taken in terms of reactivity between each component as the process can

be quite energetic for high rotational speeds. In a typical ball-milling setup, the powder is placed in a sealed bowl with the milling balls, and the bowl is spun at a defined rotational speed. The impact force generated by the movement of the balls within the bowl has for effect to break the particles or agglomerates of the solid materials. This process can notably be used in so-called mecanosynthesis to produce nanomaterials such as doped solid electrolytes, as will be further discussed in **Chapter II**.

The finely dispersed powder can then be processed in various manners to obtain the desired structure. Continuing in our simple approach, cold pressing of the powder to form a compact pellet is sufficient to perform electrochemical investigations. Obviously, the electrode architecture is one of the key factors to enhance the battery's performance. Ball-milling associated with cold-pressing is a fast and easy way to produce all-solid-state batteries but does not provide much control over the obtained structure. More complex approaches can be employed to better control the architecture of the electrode and optimize the electrochemical performance of the cell. Some of them will be quickly discussed at the end of this chapter. Considering the early stage of advancement of FIBs, and considering that the objective is to try to clarify the electrochemical mechanisms taking place in the FIB, the milling/cold pressing approach was chosen.

To understand the electrochemical reactions that may take place in FIBs, it may be interesting to present the different types of possible electrochemical reactions occuring in LIBs.

2.1.2. Conversion reactions

Most commercial LIBs rely on the insertion and deinsertion of lithium ions in the host structure of the active material. The insertion reactions are also called intercalation reactions. The most typical insertion material is graphite, where Li ions are inserted between the graphene layers. Upon Li insertion/extraction, the layered host structure suffers only mild volumetric variations so that no major modification of the pristine structure is observed (at least for a few cycles). Similar insertion reactions can be observed with layered oxides/phosphates such as $LiCoO_2$/$LiFePO_4$.

However, materials that do not present layered structures are still capable of reacting with Li ions. This is the case of some metals or semi-metals (e.g. Sb, Sn, Si) that can form alloys with lithium. These electrochemical reactions are generally referred as alloying reactions.

Nanosized transition metal oxides or fluorides are also candidates as active material. The reactions involved are then referred as conversion reactions. These electrochemical reactions were first explored by Poizot *et al.*[8] using nanosized transition metal oxides (e.g. NiO or FeO) and were spread to fluorides[9] (e.g. FeF_3, MnF_2) and even oxyfluorides[10] (e.g. FeOF). The drawings of Armand and Tarascon[11] perfectly illustrate the difference between the insertion and conversion mechanisms (**Figure I.5**). The drawings illustrate the insertion and conversion reactions for metal oxides (M being the metal ions and X the oxygen ions) but similar reactions can take place with metal fluorides. In the case of a fluoride, the equation of the conversion reaction can be written as:

$$xLi^+ + xe^- + MF_x \rightarrow M + xLiF \qquad\qquad 26.$$
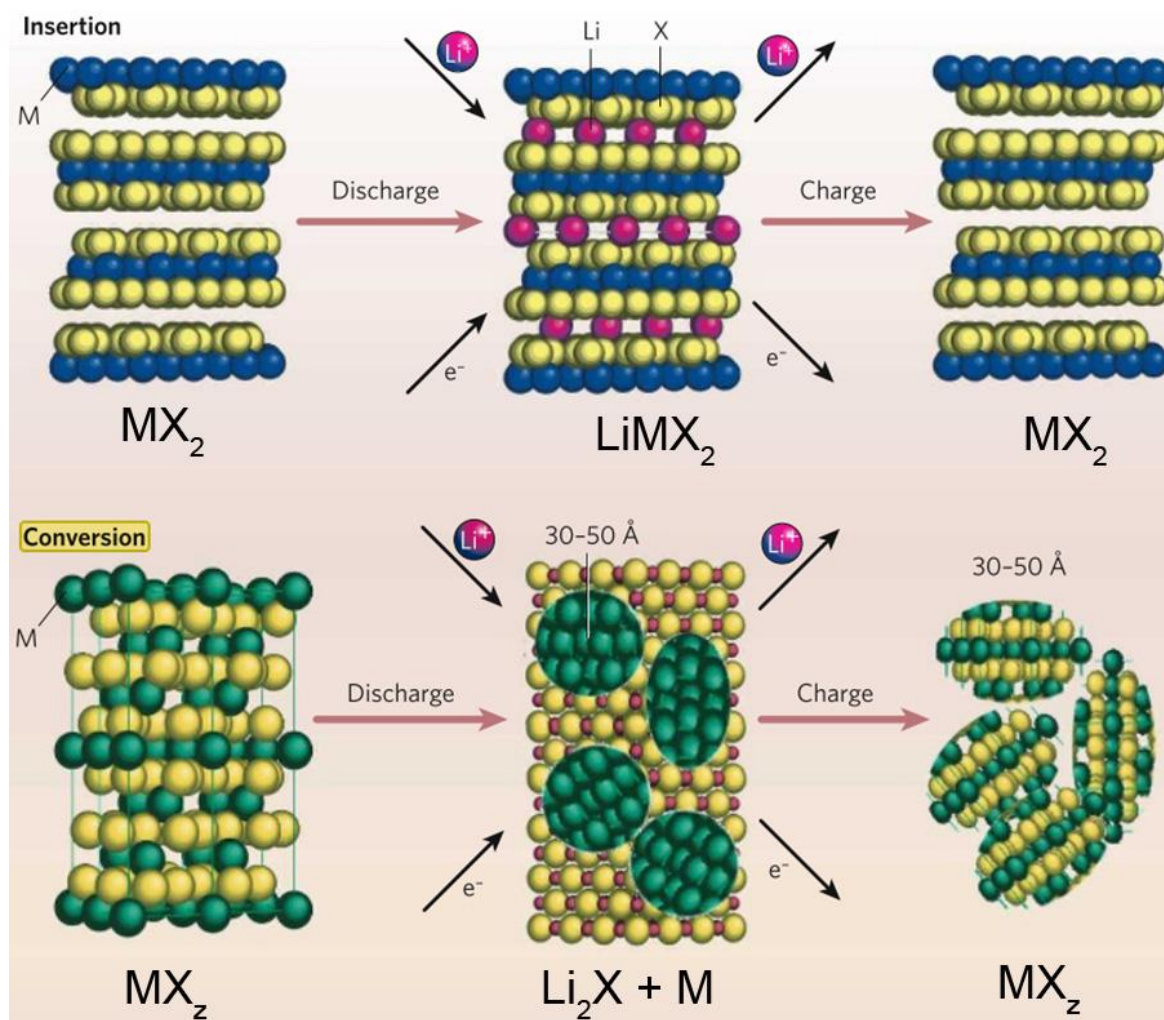
Figure I.5. *Schematic representation of the insertion and conversion mechanisms taking place in lithium batteries with oxides (M is a metal and X is oxygen). Taken from the work of Armand and Tarascon*[11] *and Amatucci and Pereira*[9].

Unlike insertion reactions where only up to 0.5 electrons can be inserted/extracted per mole of metal in the active material (to maintain intact the layered structure), conversion materials are capable of electrochemical reactions involving several electrons, depending on the oxidation state of the metal.

Let us consider a promising conversion material that was studied in our group: MnF_2. Nanosized MnF_2 can be used as anode. The reaction involves a 2 electron exchange process[12]. Upon discharge, MnF_2 reacts with lithium ions and electrons to form nanodomains (5-8 nm in diameter) of metallic manganese, embedded in a LiF matrix. It is expected that upon lithium uptake, the Mn nanodomains form a continuous network that allows transport of electrons within the bulk of the MnF_2 nanocrystals, allowing a continuous reduction of MnF_2. In addition to charge transport, mass transport must also be considered to explain the morphology of discharged electrode.

Wang et al. studied the conversion reaction mechanisms of FeF_2 in detail[13]. To explain the formation of interconnected Fe nanodomains embedded in a LiF matrix, they suspect the diffusion of Li^+ along the boundaries created at the interface between Fe and LiF. The Fe nanodomains are suspected to be essentially present where the initial FeF_2 phase was, due the lower mobility of Fe^{2+} than F^- or Li^+. Similar considerations can be made for Mn^{2+}.

During lithium extraction (charge), the LiF matrix is partly reduced and the fluorides react with Mn to form nanosized (3-5 nm) MnF_2 particles embedded in the unreacted LiF matrix. The first lithium uptake is often referred as an activation process, as the electrode structure is reorganized on the nanoscale, and significant loss of capacity is observed between the 1st discharge and the 1st charge due to side reactions such as electrolyte reduction (formation of the solid electrolyte interface during 1st discharge) and the presence of LiF. The electrochemically activated structure can then be cycled, with capacities significantly higher (e.g. above 400 mAh/g for MnF_2, and even more for some other oxides/fluorides) than those typically observed in insertion materials (e.g. below 200 mAh.g^{-1} for $LiCoO_2$). The precise mechanisms involving the complete redistribution of the active material within the electrode during the activation step is still unknown. Indeed, research efforts are often focused on the increase of the performance of the electrode, rather than the deeper understanding of the electrochemical mechanisms involved.

Obviously, the electrochemical reactions that take place in FIBs do not involve lithium ions. However, the fluorination and defluorination reactions that happen can somehow be assimilated

to conversion reactions, as they are multi-electronic processes and do not involve the insertion of the fluoride ions in a host structure. From a purely mechanistic point of view, the conversion mechanism in FIBs is simpler as it involves only electrons and fluoride ions, when the conversion reaction of MF_x in LIBs involves electrons, fluoride ions and lithium ions. However, the solid-state of FIBs renders the issue more complicated, as will be discussed in the next section.

The reduction of the metal fluoride to its metallic state has already been established by the group of Fichtner[14] (Refer to **3.2** for a detailed presentation.) However, the measured capacities suggest that the metal fluoride present at the cathode could not be fully reduced. This may be due to the absence of charge/mass transport towards the remaining, isolated particles.

Alternatively, one may imagine that upon conversion of the cathode (reduction of the MF_x), the metallic nanodomains form solely on the surface of the particle which is in contact with the electrolyte. The particles volume are continuously reduced until the breaking of the contact with the electrolyte occurs, and that no further ionic transport is ensured. The process eventually leaves isolated and unreacted MF_x regions in the resulting electrode.

Indeed, the conversion reactions involving the exchange of fluoride ions between the two electrodes will necessarily induce volumetric variations of the active material.

2.1.3. Volumetric variations of the active materials

The active material within the electrode will undergo volumetric variations far greater than the typical insertion reactions that happen in commercial LIBs. For example, the reduction of MnF_2 to Mn corresponds to a reduction of the volume of MnF_2 of 69 %. These volumetric variations are related to the volume of the crystallographic unit cell of the relevant materials. Volumetric variations can be calculated using the following equations:

$$\Delta V(MF_x \to M) = \frac{\frac{v_M}{N_M} - \frac{v_{MF_x}}{N_{MF_x}}}{\frac{v_{MF_x}}{N_{MF_x}}} = \frac{\frac{v_M}{N_M}}{\frac{v_{MF_x}}{N_{MF_x}}} - 1 \qquad\qquad 27.$$

$$\Delta V(M \to MF_x) = \frac{\frac{v_{MF_x}}{N_{MF_x}} - \frac{v_M}{N_M}}{\frac{v_M}{N_M}} = \frac{\frac{v_{MF_x}}{N_{MF_x}}}{\frac{v_M}{N_M}} - 1 \qquad\qquad 28.$$

with v_{MF_x} and v_M the crystal unit cell volume (Å^3), and N_{MF_x} and N_M the number of formula per unit cell of the metal fluoride and its corresponding metal. **Table I.3** shows the volumetric

calculated variations that can be expected for some fluorides and metals during discharge and charge processes.

$\Delta V(MF_x \to M)$ (%)		$\Delta V(M \to MF_x)$ (%)	
$MgF_2 \to$ Mg	-29%	Li $\to$ LiF	-24%
$CaF_2 \to$ Ca	7%	Na $\to$ NaF	-37%
$BaF_2 \to$ Ba	6%	K $\to$ KF	-50%
$MnF_2 \to$ Mn	-69%	Mg $\to MgF_2$	40%
$FeF_2 \to$ Fe	-68%	Ca $\to CaF_2$	-6%
$CuF_2 \to$ Cu	-66%	Ba $\to BaF_2$	-5%
$AlF_3 \to$ Al	-62%	Mn $\to MnF_2$	212%
$MnF_3 \to$ Mn	-76%	Fe $\to FeF_2$	210%
$FeF_3 \to$ Fe	-77%	Cu $\to CuF_2$	192%
$BiF_3 \to$ Bi	-36%	Al $\to AlF_3$	162%
$LaF_3 \to$ La	-32%	Mn $\to MnF_3$	313%
$CeF_3 \to$ Ce	-36%	Fe $\to FeF_3$	342%
$MnF_3 \to MnF_2$	-22%	La $\to LaF_3$	47%
$FeF_3 \to FeF_2$	-30%	Ce $\to CeF_3$	56%

Table I.3. *Calculated volumetric variations for some selected metal/metal fluoride couples. The crystal unit cell volume and number of formula per unit cell can be found from crystallographic database like ICSD.*

For some fluorination reactions, the calculated volumetric variations can be huge (e.g. $+212\%$ for Mn $\to$ MnF$_2$). Despite this issue and the high probability to lose the interparticle contact, several approach are practicable to counter this.

The first and easiest way to cope with the volumetric variations is to use of small quantities of active material in the composite. Large amounts of electrolyte and carbon will provide both efficient charge transport and better accommodation of the strains induced by the volumetric variation of the active material. Since that carbon black and graphite powders exhibit lubricating properties, their replacement by carbon nanotubes could provide an improvement of the mechanical strength of the electrode composite.

Another way to cope with the issue is the use of nanomaterials. Indeed, the strains induced by the volumetric variations could be better accommodated by nanocrystallites. Moreover, the large contact area created between the active material and these nano-additives should also provide a more complete reaction of the active material. This is typically the case when nanosized conversion materials are used in LIBs.

The use of appropriate binders should also help in accommodating these volumetric variations. Indeed, one of the main components of a typical LIB electrode is the binder. As its name suggest, it ensures the mechanical integrity of the cell upon the discharge and charge processes. In a conventional LIB relying on insertion mechanisms, PolyVinyliDene Fluoride (PVDF) is used with success to accommodate the volumetric variations associated with the insertion and desinsertion of lithium within the active material. For conversion or alloying materials, more appropriate binders such as carboxymethyl cellulose (CMC) or alginates are green and efficient alternatives to PVDF and provide excellent results in terms of cyclability[15]. Although, current all-solid-state FIBs are operated at elevated temperatures (150 °C) because of the relatively low conductivity of the fluoride electrolytes at room temperature. At these temperatures, these polymers may be degraded[1] (T_f (PVDF) = 170 - 180 °C). Moreover, their possible electrochemical activity, introducing side reactions, cannot be disregarded.

Finally, designing specific architectures is a key to counter the deleterious effects of the volumetric variations created by the electrochemical reactions underwent by the active material. Such approaches are successfully employed in conversion or alloying materials for LIBs[16]. For instance, the use of nanowires or carbon coating is successfully employed to accommodate the large volumetric expansions experienced by Si alloy anodes in conventional LIBs[17], [18].

In summary, while the operation of FIBs is faced with challenging issues, there exist many approaches that could potentially improve their performance.

3. State of the art of fluoride-ion batteries

There is a large time gap between first reports of reversible electrochemical cells based on other solid fluoride electrolytes and recent work. Considering that Anji Reddy and Fichtner evidenced the feasibility of the concept of reversible cells using *ex-situ* X-ray diffraction,

---

[1] Polyimides, because of their good thermal stability, could be of interest to develop binders suited for FIB.

special focus to this work will be given after reviewing the work performed in the early days of FIBs.

3.1. Early days

The early days of FIBs, which were more commonly referred as fluoride galvanic cells at the time, started with the use of PbF_2 as solid fluoride electrolyte. It opened the path for the development of many solid fluoride electrolytes with improved ionic conductivity, destined to be used in various electrochemical devices and electrochemical studies.

Although this part of the bibliographic study is focused on the performances of FIBs, many references are available concerning the enhancement of the ionic conductivity of the electrolyte(s) used in the respective study. In a nutshell, the doping of pure fluoride electrolytes with aliovalent fluorides (e.g. BaF_2-doped LaF_3, KF-doped β-PbF_2 or BiF_3-doped β-PbF_2) leads to an increase of the ionic conductivity of the doped material due to the creation of fluoride point defects. Fluoride defects present in the crystal structure provide fast diffusion pathways for fluoride ions. The more they are present, the faster the conductivity. Please refer to Chapter II for a general introduction about conductivity in ionic solids.

To the best of my knowledge, the first claims of a FIB can be found in a patent published in 1974 by Baukal.[19] He claimed that doped CaF_2 could be used as solid electrolyte in an all-solid-state FIB at 400 – 500 °C. But the patent does not provide any experimental data to support the claims.

The first report of a FIB supported by experimental observations has been provided by Kennedy and Miles, after studying the electrical properties of the fluoride electrolyte PbF_2[20]. In their electrochemical cell, Kennedy and Miles used KF-doped β-PbF_2 (or β-PbF_2:KF) as a solid electrolyte[21]. They observed OCVs of 0.70 and 1.30 V for CuF_2 and AgF cathodes, which is in good agreement with thee calculated values *vs.* a Pb anode. The following cell reactions were considered:

$$Pb + CuF_2 \rightarrow PbF_2 + Cu \hspace{4cm} 29.$$

$$\Delta E° = 0.72 \text{ V}$$

$$Pb + 2\ AgF \rightarrow PbF_2 + 2\ Ag \hspace{4cm} 30$$

$$\Delta E° = 1.32 \text{ V}$$

However, upon polarization, the potential quickly decayed, yielding poor capacities. Suspecting the passivation of the Pb electrode, they investigated Pb|KF-doped PbF_2|Pb symmetrical cells. One Pb electrode was deposited on the electrolyte to obtain a good contact. The other Pb electrode was a plate pressed on the electrolyte, so it could be detached and analyzed. They polarized the cell to 1 V until no current could be drawn anymore and they performed physical-chemical characterizations of the Pb anode plate. They observed the presence of coalesced deposits at the surface of the plate, which were composed of α-PbO_2 and Pb_2OF_2. They attributed the poor performance of the cell to the formation of α-PbO_2, an allotropic phase of PbF_2 offering a poor ionic conductivity. It is noteworthy that the lead oxyfluoride phase revealed by X-ray diffraction presented peaks with higher intensity compared to that of α-PbO_2. The result suggests that the oxide layer probably present at the surface of Pb could be fluorinated before Pb itself.

In the same timeframe, Kennedy and Hunter managed to discharge thin-film cells using PbF_2 as electrolyte, Pb as anode and CuF_2 as cathode[22]. The thin-film cells were built by vacuum evaporation, offering stable OCVs ranging from 0.61 to 0.70 V. To increase the conductivity of the CuF_2 film, which was measured to be 1.6×10^{-9} S.cm^{-1} at 25°C (a rather low value), CuF_2 was codeposited with beta-PbF_2. The codeposition process gave rise to amorphous films. The cells were discharged at current densities higher than 10 µA.cm^{-2}. The maximum capacity of measured reached 40 % of the theoretical capacity of CuF_2 (528 mAh/g). This was calculated assuming that the PbF_2:CuF_2 codeposited films contained 50 mol% of CuF_2. Attempts to charge the cell all failed. No significant charge capacity could be recovered.

Following the work of Kennedy, Schoonman[23] built a Pb|β-PbF_2:AgF|$BiO_{0.09}F_{2.82}$|Bi cell relying on the following cell reaction:

$$3\ Pb + 2\ BiF_3 \rightarrow 3\ PbF_2 + 2\ Bi \qquad\qquad\qquad 31.$$

$$\Delta E° = 0.37\ V$$

The cells were built by painting the β-PbF_2:AgF and $BiO_{0.09}F_{2.82}$ powders dispersed in ethyl acetate onto Pb and Bi disks, and by spring-laoding the disks together. Both β-PbF_2:AgF and $BiO_{0.09}F_{2.82}$ presented relatively good ionic conductivity (about 5×10^{-6} S.cm^{-1} at RT) and significantly lower electron hole conductivity at this potential ($\sigma°_h \approx 10^{-10}$ S.cm^{-1} for $BiO_{0.09}F_{2.82}$). Once again, the OCVs of 0.330-0.335 V were in relatively good agreement with the theoretical value, suggesting that oxyfluorides are also candidates to be used in FIBs. Upon discharge, the cell potential dropped to a plateau value depending on the load applied.

Eventually, the potential neared 0 V in a matter of days, depending on the load applied. However, the OCV value could be recovered when the polarization was ended, suggesting that the cell was not entirely discharged and that passivation of an electrode occurred. Similar to the observations made by Kennedy, the current drawn from the cell was significantly increased when the discharge was carried out at elevated temperature. However, no information about the reversibility of such cell was given.

At around the same time, a patent from Borger *et al*.[24] suggests that carbon fluoride $(CF)_n$ could be discharged against a lead electrode using $K_{0.25}Pb_{0.75}F_{1.75}$ as solid electrolyte, at 280 °C with a current of 0.1 mA. This is the only claim supported by experimental data in the patent. It is however an important one, as it suggests that carbon could be used as active material in FIB.

Danto *et al*.[25] confirmed the work of Schoonman by building a $Pb|PbF_2|BiF_3|Bi$ cell obtained upon charging a $Bi|PbF_2|Bi$ thin-film structure obtained by thermal evaporation. Upon charging, PbF_2 at the Bi cathode is reduced to Pb, while at the anode, Bi is oxidized to BiF_3. Charging was carried out at constant current until a capacity of 12 µAh was reached. A voltage of 0.4 V was measured upon charge. The charging voltage and OCV values of 0.353 V obtained after charging suggested that the cell depicted above was successfully obtained. The cell could then be cycled several times successfully, indicating that the reaction is reversible.

In 1979, Schoonman *et al*.[7] essentially repeated the study on the $Pb|\beta$-$PbF_2:AgF|BiO_{0.09}F_{2.82}|Bi$ configuration, investigating new electrolytes based on solid solutions $M_{1-x-y}U_xCe_yF_{2+2x+y}$ (M = Ca, Sr, Ba), as well as cubic BiF_3 (*Fm-3m* space group) as cathode and Ca as anode. The publication is rather focused on the electrical properties of the components of the cell and gives insight on the ionic conductivity of cubic BiF_3 ($\sim 1\times 10^{-6}$ S.cm^{-1} at RT), which is close to the conductivity of tysonite-type $BiO_{0.1}F_{2.8}$ ($\sim 5\times 10^{-7}$ S.cm^{-1} at RT). Nevertheless, the study set the course for the future investigations, as the growth of passivating layers formed at the surface of the anodes could be monitored upon operation of the cell.

- For Ca, the low conductivity of the pure CaF_2 ($\sim 2\times 10^{-9}$ S.cm^{-1} at RT for large crystallites[26]) layer formed at the surface lead to passivation.
- However, unlike reported by Kennedy and Miles, the formation of alpha-PbF_2 or Pb_2OF_2 at the surface of the Pb anode did not reveal to be blocking as the cell was reversible.

The above assumptions were made by measuring the internal resistance of the cell upon charge/discharge cycles. The cell resistance was measured from the overpotential ("OCV – LCV", LCV being the "load-circuit voltage") and the load applied to the cell, using ohm's law.

Considering the interesting cell potential developed by the Ca/CaF_2-Bi/BiF_3 couple (about 3 V), efforts were made by Schoonman and Wolfert[27], [28] to counter the passivation of the Ca anode. In a sort of last attempt, they employed $Ca_{1-x}M_x$ (M = La, Yb) alloys to form the corresponding fluoride (e.g. $Ca_{1-x}La_xF_{2+x}$) which would offer better ionic conductivity than CaF_2. The idea proved to be effective as significantly lower cell resistance (about two orders of magnitude) was monitored upon operation of the cell.

This publication is the last publication that brings a significant input to the field and marks the end of the early development of FIBs. The fleeting popularity of FIBs was probably stopped with the advent of lithium batteries and the commercialization of the first lithium battery working on the rocking chair principle in the early nineties. It is only recently that their interest was renewed.

3.2. Recent work

The renewed interest for FIBs was provided by a proof of concept demonstrated by the work of the group of Pr. Fichtner. In 2011, a communication of Anji Reddy and Fichtner[14] proved that reversible cells could be operated using simple preparation techniques.

The bulk cells relied on the use of LBF10 ($La_{0.9}Ba_{0.1}F_{2.9}$, tysonite-type structure LaF_3 doped with 10 mol% of fluorite-type structure BaF_2) as solid electrolyte due to its relatively high conductivity (2.8×10^{-4} $S.cm^{-1}$ at 160 °C). Cells were assembled by cold pressing pellets composed of the electrolyte and positive electrode powders, with a disk of cerium as negative electrode. Several metal fluorides (MF_x = CuF_2, BiF_3, SnF_2 and $KBiF_4$) composites were evaluated. The LBF electrolyte was easily prepared by ball-milling LaF_3 and BaF_2 in stoichiometric amounts and the positive electrode composites were prepared by an additional ball-milling step of MF_x:LBF:C in a 30:60:10 % wt ratio. For most preparations, a high rotational speed of 600 rpm was used. For BiF_3 however, two different conditions, i.e. ball-milling at 150 and 600rpm in the presence of LBF, lead to two radically different structures. The one ball-milled at 600rpm formed a so-called "solid solution" with LBF since that only the tysonite-type structure similar to that of LBF could be observed on the diffraction pattern. The authors assumed it was due to a possible doping of BiF_3 by oxygen to form tysonite-type

structure oxyfluoride $BiO_{0.1}F_{2.8}$ which could then form a solid solution with LBF. It is also interesting to notice that $BiO_{0.1}F_{2.8}$ was notably used as electrolyte by Schoonman.[28] If such phase transition does occur, it could explain the better capacity and reversibility (50 mAh/g after 40 cycles), of the BiF_3 solid-solution electrode, compared to the other metal fluoride composites, including the one based on BiF_3 (prepared at 150 rpm). Indeed, the enhanced conductivity of the active material associated with the reduction of its size could lead to improvements in terms of kinetics, due to the faster diffusion of fluoride ions, and in terms of volumetric variations (easier accommodation with less strains). Unfortunately, the communication lacks of details (e.g. crystallographic data related to the BiF_3 solid-solution) for a better understanding of the origin of the enhanced performance of this material.

All cells using the composite electrodes could be discharged with capacities superior to 130 mAh/g of MF_x when discharged down to 1 V at 150 °C. Discharge curves exhibited a single pseudo-plateau between 1.7 and 2.7 V depending on the MF_x tested. The best discharge performance goes out to CuF_2 for reaching a capacity of 322 mAh/g. But like the other composites, it showed very limited cycling stability. Nonetheless, the reduction of the metal fluorides was definitely established as in most cases, peaks corresponding to the respective metal (Bi or Sn) could be observed on XRD patterns obtained from the cathode. This report is the first real evidence that electrochemical conversion of the metal fluoride can take place in FIBs. However, no information about the electrochemical reactions taking place at the Ce electrode was presented. One may imagine that the suspected formation of CeF_3 at the Ce was not blocking.

In another publication by Rongeat *et al*.[29], the group decided to continue their investigations starting from the "discharged" configuration (e.g. Bi vs. CeF_3). This switch was justified by the high sensitivity of Ce towards oxidation, which could lead to degradation of the performance when this metal was used as anode.

N. B.: It is important to note that similar observations were made on our side during this thesis. Early experiments (not presented in this manuscript) were carried out with Ce disks as anode, and attempts to reproduce the results of Anji-Reddy and Fichtner were all met with failure. After galvanostatic experiments at 150 °C with the modified coin cell setup presented in **Chapter III**, *the surface of the Ce disk was significantly oxidized (Ce_2O_3), especially on the side in contact with the electrolyte, although the surface of the Ce disk was scrapped prior assembly of the cell (in a dry Ar glovebox), and special precautions were taken to avoid a significant amount of oxygen within the cell (e.g. Ar purge). The capacities obtained during our*

experiments were largely inferior (i.e. a few dozen mAh/g) to those obtained by the previously mentioned authors. In a similar manner, we therefore decided to continue experiments working with Bi as anode material.

The cells were tested using Bi or Cu as anode and CeF_3, CaF_2 and MgF_2 as cathode (N. B.: In this publication, Bi and Cu are wrongfully designated as being the cathode materials.) For all cell combinations, little to no reversibility could be obtained, while the charge capacity was generally above the theoretical capacity of the active materials, suggesting side reactions.

The CeF_3 vs. Bi cell is of particular interest as it is the discharged configuration of the Ce vs. BiF_3 cell of the previous paper, which showed the most promising electrochemical performances.
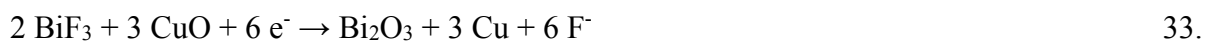
The following cell reaction was considered:

$Ce + BiF_3 \rightarrow Bi + CeF_3$ 32.

$$\Delta E° = 2.83 \text{ V}$$

The CeF_3 vs. Bi cell exhibited an OCV of about 0 V and a galvanostatic charge curve presenting three voltage plateaus, suggesting a three-step charging process. The first plateau starts from 1.5 V up to 2.3 V (about 130 mAh/g) and is below the theoretical potential of the cell, meaning that the considered cell reaction does not involve Ce and BiF_3. The second plateau is really flat and gives an average voltage of 2.5 V (about 150 mAh/g). Once again, this value does not correspond to the theoretical potential. Indeed, the effect of the overpotential should lead to voltage plateaus of higher values than the theoretical potential (i.e. 2.83 V). Only the last pseudo-plateau (3 – 4 V, about 100 mAh/g) is above the theoretical potential of the couple and should correspond to the cell reaction 32.

To investigate the electrochemical mechanisms involved, the Bi anode was characterized by XRD and XPS at different states of charge. After charging to 2 V, a cubic phase of bismuth oxyfluoride $BiF_{3-x}O_x$ was detected by XRD. At 2.5 V, in the middle of the charge plateau, no BiF_3 is detected. It is only after a charge up to 3.2 V that BiF_3 can be detected. Up to 4 V, no new phases were detected. XPS measurements confirmed the increasing formation of $BiF_{3-x}O_x$ (or BiF_3 as they cannot be distinguished by XPS) during increasing charging voltage. Remaining Bi can be detected in both XPS and XRD suggesting that unreacted Bi is still present, even after charging up to 4 V.

Considering that the capacities reached are larger than the theoretical capacity of Bi, a conversion mechanism involving other materials must be considered. The starting Bi powder contains significant amounts of Bi_2O_3. The authors suggest that the fluorination of Bi_2O_3 could explain the presence of $BiF_{3-x}O_x$ detected by XRD. This is an important result as it means that an oxide might be fluorinated before the metal, due to a partial substitution of oxygen ions by fluoride ions.

In a patent submitted by Potanin[30], which probably greatly inspired the work of the group of Fichtner, experimental results obtained on La|LBF|BiF$_3$:KF cells at 550 °C showed small amounts of CuO in the BiF$_3$ electrode enhanced the specific capacity of the cell. He proposed the following mechanism at the cathode:

$$2 \ BiF_3 + 3 \ CuO + 6 \ e^- \rightarrow Bi_2O_3 + 3 \ Cu + 6 \ F^- \qquad\qquad 33.$$

At the anode:

$$La + 3 \ F^- \rightarrow LaF_3 + 3 \ e^- \qquad\qquad 34.$$

Leading to the overall cell reaction:

$$2 \ La + 2 \ BiF_3 + 3 \ CuO \rightarrow 2 \ LaF_3 + Bi_2O_3 + 3 \ Cu \qquad\qquad 35.$$

$$\Delta E° = 2.98 \ V$$

Which is to be compared with the cell reaction:

$$La + BiF_3 \rightarrow LaF_3 + Bi \qquad\qquad 36.$$

$$\Delta E \ ° = 2.83 \ V$$

Such alternative side-reactions, owed to the presence of significant amounts of oxides in the Bi composite electrodes, could explain the additional capacity observed during the charging of the cells. Indeed, other cells using Bi as anode and CaF_2 or MgF_2 as cathodes also show pseudo-plateaus (with capacities > 150 mAh/g) below the theoretical potential at which the expected cell reaction should occur (i.e. below 3.2 V and 2.65 V, for CaF_2 and MgF_2, respectively).

To investigate the reason why no reversibility was obtained in these configurations, a mixture of Mg and MgF_2 was tried out as cathode. The OCV was about 1.8 V, probably owed to the presence of Mg, creating a new redox couple. The first charge (266 mAh/g) exhibited 2 plateaus, suggesting that the previously discussed side reaction ($BiF_{3-x}O_x$ from Bi_2O_3) still occurred. The cell could then be discharged but only about 70 mAh/g could be recovered. The capacity then rapidly faded upon cycling to reach only 10 mAh/g after 50 cycles. Cu was also

investigated as anode instead of Bi, but the performance was even worse upon subsequent cycling. This was attributed to the large volume change (192 %) for the oxidation of Cu to CuF_2.

3.3. Cells based on liquid electrolyte

Cells based on liquid or polymeric electrolytes are referred as room temperature fluoride ion batteries as liquid electrolytes generally provide faster mass transport than their solid counterparts. The literature is even scarcer than for solid-state systems and no proof of concept is presented.

The first contribution is presented in a patent from Darolles *et al*.[31] The presented results mainly rely on the use of a liquid electrolyte obtained by dissolving 0.1 M tetramethylammonium fluoride (TMAF) in an ionic liquid, 1-methyl-1-propylpiperidinium bis(trifluoromethanesulfonyl)imide (MPPTFSI). They could cycle cells using polyaniline (PANI) and PbF_2 composites (i.e. typical AM+PVDF+carbon slurry deposition on metal foil) as electrode materials. A stable OCV of about 1.1 V could be observed, and galvanostatic experiments showed some reversibility. But looking at the electrochemical stability window of the prepared electrolyte, one can suspect a large contribution of the electrolyte redox activity to the observed capacities (~100 mAh/g). Unfortunately, no characterization of the electrodes after operation is showed.

Gschwind *et al*.[32] reported a fluoride-doped polyethylene glycol (PEG) matrix as an electrolyte for FIB. Their strategy was to partially coordinate hydrogen difluoride HF_2^- using a methylated PEG matrix. HF_2^- supposedly acts as charge carrier between an Mg anode and BiF_3 composite cathode. The cells could be discharged with varying capacities depending on the constituents of the electrolyte (e.g. PEG chain length) and electrode preparation. The cells could not be cycled due to the passivation of the Mg anode. No characterization of the BiF_3 electrode after discharge was performed.

In conclusion, room temperature fluoride ion batteries are faced with the challenge of producing adequate liquid electrolytes. The field would benefit from providing unequivocal proof that the capacities measured are indeed related to the defluorination of the cathode and not from side reactions, such as the redox activity of the prepared electrolytes.

4. The need of a reference electrode

The study of FIBs is complicated by the fact that no reference is available when F⁻ is considered as shuttling ion. In order to contextualize this issue, it is relevant to quickly review how research is generally performed on LIBs.

4.1. Two and three electrode setups

In a two-electrode electrochemical cell, current and potential are measured between the working electrode electrode (WE) and counter electrode (CE). Even if the CE is of known potential, as current flows, its potential will vary and the absolute potential of the WE cannot be known. Only the difference in potential between the two electrodes is known. This configuration is typically used in charge-discharge experiments to evaluate the electrochemical performance (particularly the capacity) of the cell.

In a three-electrode cell, a reference electrode (RE) of known potential is added. The reference is usually a small piece of metal in contact with the electrolyte. For solid-state batteries, it can be attached on the side of the pellet electrolyte, or even inserted in the electrolyte layer. Since that no current flows between the RE and WE, the potential of the WE can be precisely determined as the potential of the RE is known and stable. The potential of the CE can also be determined precisely. Such configuration can be of interest in the study of the kinetic properties of the WE.

The distinction between the two cell configurations is presented on **Figure I.6**.
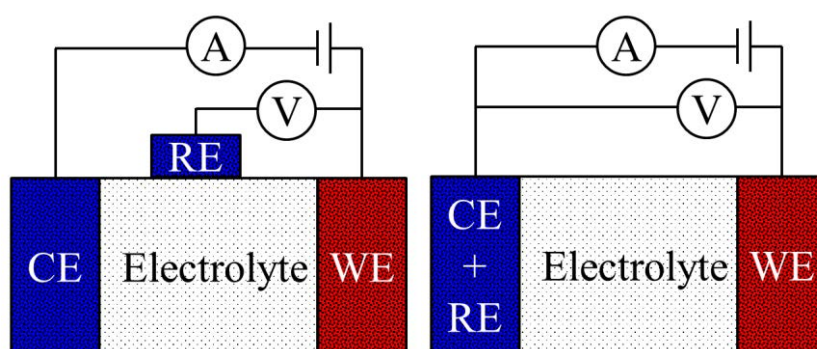
Figure I.6. *Schematic representation of a three-electrode (left) and two-electrode (right) cell with the counter electrode CE, reference electrode RE and working electrode WE.*

4.2. Reference electrode in LIBs and FIBs

When research is performed on LIBs, two or three electrode electrochemical cells can employ metallic lithium as CE and RE. Such cells are referred as *half-cells.* If the CE and WE are not metallic lithium, the cells are referred as a *full-cell*s. A piece of lithium can still be used as RE to provide the potential of the CE and WE electrodes.

Li provides a good RE/CE to evaluate the electrochemical properties of the material at the WE. Upon operation of the half-cell, Li plating/stripping occurs at the Li CE during successive charge discharge processes. Li at the RE remains intact and provides a stable potential. The potential is thus conveniently expressed as V vs. Li^+/Li.

For FIBs, the element form of fluoride is fluorine F_2, a highly corrosive and toxic gas in standard conditions. Obviously, its use as RE would be difficultly implemented.

The use of Li may be suited to be used as RE in FIBs, as long as the interface formed between Li and the electrolyte is stable. Experimental results suggest that it is indeed stable (see Chapter II.4.3.2).

However, Li may not be entirely appropriate as CE. Upon oxidation of Li, the LiF layer formed on the surface could eventually passivate the surface as LiF presents poor ionic and electronic conductivity. Similar conclusions were made with Pb and Ca anodes in the early days of the study of FIBs (see 3.1 of this chapter).

This effect may be illustrated by the work of Rongeat *et al*.[33] who tested a Li anode, with $Ba_{0.6}La_{0.4}F_{2.4}$ as solid electrolyte, and a BiF_3 composite as cathode (**Figure I.7**, left). Nanocrystalline fluorite-structure $Ba_{0.6}La_{0.4}F_{2.4}$ offers an ionic conductivity very close to that of LBF[34]. The BiF_3 composite cathode was previously used with relative success against a Ce anode[14] (**Figure I.7**, right). Looking at the discharge curves below 2.2 V for $Li|Ba_{0.6}La_{0.4}F_{2.4}|BiF_3$ cell, we see that the potential starts to vary in an erratic manner as it goes down to 1.5 V. This observation may be caused by the passivation of the Li anode. Indeed, as discharge occurs, the layer at the $Li|Ba_{0.6}La_{0.4}F_{2.4}$ interface grows and becomes more blocking, and the ohmic drop increases. One can imagine that the constant current applied to the cell will force the layer to break down to allow charge transfer, and the ohmic drop will thus decrease. The repetition of this "passivation/transpassivation" mechanism during the discharge might be the cause of the erratic behavior of the potential at low voltage.
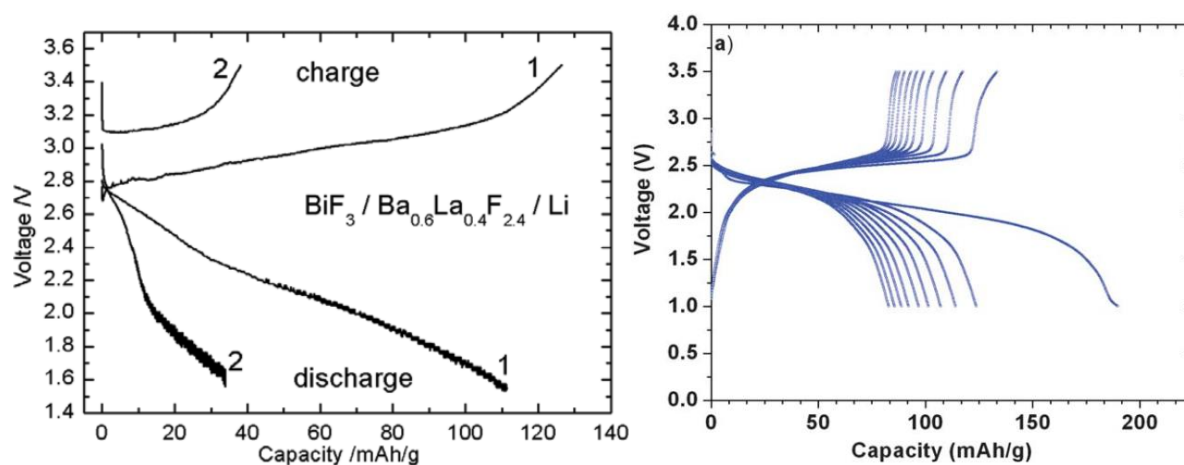
Figure I.7. *Galvanostatic cycling of a Li|Ba$_{0.6}$La$_{0.4}$F$_{2.4}$|BiF$_3$ cell (left, 4 mA.g^{-1})[33] and a Ce|La$_{0.9}$Ba$_{0.1}$F$_{2.9}$|BiF$_3$ cell (right, 10 µA.cm^{-2})[14] at 150 °C. The indices present on the graph (left) indicate the order in which the charge/discharge curves were recorded.*

In summary, Li may provide a good RE material for FIBs (see results of **Chapter II.4.3.2**). However, its use as CE might be faced by the probable formation of a passivating LiF layer upon oxydation which might eventually impede charge and mass transfers.

Chapter II. Characterization of fluoride solid electrolytes

1. Introduction

As mentioned in chapter one, one of the most crucial component of a solid-state battery is its electrolyte. It ensures the shuttling of ions from one electrode to the other, allowing the redox reactions to happen. Good electrolytes exhibit negligible electronic conductivity and high ionic conductivity. They must be electrochemically stable within the operation voltage of the cell. Finally, they must be chemically compatible with the electrode materials to ensure fast transport of the charged species through the interfaces present between the electronic and ionic transporting components of the battery. Ba-doped LaF_3, $La_{1-x}Ba_xF_{3-x}$ ($0 \leq x \leq 0.15$) (LBF) seems to be a good candidate for all-solid-state FIBs as it was successfully used by the group of Pr. Fichtner[14]. This chapter is dedicated to LBF.

In a first part, the relation between the structural and the electrical properties of solid electrolytes in general, and applied to FIBs, will be discussed. The talk will be illustrated by the example of LaF_3 and LBF.

This knowledge will be useful to present the state of the art of LBF in a second part. The state of the art will be concluded with a comparison of LBF with state of the art lithium electrolytes, and the necessity to investigate the electrochemical stability of LBF.

The last section focusses on the use of polycrystalline $La_{0.95}Ba_{0.05}F_{2.95}$ as solid-state electrolyte for FIBs. The section includes the investigations of the electrical and electrochemical properties of LBF. The use of lithium as electrode and the stability of the interface it forms with LBF is investigated. Lithium is then used to study the electrochemical stability of LBF. Finally, a composite formed of LBF and carbon (LBF-C composite) will be used to explore the electrochemical interactions that may take place between LBF and carbon in a typical composite electrode for FIBs. The electrical properties of the LBF-C composite will be particularly probed and discussed to understand the electrochemical results obtained on the LBF-C composite.

Electrochemical impedance spectroscopy (EIS), an inescapable tool for the study of the electrical properties of solid electrolytes, is introduced in **appendix 2**. The principle of EIS, and the fitting of EIS data applied to the study of solid-state electrolytes is presented.

2. Electrical conductivity and ionic conductivity

2.1. Fundamental notions

The electrical conductivity σ (S.cm^{-1}) quantifies how strongly a given material allows the flow of electric current. It is characterized by the ratio between the current density j (A.cm^{-2}) and the applied electric field $\boldsymbol{E}$ (V.cm^{-1}), in accordance with Ohm's law.

$$\sigma = \frac{j}{E} \tag{37.}$$

The conductivity σ is the inverse of the resistivity ρ (Ω.cm) and can be determined by measuring the resistance R (Ω) that the material opposes to the electric current, providing that its length L (cm) and cross sectional area A (cm²) are uniform and measurable.

$$\sigma = \frac{1}{R}\frac{L}{A} = \frac{1}{\rho} \tag{38.}$$

Moreover, σ is the sum of the electronic σ_e and ionic σ_i conductivity contributions.

$$\sigma = \sigma_e + \sigma_i \tag{39.}$$

The ionic (or electronic) transference number t_i (or t_e) characterizes the contribution of the ionic (or electronic) conductivity to the total conductivity.

$$t_i \equiv \frac{\sigma_i}{\sigma_{tot}} \tag{40.}$$

$$t_e \equiv \frac{\sigma_e}{\sigma_{tot}} \tag{41.}$$

From a practical point of view, the resistance of electrolyte can be determined experimentally by performing electrochemical impedance spectroscopy (EIS) measurements. An introduction to EIS is available in appendix 2.

Now that the fundamental notions have been introduced, we can take a look at what lies behind the conductivity of ionic solids.

2.2. Conductivity in ionic solids

2.2.1. Generalities

All ionic solids conduct electricity due to unavoidable defects present in their crystalline structure. However, these defects are only sporadically present in the structure, so that most

ionic solids exhibit poor conductivity and are generally considered as insulators in standard conditions.

Only a few solids can offer conductivities that are sometimes high enough to reach the values of liquid electrolytes. These ionic solids exhibit specific structural features, allowing for high conductivity (10^{-1} - 10^{-5} S.cm^{-1})[35] well below their melting point. They are sometimes referred as *fast ion conductors* or *superionic conductors*, but are more commonly named *solid electrolytes*.

Only a few solid fluorides exhibit significant electrical conductivity. The electrical conductivity of fluorides usually rises from their ionic conductivity, since that fluorides are generally electronic insulators due to their large band gap, as predicted by the band theory.

However, they can still exhibit significant residual electronic conductivity by motion of electrons and/or holes[36], [37]. This is of major importance as in electrochemical systems, it is crucial to determine both contributions to the total conductivity. Indeed, to avoid spontaneous discharge of the FIB and to avoid faradaic loss, the electronic conductivity of the electrolyte must be several orders of magnitude lower than the ionic conductivity. For the practical use of a solid-electrolyte in an electrochemical cell, an ionic transference number t_i as close as possible to 1 is desired. If t_i becomes significantly lower than 1, electronic leakage will take place in the cell and the faradaic yield will be accordingly degraded.

2.2.2. Mechanism of ionic conductivity

The mechanism relies on the hopping of the ionic species (the fluoride ion in our case) from site to site, along channels that are present in the rigid crystal framework of the material. Increasing hopping rate, and multiplicity of diffusion channels, result in improved conductivity of the electrolyte. In a phenomenological approach, σ_i can be expressed as the product of concentration c_i, charge q, and mobility u_i of its ionic species.

$$\sigma_i = c_i q u_i \qquad\qquad 42.$$

Two conduction mechanism for the mobility of ions can be distinguished. They both rely on point defects (defects at, or around, a single lattice point, involving only a few atoms) that are inherently present in the crystal sub lattice: vacancies and interstitials.

In a vacancy type conduction, the ion hops from its site to another vacant site with equivalent energy. In an interstitial type conduction, the ion hops from its site to an interstitial position

where no ions should be present. The interstitial position generally has a higher energy value. The presence of conduction pathways (e.g. diffusion channels) where these mechanisms are energetically favored results in an increased mobility of the ionic species and thus a better conductivity.

The conductivity of a material is temperature dependent. In an ionic solid, for an ion to hop, it must overcome the energetic barrier that separates it from the next site. The displacement of ions along conduction channels can be seen as a series of potential wells and barriers as outlined by **Figure II.1**. The drawing illustrates how an ion can hop from one site to another when it has enough energy to overcome the barrier that separates it from the next lattice point.
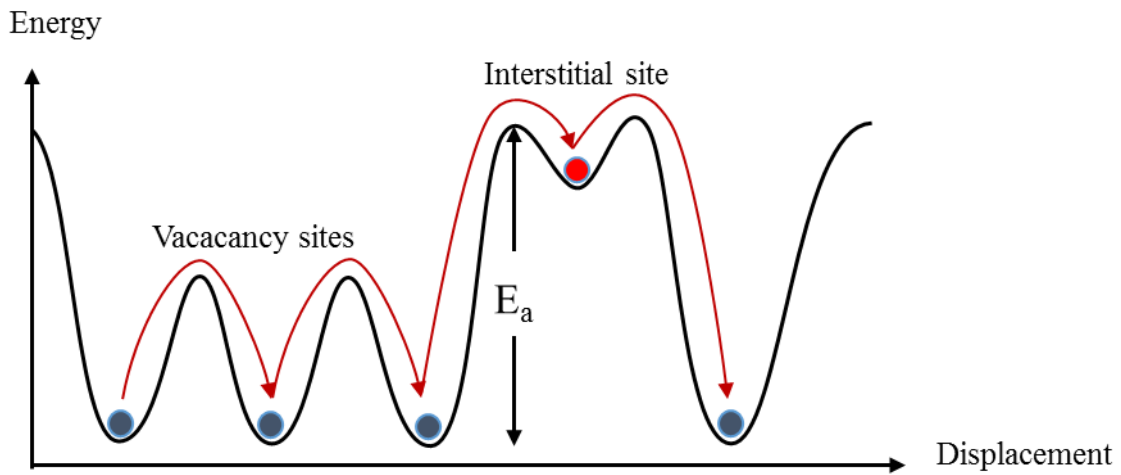
Figure II.1. *Illustration of the energy profile for an ionic species migrating in a solid electrolyte. The interstitial site has a higher potential energy than the vacancy sites.*

This energetic barrier, called activation energy, E_a, is the major factor controlling the mobility u_i. The activation energy can somewhat be seen as the equivalent of the band gap E_g in the band theory. It is linked to the conductivity and temperature by an Arrhenius type law:

$$\sigma_i = \frac{A_T}{T} exp(\frac{-E_a}{k_B T})$$
43.

Where A_T is called the pre-exponential factor, or prefactor, which contains many terms like the number of mobile ions[38], T is the absolute temperature (K), and k_B is the Boltzmann constant ($k_B \approx 8.6173324.10^5 \ eV.K^{-1}$) [39].

To continue the discussion and illustrate the Arrhenius-type law of conductivity, let us take LaF$_3$ as example. **Figure II.2** represents (a) the ionic conductivity of a LaF$_3$ single crystal in a typical Arrhenius plot along two directions, perpendicular and parallel to c axis, and (b) the

respective representations of LaF_3 crystal structure. Arrhenius plots are commonly presented by plotting the log of the conductivity in function of the inverse temperature in order to visualize and compare E_a, which is proportional to the slope of the curve. A larger E_a will lead to a greater increase of the conductivity with increasing temperature (steeper slope). The ionic conductivity of the LaF_3 single crystal was measured perpendicular and parallel to its c axis. We can observe that the increase of σ_i with increasing temperature is greater when the conductivity of LaF_3 is measured perpendicular to c axis. Consequently, E_a is higher for the direction perpendicular to c axis.
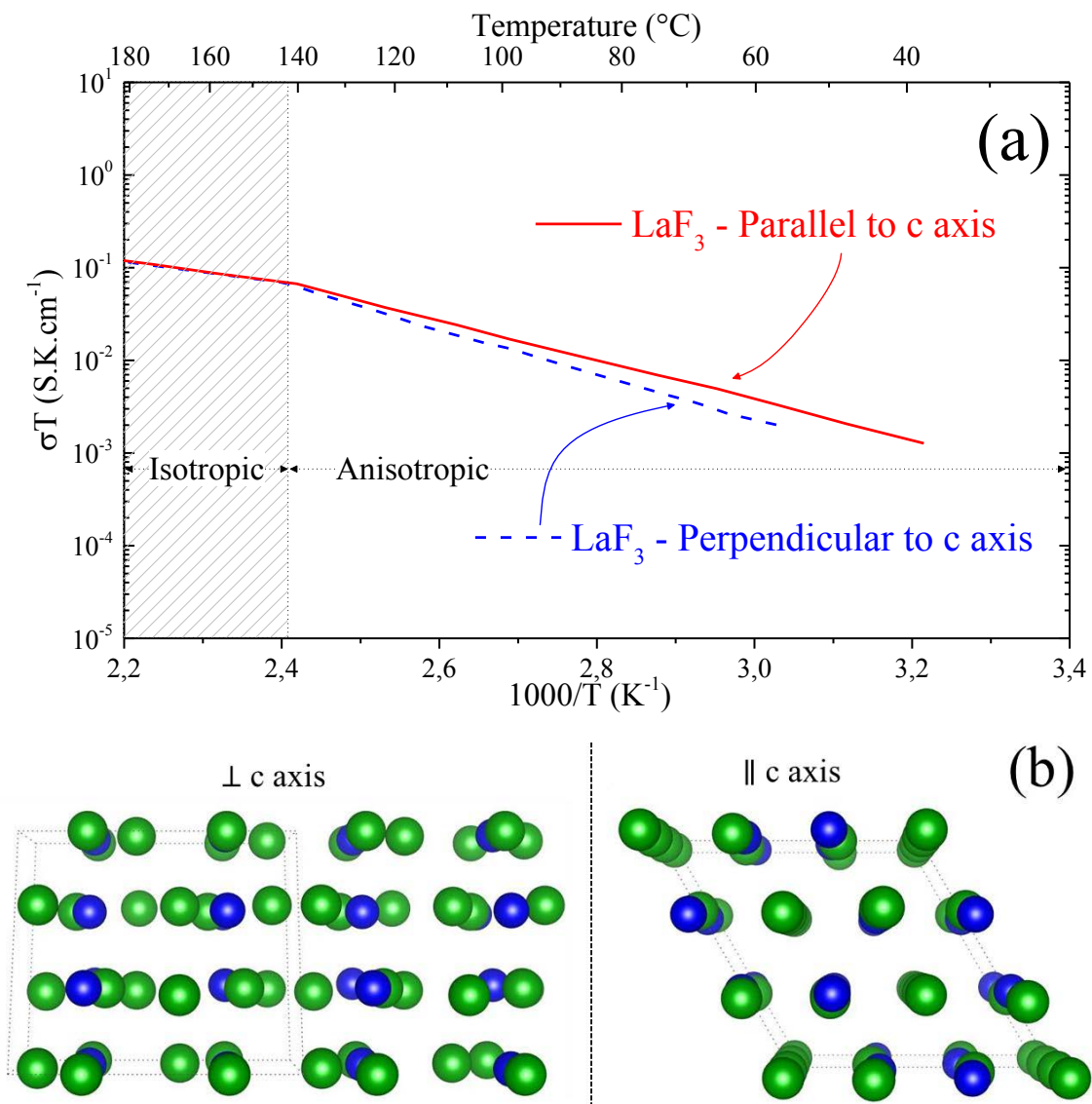
Figure II.2. *(a) Arrhenius plot of the bulk ionic conductivity of a LaF₃ single crystal perpendicular and parallel to its c axis. Experimental data collected by Schoonman et al.[40] (b) Crystal structure of LaF₃ perpendicular (left) and parallel (right) to c axis. The blue balls represent La³⁺ cations and green balls F⁻ anions. The dotted lines represent the unit cell.*

This observation illustrates the anisotropic nature of σ_i and the presence of preferable conduction pathways due to preferable motion of fluoride ions in certain directions of the crystal structure. The Arrhenius plot shows that at RT, F⁻ move faster along c axis due to preferable hopping energies in this direction, as illustrated by **Figure II.2.b**, where it is possible to see some F⁻ ions perfectly aligned along the c axis. As temperature increases, conduction pathways perpendicular to c get thermally activated faster than the ones parallel to c. Between 140 and 180 °C, conductivity becomes isotropic ⊥ and ∥ to c.

3. State of the art and choice of La$_{1-x}$Ba$_x$F$_{3-x}$

Ionic conductivity can be enhanced by introducing defects in the crystal lattice in order to increase the concentration of mobile ionic species c_i. One practical way to do this is to dope the crystal with aliovalent (heterovalent) ions, an approach which is often referred as homogeneous doping. The doping of LaF$_3$ (La^{3+}) by BaF$_2$ (Ba^{2+}) creates a net deficit of positive charges in the crystal. The electroneutrality is maintained by the creation of fluoride vacancies which allows the higher mobility of F⁻ in the crystal sub lattice, yielding an increased conductivity.

This is typically the case in the widespread nonstoichiometric phases based on the LaF$_3$-tysonite type (*P*-3*c*1) and on the CaF$_2$-fluorite type (*Fm*-3*m*) structures[41], [42]. Tysonite-type systems Ln$_{1-x}$M$_x$F$_{3-x}$ (Ln = La, Ce, Sm and M = Ba, Ca, Sr) and fluorite-type systems M$_{1-x}$A$_x$F$_{2+x}$ (M = Ba, Pb, Sn and A = Ca, La, Sn, K) are promising as they are amongst the electrolytes with the highest conductivity values reported in the literature. However, the conduction mechanisms involved in tysonite and fluorite structures are different, as the fluorite conduction mechanism involves anti-Frenckel pairs (one anion vacancy combined with one interstitial anion) while tysonite structures rely on a purely vacancy-type mechanism due to Schottky defects (one cation vacancy associated with one anion vacancy)[33].

However, the electrical properties of LBF are highly dependent on the crystalline form under which it is used.

Part of the state of the art presented in this chapter will introduce the effect of the microstructure on the conduction properties of LBF. For an in-depth investigation of the conduction mechanism of solid fluoride electrolytes, one can refer to the thesis of J. Chable[43], as part of the Fluobat project. The primary focus of his work was the conduction properties of solid electrolytes for fluoride-ion batteries, and particularly tysonite-type solid-solution such as LBF.

3.1. Early work with single crystals

Roos *et al*. have thoroughly investigated the general electrical conduction[44] as well as ionic[45] and electronic[37] conductivities of LBF single crystals by ^{19}F NMR, impedance spectroscopy and various electrochemical techniques. The effect of the homogeneous doping of LaF_3 by BaF_2 on the ionic conductivity is shown on **Figure II.3**. Small amounts of BaF_2 ($\approx$ 0.05 – 0.10 mol%) dramatically increase the conductivity by more than one order of magnitude. There exist a maximum conductivity for a determined concentration of aliovalent ions. In the case of $La_{1-x}Ba_xF_{3-x}$ single crystals the maximum seems to be situated around $x = 0.07$.
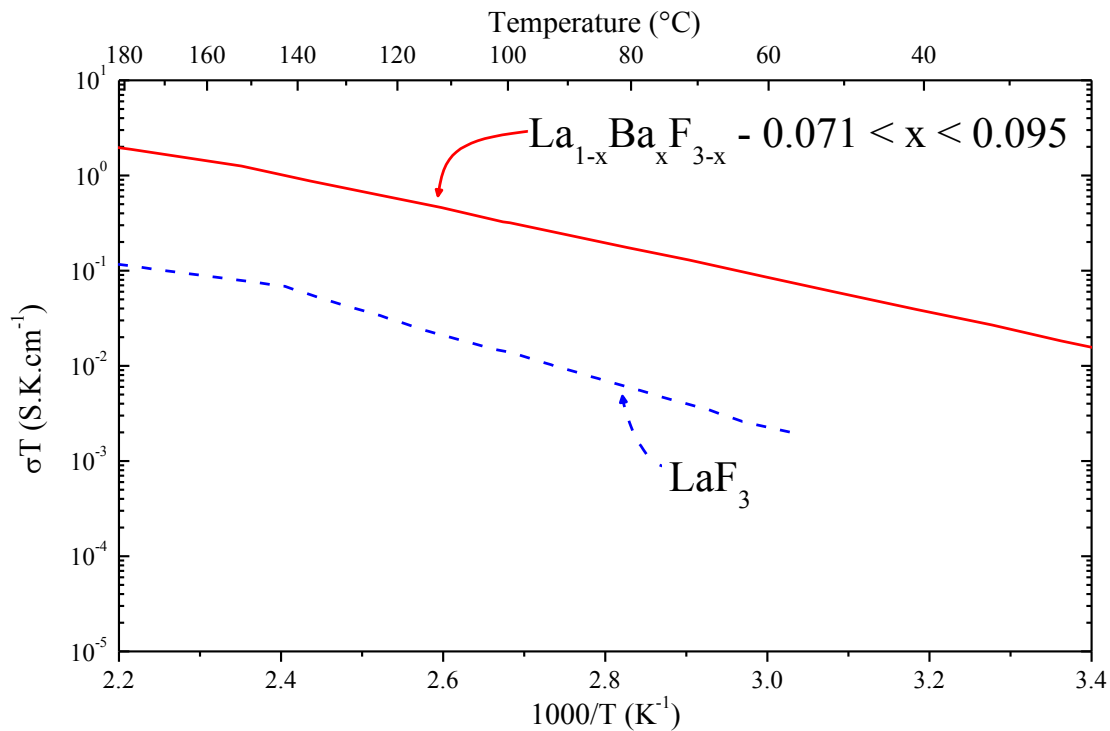
Figure II.3. *Arrhenius plot of the bulk ionic conductivity of single crystals of LaF₃ and La₁₋ₓBaₓF₃₋ₓ (0.071 < x < 0.095) perpendicular to their c axis. Data gathered from Roos et al.[45]*

Hebb-Wagners polarization experiments were carried out on LBF single crystals at different temperatures and for two compositions, in order to determine their electronic conductivity[37]. The authors used metallic La as reversible electrode and Pt as blocking electrode. It revealed that the electronic conductivity in LBF relies on electron conduction rather than by holes, with a maximum electronic conductivity of 10^{-4} S.cm^{-1} at 373K for $x = 0.013$. When compared to the ionic conductivity of 4.2×10^{-2} S.cm^{-1} for the same sample, it yields an ionic transference

number $t_i \approx 0.9976$ which is close to unity. It suggests that little electronic leakage should take place in the electrolyte[46]. Moreover, Hebb-Wagners technique is a tricky method with many limitations which can potentially yield largely overestimated values.

3.2. Recent work with polycrystalline samples

Most in-depth conductivity studies made on solid fluoride-conducting electrolytes were carried out on single crystals where the conduction properties are the same along one direction of the crystal. Even if the conduction properties can sometimes be anisotropic, they are entirely different when polycrystalline samples are used, due to the exceptional surface properties of materials. Single crystals are costly to produce and cannot be implemented in practical electrochemical devices. Polycrystalline powders are generally used instead[47]. The ionic conductivity is then dependent on the microstructure of the polycrystalline material, as conduction properties are different in the grain boundaries and in the bulk.

Polycrystalline solid electrolytes, especially when downsized to the nanoscale, present conduction properties that are radically different from their monocrystalline counterpart. This can be explained by the profoundly different properties of the bulk, which generally presents the same conduction properties than a single crystal (if there is no significant anisotropy in the conductivity of the single crystal), and the surface, where many defects are present at the grain boundaries. This effect can either be detrimental or beneficial to the conduction properties, depending on whether the conduction is faster in the grain boundary or in the bulk of the structure[48]. This is illustrated by **Figure II.4** which shows detrimental (tysonite-type LBF) or beneficial (fluorite-type $Ba_{0.6}La_{0.4}F_{2.4}$) contribution of the nanostructuration.
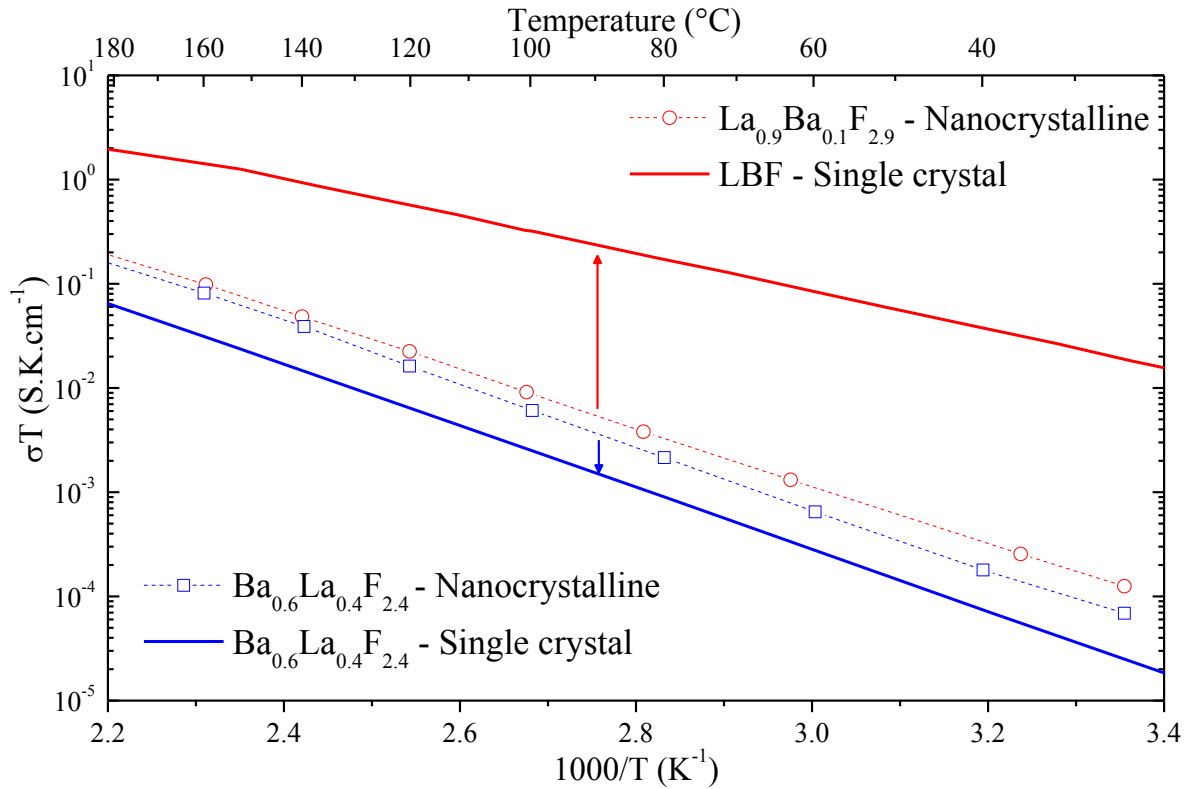
Figure II.4*. Arrhenius plot of the conductivities of compacted nano-powders of $La_{0.9}Ba_{0.1}F_{2.9}$ and $Ba_{0.6}La_{0.4}F_{2.4}$[34]. The conductivity of single crystals of $La_{1-x}Ba_xF_{3-x}$ (x ≈ 0.071 – 0.095) and $Ba_{0.6}La_{0.4}F_{2.4}$ is added for comparison[45].*

These grain boundary effects are often described as happening in the *space charge layer/region (scl)*, where local domains can present unique electrical properties. The concept was first used by Carl Wagner[49] to predict the conductivity of semiconductors (metal oxides) involving inclusion of another phase (metal or metal oxides) yielding clouds of excess electronic charges (electrons & holes). It is of particular interest in semiconductors, and particularly p-n junctions, as their operation relies on this space charge effect where a local interfacial loss of the electroneutrality takes place at the p-n junction.

The scl can be logically extended to the field of solid-state ionics as the local region of redistribution of point defects can also involve ionic charges. These effects are boundary layer phenomena and do not happen in the bulk, unlike homogeneous doping. The scl is, to some extent, the solid equivalent of the interfacial double layer that forms in liquids, where charges locally rearrange at the solid/liquid interface. Excess charges, for instance fluoride vacancies, can form at the interface/grain boundary, to yield exceptional conduction properties.

Mathematical calculations to predict the behavior of charge transport in the scl have been carried out with relative success for the past decades, particularly by J. Maier.[50] The scl effect is particularly well illustrated by his work with nanometer-scale CaF_2/BaF_2 films.[51] A periodic succession of CaF_2/BaF_2 thin films offers F^- conductivities several orders of magnitude higher than the bulk materials taken individually, due to the creation of space charge layers offering high conductivity pathways parallel to the interfaces.

3.3. Effect of sintering

Another approach to increase the conductivity of an electrolyte is to bypass the grain boundary conduction, which can be deleterious to the conduction properties, by merging the grains together. Indeed, the bottleneck effects created by the low contact area between the grain boundaries of polycrystalline samples can be detrimental to the conduction properties of polycrystalline samples. Hence, reducing porosity to obtain a dense solid is crucial to obtain efficient conductivity in polycrystalline samples. This process is called sintering, and is illustrated in **Figure II.5**. The sample is heated to a sufficient temperature (lower than the fusion temperature) to allow atoms to diffuse across the grains. The Ostwald ripening process leads to grain growth and fusing of the grain boundaries, leading to the formation of favorable intergranular conduction pathways that can provide better conduction properties.

While the conduction is limited by the migration of the ionic species in the grain boundaries for the powder processed by uniaxial pressing, it is the bulk of the grains that ensure the overall conduction in sintered samples.

Grain boundary limited conduction   *Bulk limited conduction*

ΔT
Sintering
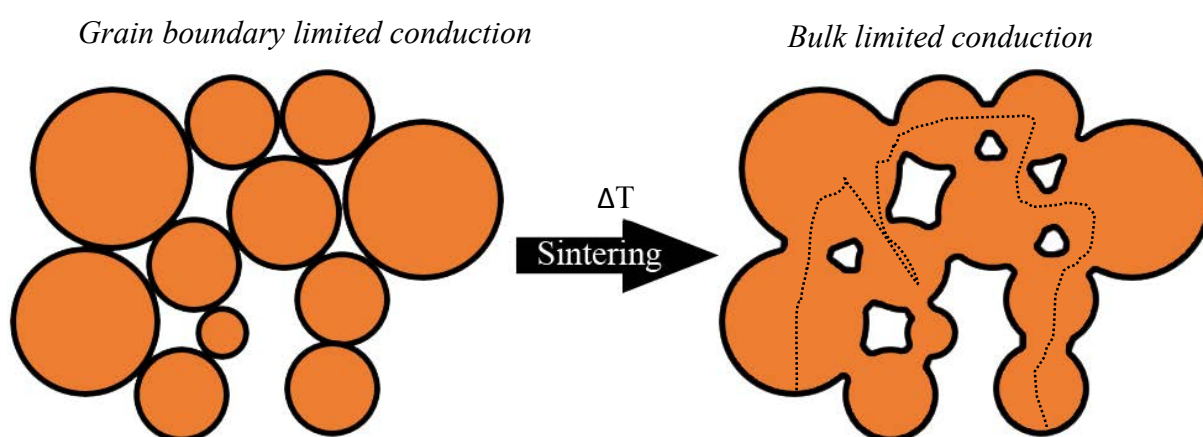
Figure II.5. *Schematic representation of a compact powder before and after a sintering process. The grains are represented in orange and the grain boundaries in black.*

Thus, the sintering process is beneficial to the conduction properties only if the conduction is faster in the bulk than in the grain-boundary, as it is the case in tysonite-type LBF. **Figure II.6** represents the conductivity of samples of $La_{0.9}Ba_{0.1}F_{2.9}$ (tysonite-type) prepared by powder compacting or by sintering, as presented by Rongeat *et al.*[34] For sintering, the pressed LBF powder was heated in Ar atmosphere at 800 °C for 2 hours.
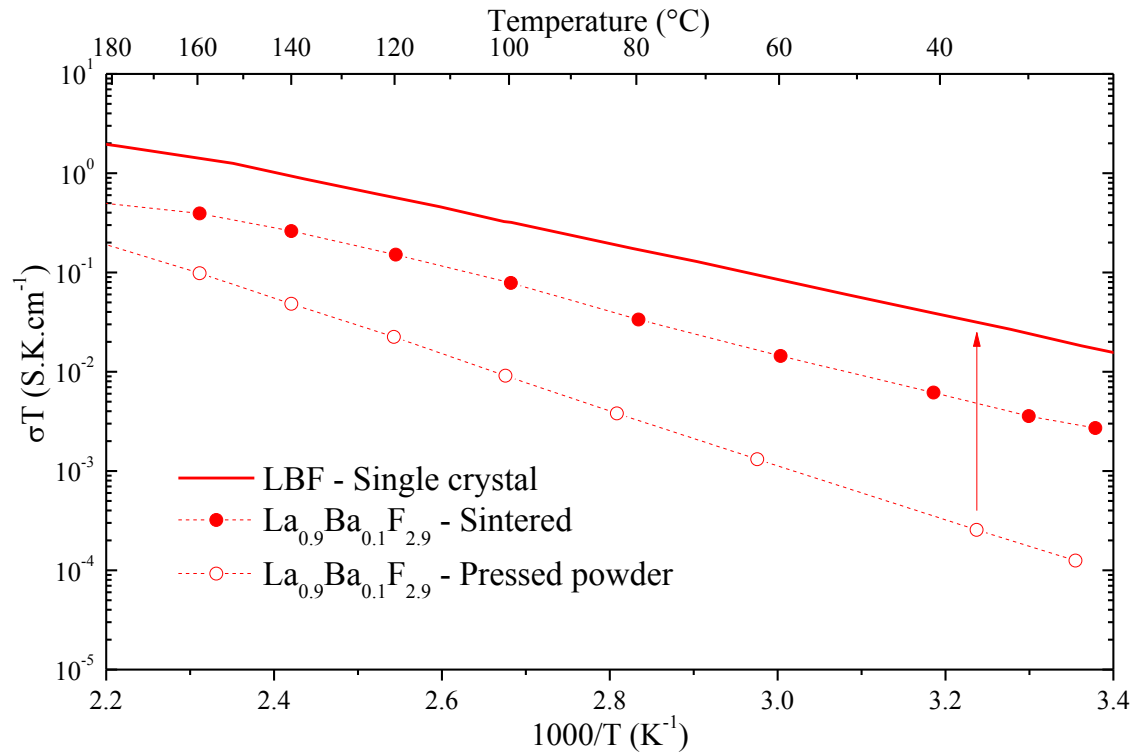
Figure II.6. *Arrhenius plot of the conductivity of compacted nano-powder and sintered samples of of $La_{0.9}Ba_{0.1}F_{2.9}$. [34] The conductivity of a single crystal of $La_{1-x}Ba_xF_{3-x}$ ($x \approx 0.071 – 0.095$) is shown for comparison purpose.[45]*

The conductivity is dramatically increased by the sintering process in LBF samples. The bulk ionic conductivity is higher than the grain boundary conductivity and the sintering process is beneficial to the conduction properties. Inversely, nanostructuration of LBF is detrimental, as it will have for effect the apparition of additional boundaries in which conduction is worse than in the bulk.

This makes the use of sintered LBF in FIBs a very attractive process. However, in a typical all-solid-state battery, to ensure intimate contact between the components and to limit interfacial impedance[52], the anode|electrolyte|cathode stack is generally shaped by compaction of

powdered materials in bulk-type solid-state batteries[53], [54], or by successive deposition of thin films in solid-state microbatteries.[55] Accordingly, the sintering of the electrolyte in practical conditions is complicated because it involves the sintering of the whole battery stack in a single step. For instance, the assembly of solid-state Li-ion batteries by spark plasma sintering (SPS) was recently proposed to generate a monolithic battery exhibiting promising electrochemical performance.[56], [57] The different chemical and physical properties of the materials composing the stack, and their reactivity towards each other at increased temperature, demands a careful selection of the materials beforehand. The result is very promising in terms of electrochemical performance, and it might be applicable to FIBs.

For a comprehensive evaluation of the sintering and nanostructuration parameters on the conduction properties of LBF, please refer to the thesis work of J. Chable[43].

3.4. Comparison with lithium solid electrolytes

It is interesting to compare electrolytes for FIBs with state of the art electrolyte for LIBs. It is worth noticing that, in a contradictory way, investigations focusing on the electrical properties of solid state electrolytes are habitually carried out on sintered samples while in practice, most solid-state batteries employ electrolyte layers processed by a simple compacting process. In most cases, sintering the electrolyte is highly desirable to increase its conductivity, and more efforts should be made to implement this approach in practical systems.

Despite this contradiction, sintered electrolytes offer a convenient approach to compare the conductivity of Li^+ and F^- electrolytes (**Table II.1**). LBF presents conductivities below that of the current best Li^+ SSEs, namely c-LLZO for oxides, and LGPS for sulphides, with conductivities 1 to 3 orders of magnitude inferior. It does however surpass LiPON which has been successfully used in commercial microbatteries for several years now[58].

Electrolyte	Mobile ion	σ @ RT (S.cm^{-1})	Reference
La$_{0.95}$Ba$_{0.05}$F$_{2.95}$	F$^-$	4.5×10^{-5}	Chable *et al.* [41]
La$_{0.9}$Ba$_{0.1}$F$_{2.9}$	F$^-$	2.7×10^{-5}	Chable *et al.* [41]
La$_{0.9}$Ba$_{0.1}$F$_{2.9}$	F$^-$	1.2×10^{-5}	Rongeat *et al.* [34]
β-PbSnF$_4$	F$^-$	*$(1\text{-}2) \times 10^{-3}$	Sorokin *et al.* [59]
c-Li$_7$La$_3$Zr$_2$O$_{12}$ (c-LLZ)	Li$^+$	$(2-3) \times 10^{-4}$	Thangadurai *et al.* [60]
Li$_{10}$GeP$_2$S$_{12}$ (LGPS)	Li$^+$	1.2×10^{-2}	Kamaya *et al.* [61]
Li$_x$PO$_y$N$_z$ (LiPON)	Li$^+$	2×10^{-6}	Luntz *et al.* [52]

Table II.1. *Room temperature ionic conductivity of state of the art F$^-$ and Li$^+$ **sintered** solid electrolytes. *Value for a "monolith"; to the best of my knowledge, no data on sintered samples of PbSnF$_4$ is available. Polycrystalline PbSnF$_4$ samples can exhibit conductivity as high as 10^{-2} S.cm^{-1} at RT[59].*

This justifies the need to heat the FIB to temperatures where the LBF conductivity can reach that of the Li electrolytes at RT. LBF shows a conductivity of about 10^{-4} S/cm at 150 °C which should be sufficiently high to employ similar current densities than typical lithium solid state batteries.

Looking at the table, one might think that β-PbSnF$_4$ is better suited for FIBs as it presents high ionic conductivity, especially when considering polycrystalline samples. For instance, LBF10 and β-PbSnF$_4$ polycrystalline samples present RT ionic conductivities of 4.2×10^{-7} and 3×10^{-2} S.cm^{-1}, respectively[34], [62].

Unfortunately, β-PbSnF$_4$ is not suited as high voltage electrolyte for FIBs due to its low electrochemical stability, which brings us to the next section.

3.5. Electrochemical stability

The electrochemical stability of the electrolyte is linked to its electrochemical decomposition potential, or reduction potential. It can be calculated from its thermodynamic properties by considering the following decomposition reaction:

$$MF_{x\,(s)} \rightarrow M_{(s)} + \frac{x}{2} F_{2\,(g)} \qquad\qquad 44.$$

Table II.2 gives the calculated decomposition potential in standard conditions of some metal fluorides that could potentially be used as solid electrolytes in their pure form, or as dopant.

The calculations were done using the thermodynamic considerations presented in **Chapter I.1.2.1**.

MF_x	Structure type	ΔE_d (V)
CeF_3	Tysonite	5.73
LaF_3	Tysonite	5.73
BiF_3	Orthorombic (*Pnma*)	2.87
SrF_2	Fluorite	6.00
BaF_2	Fluorite	6.00
CaF_2	Fluorite	6.10
β-PbF_2	Fluorite	3.27
α-SnF_2	Monoclinic (C2/c)	3.41
β-$PbSnF_4$	Tetragonal	3.32

Table II.2. *Theoretical decomposition potentials of various metal fluorides that could potentially be used as solid electrolyte or electrolyte dopant for FIBs. Thermodynamic values used for the calculations were taken from www.materialsproject.org, except for α-SnF$_2$ and β-PbSnF$_4$, where values were taken from ref* [63].

$PbSnF_4$, BiF_3, PbF_2, and SnF_2 show decomposition potentials which are considerably lower ($\approx$ 3.2 – 3.6 V) than CeF_3, LaF_3, SrF_2, BaF_2, and CaF_2 ($\approx$ 5.7 – 6.1 V). Since the electrolyte is largely present in the electrode composite (60 wt%), the former are not good candidates to be used as electrolyte as they could potentially be reduced before the active material, even if they are present in a few mole percent level as dopant (e.g. BiF_3). They could be used in cells provided that the operating potential is below the corresponding decomposition potential.

They are however interesting candidates as active material as they present fluoride conduction properties. For example, BiF_3 was used as cathode in FIBs vs. Ce metal and the cell was successfully cycled dozen of times[14].

To further discuss the decomposition mechanism of LBF, one can refer to the work of Bezmelnitsyn *et al.*[64], who took interest in the decomposition of metal fluorides, particularly LBF, as a way to produce pure fluorine by solid-state electrolysis. They used LBF (x $\approx$ 0.03 – 0.10) pellets and deposited metal (Ni, Cu or Ni) or graphite on each face, before applying a

galvanostatic current of 1.0 mA to the cell. The cell was placed in a vacuumed chamber linked to a mass spectrometer, which revealed F_2 and HF gases evolution. They also observed the formation of dendrites at the LBF interface in contact with the negative electrode. XPS analysis of the dendrites showed that it was a mixture of La and Ba metal with a Ba/La ratio corresponding to that in the LBF. As for F_2 evolution, Bezmelnitsyn et al.[64] propose a recombination type mechanism between holes h^+ and fluoride ions F^- to yield elemental fluorine F^0, which then recombines to form F_2.

In conclusion, it is important to carefully check all possible redox reactions that would involve the electrolyte, and operate the cell in a safe potential window where the electrolyte will remain intact.

4. Electrical properties and electrochemical stability of tysonite-type Ba-doped LaF₃ electrolyte and its carbon composite in solid-state fluoride-ion batteries.

This section focuses on the electrical and electrochemical properties of LBF and LBF-C composites. The electrochemical stability of LBF is investigated as no such investigation can be found in the literature. LBF-C composites were studied to evaluate the interaction of carbon and LBF within the electrode composites.

4.1. Introduction

All-solid-state batteries are attractive electrochemical devices, owing to the use of inherently safer solid electrolytes. Indeed, conventional battery technologies present safety concerns as a rupture of the cell package could lead to the leakage of the corrosive and flammable liquid electrolyte.

Several criteria must be fulfilled for a material to be successfully used as solid electrolyte. Firstly, it must present high ionic conductivity to ensure the fast transport of ions to the electrodes. In addition, it must also exhibit a low electronic conductivity to avoid short circuit and self-discharge of the cell. Finally, the electrolyte must be electrochemically stable within the potential window at which the battery is operated, so that long-lasting cycle life can be achieved.

Despite the efforts made by the scientific community to develop solid electrolytes capable of ionic conductivities equivalent to those of liquids[61], the high-rate capability of cells employing such electrolytes remained inferior[54]. These efforts have recently been directed towards the understanding of the cause of these inferior performances by focusing on interfacial phenomena.[65]–[67] It is now fair to say that the principle obstacle for developing all-solid-state batteries capable of delivering relatively high current densities relies in the achievement of low resistance interfaces[52]. Electrochemical stability of the electrolyte and electrochemical compatibility with the cell components is crucial to avoid the formation of interphases and layers that can significantly impede mass and/or charge transport.

Comparable observations can be made for solid electrolytes for fluoride-ion batteries (FIBs) that can potentially face similar interfacial issues encountered in lithium solid-state-batteries. It is therefore of crucial importance to understand the electrochemical stability of fluoride-ion solid electrolytes. Additionally, the interaction of the fluoride ions with the carbon present in

the electrode composite might be an issue. Indeed, the possible fluorination of carbon to yield insulating carbon fluoride $(CF)_n$ needs to be addressed.

The electrochemical stability of lithium electrolytes is generally performed using Li metal as a pseudo-reference electrode. No such equivalent exists for FIBs, as the element form of fluorine is fluorine gas F_2. Consequently, we evaluated the use of lithium as pseudo-reference in the study of the electrochemical properties of Ba-doped LaF_3, $La_{1-x}Ba_xF_{3-x}$ (LBF), a fast fluoride conductor of tysonite-type structure (trigonal, P-3c1).

LBF seems to be a good candidate for all-solid-state FIBs. Nanocrystalline LBF compacted powders prepared by ball-milling exhibit relatively high ionic conductivity (about 10^{-4} S.cm^{-1} at 160 °C) and can be used in FIBs as solid electrolyte[14], [29], [30]. It is well-known that doping LaF_3 with bivalent fluorides like BaF_2 dramatically increases the F^- interstitial conduction according to a Schottky mechanism[34], [37], [41], [42], [45]. The maximum conductivity of LBF seems to be achieved for $0.05 < x < 0.10$. We performed electrochemical investigations using $La_{0.95}Ba_{0.05}F_{2.95}$.

Here, we report the first investigation of the electrochemical stability of a solid fluoride electrolyte. Examination of the Li|LBF interface by time-resolved electrochemical impedance spectroscopy shows that lithium is a suitable electrode to probe the electrochemical properties of fluoride-ion solid electrolytes. Electrochemical stability investigations performed on Li|LBF|Pt cells are corroborated by thermodynamic calculations.

Additionally, a composite formed of a mixture of LBF and carbon black (LBF-C) was employed to study the possible interaction of carbon with fluoride ions. Electrochemical investigations of the LBF-C composite suggest the formation of carbon fluorides. Experimental results obtained on cells using the LBF-C composite are supported by thermodynamic calculations.

4.2. Experimental

4.2.1. Preparation of the materials

Unless specified, all the manipulations of the materials and assembly of the cells were carried out in a dry Ar glove box ($H_2O < 2$ ppm).

All powdered materials were outgassed for 12 hours at 150 °C in a vacuumed atmosphere, then placed in the glove box without any contact with air.

$La_{0.95}Ba_{0.05}F_{2.95}$ (LBF) electrolyte was prepared by our colleagues J. Chable and A. Gil-Martin (IMMM, Le Mans) by ball-milling stoichiometric amounts of LaF_3 (Alfa Aesar, 99.99 %) and BaF_2 (Strem chemicals, 99.99 +%) in Ar atmosphere. The powders were placed in the airtight milling bowl inside the glove box then taken out for milling. A Fritsch mini pulverisette 7 premium line planetary mill with ZrO_2 grinding bowls and ZrO_2 grinding balls (10 mm diameter) was used. To produce 4 g of LBF, the mixture was ball-milled for a total of 12 hours (48 cycles of 15 min with 15 min pauses) at a rotational speed of 400 rpm.

The LBF-C composite was obtained by an additional milling step using the obtained LBF05 powder and carbon black (Pure Black, Superior Graphite), in a 9:1 wt % ratio. The mixture was ball-milled in similar conditions as LBF, for 4 additional hours.

Lithium foil (Sigma Aldrich, 99.9%) was cut into ⌀10 mm discs with a punch. The lithium discs were then placed on a stainless steel disc (coin cell spacer) and slightly pressed with a clamp using a custom-made stainless steel die and rod. To avoid contamination, the surface of the lithium was protected using a polyethylene sheet previously degreased with ethanol. The process resulted in a lithium disc of about ⌀12 mm presenting a smooth, flat surface, attached to the coin cell spacer.

Platinum foil was punched to ⌀15 mm Pt discs. The discs were then polished with P2400 SiC abrasive paper, then rinsed with ethanol and deionized water.

Graphite disks (Cg) were cut from high purity graphite rods (Mersen). Graphite rods were previously machined to reduce their diameter so that they would fit the pressing mold. The discs were then polished with grit P400 SiC abrasive paper, degreased in acetone then sonicated three times in ultra-pure water for *ca.* three minutes. Typical thickness of the graphite discs was 0.5 – 0.7 mm.

The preparation of the Pt and Cg disks were carried out in air atmosphere.

Commercial Ag conductive paint (RS Components) was painted on the LBF surface to give the Ag semi-blocking electrodes. The pellet was then outgassed at 150 °C in vacuum for 12 h.

4.2.2. Cell assembly

All pellets were assembled in the dry Ar glove box by cold pressing the LBF powder, or powder stacks, in a ⌀10 mm stainless steel die with an uniaxial press (Specac Atlas), at a load of 5 tons.

The Li|LBF|Pt cell was obtained by placing the pressed LBF pellet (300 mg) between a Li and Pt disk, which were prepared as previously described.

The Cg|LBF-C|Cg cell was obtained by pressing LBF-C powder (30 mg) directly between the Cg disks. For the Ag|LBF|LBF-C|LBF|Ag cell, 30 mg of LBF-C and 300 mg of LBF were used for each layer. Each powdered layer was poured in the pressing die and gently flattened using a stainless steel rod, before pressing of the complete stack. The LBF|LBF-C|LBF stack was then painted with Ag on each side of the pellet. Finally, the pellet was outgassed under vacuum at 150 °C overnight.

For the Li|LBF|LBF-C and Li|LBF|C cells, 15 mg of LBF-C and 5 mg of C were pressed between the LBF and a Cg disk to form LBF|LBF-C|Cg and LBF|C|Cg stacks. The stacks were then laid on a Li disk.

All cell preparation and assemblies were carried out in a dry Ar glove box. The stacks described above were mounted in modified CR2032 coin-cells. A flat PTFE washer of the desired thickness was used to maintain the stack at the center of the coin cell. A flat spring was used to maintain electrical between the stack and the coin-cell case. Spacers (stainless steel disks) were used to adjust the thickness of the pellet stack to the space available in the coin-cell. The crimped coin-cells were then tightened on a custom made electrochemical test bench employing a screw system, so that the stacks could remain under constant pressure for the duration of the electrochemical measurements. The test bench was placed in an oven set to 30 °C. The cells were left at the designated temperature for at least 3 hours before electrochemical measurements so as to reach equilibrium.

4.2.3. Electrochemical measurements

4.2.3.1. Impedance measurements

For electrical investigations of LBF and LBF-C, EIS was recorded in the 13 MHz – 5 Hz frequency range, with a HP 4192A LF impedance analyzer, or in the 300 kHz – 3 mHz frequency range, with a BioLogic VSP equipped with a low current extension. The frequency range in which the electrical properties can be observed is dependent upon the temperature at which the recordings are carried out. The 300 kHz – 3 mHz range is sufficient for low temperature measurements but as temperature increases, the frequencies shift to higher values and the beginning of the relevant electrochemical process is only partially visible. The 13 MHz – 5 Hz frequency range then becomes relevant.

The amplitude of the sinusoidal potential excitation was adjusted in the 43 mV – 300 mV range depending on the impedance of the cell. The adequate amplitude was chosen after checking that the linearity of the measure was achieved in the aforementioned amplitude range.

In all experiments, the EIS recording started 3 hours after the temperature was set in order to avoid transient processes.

Impedance spectra were fitted using EC-Lab Zfit with the relevant equivalent circuit presented in the discussion.

4.2.3.2. Cyclic voltammetry

The cyclic voltammetry experiments were recorded at 30 °C with a BioLogic VSP potentiostat channel equipped with a low current extension. All experiments were carried out at a scan rate of 0.1 mV.s^{-1} between 7 V and -0.2 V, starting from OCV. The CV recording started 3 hours after the cell was first placed at 30 °C in order to avoid transient processes.

The ohmic drop was corrected by using the resistance of the electrolyte determined from EIS measurements. The current density, rather than the current, was used to allow comparison of the cells during the investigation of the chemical compatibility of LBF with carbon. The contact area A of the LBF|WE (working electrode) developed at the interface was estimated using the relation :

$$A = \frac{L}{\sigma_i(LBF).R_{gb}}$$

45.

With L the thickness of the LBF layer, σ_i the LBF conductivity at 30°C determined from conductivity measurements on the Ag|LBF|Ag cell, and R_{gb} the resistance of the electrolyte (coming grain boundaries) determined from EIS measurements on the relevant cell. The thickness of the electrolyte was assumed to be the same for all experiments as the same mass of LBF (300 mg), and identical pressing force (5 t) was employed in all experiments.

4.2.4. Characterization

4.2.4.1. X-ray diffraction

Conventional powder XRD measurements were performed with a Rigaku Ultima IV diffractometer with a Cu Kα radiation (λ = 1.5418 Å), at a 2θ scan rate of 0.1°/min and a step of 0.017°, between 10° and 80°.

4.3. Results and discussion

4.3.1. Structural and electrical properties

The synthesis of $La_{0.95}Ba_{0.05}F_{2.95}$ (LBF05) was performed by Johann Chable and Ana Gil Martin (IMMM, Le Mans), by ball-milling stoichiometric amounts of outgassed LaF_3 and BaF_2 commercial powders under argon atmosphere.

The XRD pattern of the as-milled LBF05 powder is shown in **Figure II.7**. All peaks could be indexed by a single LaF_3 phase exhibiting a tysonite-type structure (trigonal, P-3c1) with peaks slightly shifted from the reference, suggesting the effective incorporation of BaF_2 in the structure of LaF_3 to form a solid solution, as confirmed by NMR ^{19}F experiments[43].
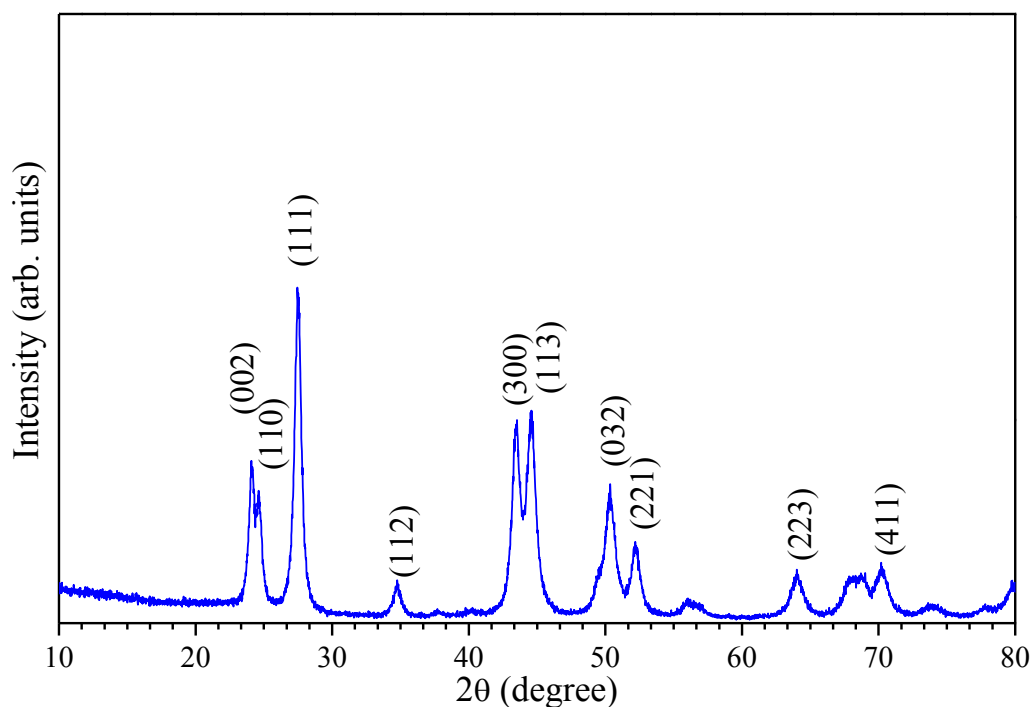
Figure II.7. *X-ray powder diffraction diagram of the ball-milled LBF05. All peaks could be indexed by a tysonite-type structure (trigonal, P-3c1), some of which are shown.*

The crystal structure of tysonite-type LaF_3 is represented on **Figure II.8**. The structure.can be described as a succession of $_\infty[LaF]^{2+}$ slabs containing F2 and F3 ions, inbetween $_\infty[F]^{-2}$ slabs containing F1 ions, along the c axis[43].
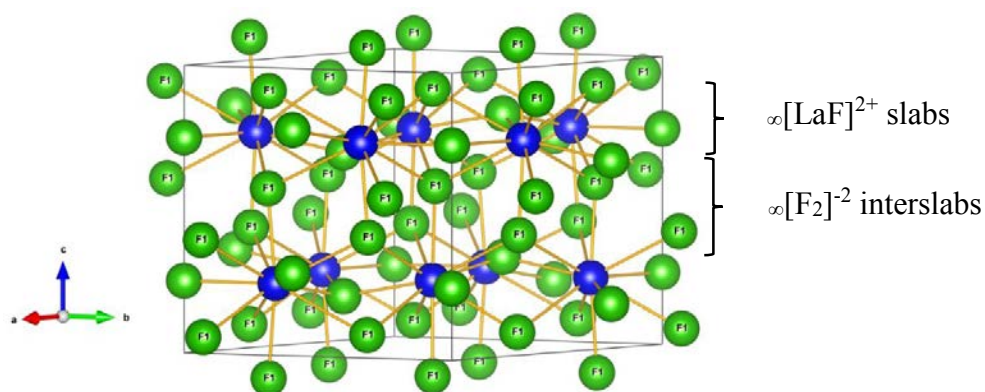
Figure II.8. *Crystal structure of tysonite-type LaF$_3$ (trigonal, P-3c1). The blue balls represent La^{3+} and the green balls F$^-$ ions.*

In the case of LBF, the crystal structure remains identical but is slightly distorted along the a and c axis due to La^{3+} cations being partially substituted by the larger Ba^{2+} cations. This substitution induces the formation of additional F$^-$ anionic vacancies in a typical Schottky mechanism, which leads to a dramatic increase of the electrical conductivity.

Rietveld refinements resulted in cell parameters (a = b = 7.205 (1) Å and c = 7.371 (1) Å) and mean crystallite size (about 13 nm) in good agreement with previously reported values[34] (a = b = 7.20 Å and c = 7.37 Å, 14 nm crystallite size.)

The electrical properties of the prepared LBF05 powder was investigated by electrochemical impedance spectroscopy, using Ag semi-blocking electrodes (**Figure II.9**). All of the recorded impedance spectra exhibit the characteristic Nyquist (complex) plot exhibited by solid electrolytes in contact with ionically blocking electrodes[68]. The data can be separated into two contributions: a high-frequency semicircle and a low frequency tail.
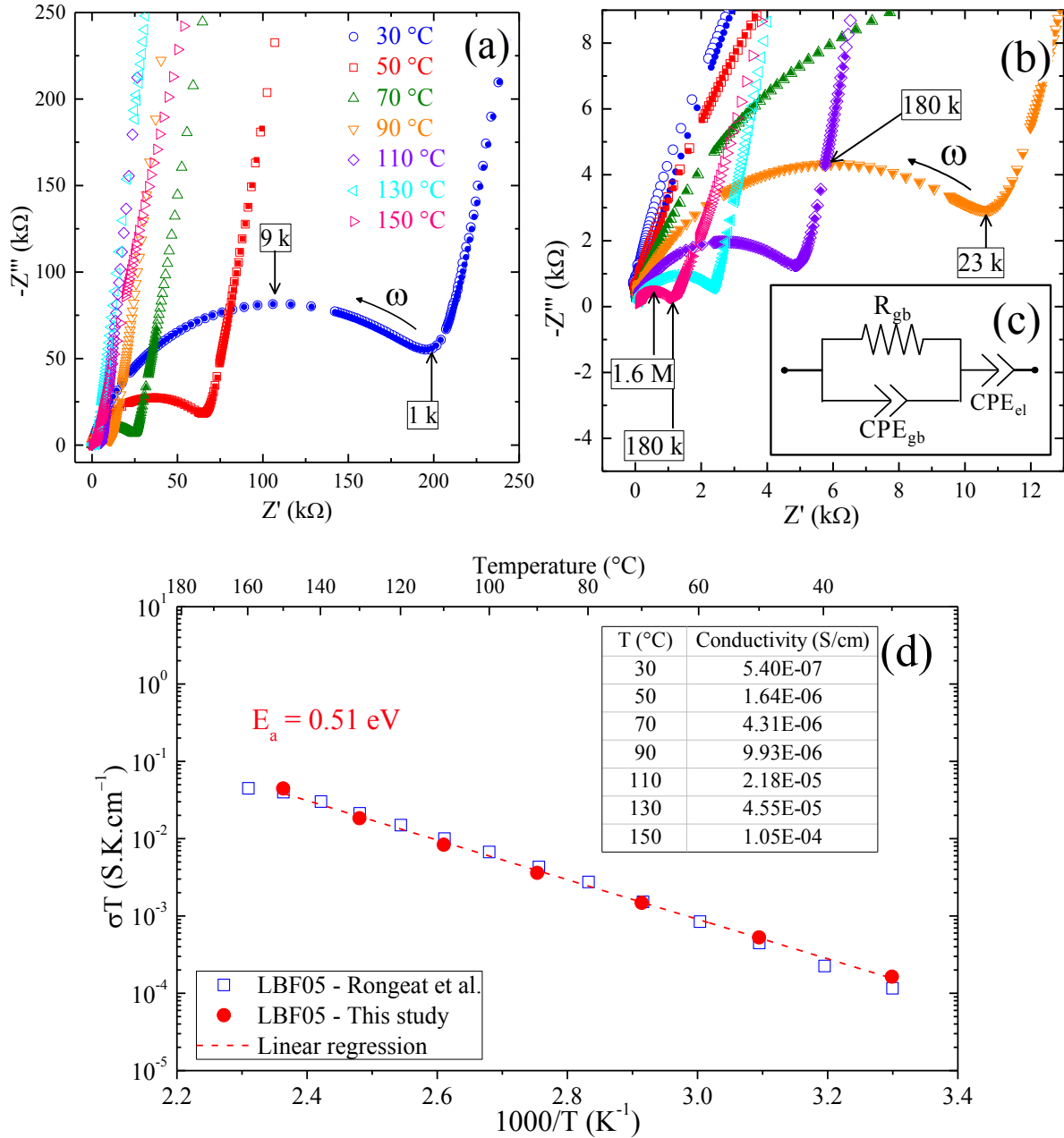
Figure II.9. *(a) Nyquist plot of the impedance spectra recorded on Ag|LBF|Ag pellets between 30 and 150 °C and (b) zoom in on the high frequency region. The open symbols represent the data and the closed symbols represent the fit obtained. (c) The equivalent circuit used to fit the impedance spectra. Arrhenius plot of the conductivity of LBF05 and comparison with data previously reported for the same composition.[34] The dashed line represents the fit obtained to calculate the activation energy. A table giving the values of the conductivity (S/cm) for each temperature (°C) is added for convenience.*

The semicircle at high frequencies represents the bulk impedance of the electrolyte[69]. It corresponds to the electrical resistance of the electrolyte in parallel with its capacitance (R//C). Considering that the electrolyte is simply pressed without additional annealing or sintering

process, the resistance of the electrolyte can be ascribed solely to intergranular resistivity due to the grain boundaries and is thus denoted R_{gb}[34]. The intragranular or "bulk" resistance of the electrolyte, which can be roughly extrapolated as the resistance of a single crystal of the same dimensions than our sample, is not visible on the impedance diagram, as it usually the case with sintered samples. This is explained by the fact that its resistance is masked by the semicircle generated by the comparatively large resistance of the grain boundaries R_{gb}, which is about 2 orders of magnitude higher than the expected intergranular resistance.

The geometrical capacitance of the electrolyte rises from its dielectric relaxation time[70]. However, considering that the semi-circle is slightly depressed, it indicates that the geometrical capacitance cannot be modeled by a purely capacitive contribution ($Z_c = \frac{1}{j\omega C}$) but rather by a constant phase element ($Z_{CPE} = \frac{1}{(j\omega)^\alpha Q}$). CPEs can be used to model a continuous distribution of time constants within the material[71]. This is attributed to the polycrystalline nature of the sample and the presence of grain-boundaries as impedance spectroscopy studies carried out on single crystal often present purely capacitive contributions[69]. The capacitance of the electrolyte is thus denoted CPE_{gb}.

The low frequency tail corresponds to the capacitive effects owed to the accumulation of electric charges at both Ag|LBF blocking interfaces which are combined in a single contribution. The tail is not perfectly vertical as expected for a pure capacitance, but is instead tilted, which is due to the roughness of the Ag|LBF interface inducing a continuous distribution of relaxation times. The electrodes' capacitance is thus denoted CPE_{el}.

The presence of a single semi-circle accompanied by a low frequency tail is indicative that no significant electronic leakage takes place at the LBF's grain boundaries. Significant electronic conductivity would be noticed by the disappearance of the capacitive tail, as capacitive effects at the electrodes would be short-circuited. Instead, a semi-circle corresponding to the electronic conductivity of the sample would be observed[46]. These observations confirm the ionic transference number close to unity obtained for LBF single crystals[37].

However, it is interesting to point out that when going to very low frequencies ($< 10^{-1}$ Hz), the capacitive tail sometimes shows deviation from linearity (not shown) to suggest the beginning of a RC (or RCPE) semi-circle of very large resistance (several MΩ). This effect can be ascribed to surface layers or electrode effects depending on the value of the effective capacitance[68] which can be calculated from the electrolyte resistance and CPE[71]. The calculated effective capacitance for this second semicircle is about 8×10^{-9} F which is consistent with the presence

of a surface layer. This is why Ag is referred as a semi-blocking electrode. Note that same phenomena were observed with Au sputtered electrodes, yielding similar capacitance values.

The resistance of the electrolyte R_{gb} is obtained by fitting the impedance data using the equivalent circuit presented in **Figure II.9** (c). The ionic conductivity σ can be then calculated using the relation $\sigma = \frac{1}{R_{gb}} \times \frac{l}{A}$ with l and A being the thickness and surface of the LBF pressed pellet. The density of the pellet was 79 % of the theoretical density of LBF05 (5.885 g.cm^{-3}). The temperature dependence of the conductivity is shown on a typical Arrhenius plot (**Figure II.9**d), with values in good agreement with previously reported data for polycrystalline samples of characteristics similar to our experimental conditions.[34] The activation energy calculated from the slope of the linear regression yields a value of 0.51 eV which is in relatively good agreement with the value of 0.55 eV reported by the same authors.

4.3.2. Electrochemical stability

The determination of the electrochemical stability window of electrolytes is crucial to evaluate the potential window in which the cell can be operated without degrading the electrolyte. In lithium batteries, the electrochemical stability window refers to lithium metal acting as a reference. Since the elemental form of fluoride is fluorine F_2, a highly toxic and corrosive gas, a suitable reference is needed to study and establish the electrochemical stability window of potential electrolytes for FIBs.

In this scope, lithium metal offers practical advantages such as a relatively low oxygen sensitivity (especially compared to lanthanum), and softness, providing good contact with the solid electrolyte. Moreover, in contact with fluoride solid electrolytes such as LaF_3 (or BaF_2), lithium can react yielding LiF and metallic La (or Ba). The Gibbs free energies of the corresponding reactions:

$$MF_x + Li \rightarrow xLiF + M \qquad\qquad\qquad 46.$$

indicate that the reaction occurs spontaneously ($\Delta_rG° = $ -120 kJ/mol and -15 kJ/mol, $\Delta E° = $ 0.355 V and 0.079 V for LaF_3 and BaF_2, respectively) in standard conditions. The formation of a LiF/Li interface can provide a reference redox couple as long as the interface is not entirely blocking. We refer as it being a counter electrode as the electrochemical investigations presented here are carried out in a two-electrode setup, lithium being both the counter and reference electrode.

The formation and electrical properties of a LiF/Li interface was monitored by time-resolved electrochemical impedance spectroscopy (EIS) investigations performed on a Li|LBF|Li cell (**Figure II.10**.)

After 3 hours of contact, the impedance spectrum exhibits a semi-circle characteristic of the electrolyte's resistance, and an additional semi-circle, followed by the capacitive tail. It should be noted that the electrolyte resistance R_{gb} is slightly inferior using Li electrodes when compared to painted Ag electrodes, which might be due to the Li metal overlapping the sides of the pellets upon assembly of the cell, thus increasing the contact area A, and consequently decreasing R_{gb}. Over time, the resistance of the first semi-circle is stable, while the resistance of the second semi-circle increases. The fitting of all spectra was carried out with the equivalent circuit presented on **Figure II.10 (c)**. The resistances of the two semi-circles, gathered from the fits, are reported on **Figure II.10 (b)**.
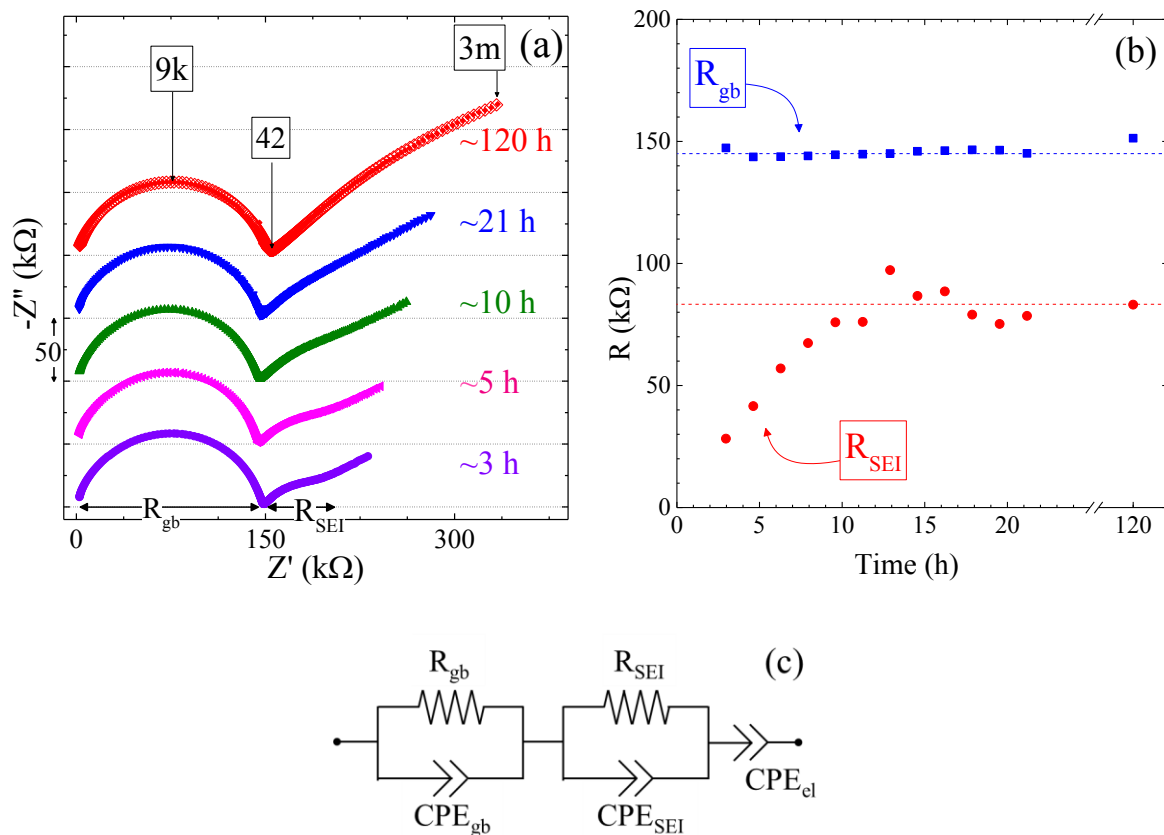
***Figure II.10**. (a) Nyquist plot of the impedance spectra of a Li|LBF|Li cell in open circuit conditions at 30 °C. (b) Evolution of R_{gb} and R_{layer} in function of time under open circuit conditions. (c) Equivalent circuit used to fit the data.*

The appearance of a second semi-circle is attributed to the formation of an interface layer formed upon contacting Li with LBF. This layer can be described as a solid electrolyte interface (SEI). While the values of the electrolyte resistance R_{gb} does not significantly evolve over time, the resistance of the SEI, R_{SEI}, gradually increases until it stabilizes at around 82 kΩ after a 15 h. Thus, the increase of R_{SEI} prior to stabilization can be ascribed to the increase of the thickness of the SEI until it becomes sufficiently thick to impede significant local charge/mass transfer, and reach equilibrium. However, R_{SEI} (≈ 41 kΩ for a single Li|LBF interface) is inferior to the electrolyte resistance R_{gb} (≈ 145 kΩ) so that the overall cell impedance remains sufficiently low to conduct electrochemical characterizations. All these observations suggest that Li is a suitable electrode for the measurement of the electrochemical stability of fluoride solid electrolytes.

To evaluate the experimental electrochemical stability of LBF, a Li|LBF|Pt cell was assembled and cyclic voltammetry was performed at 0.1 mV/s scan rate, at 30 °C (**Figure II.11**).The cell was polarized up to 7 V and down to -0.5 V, for two cycles. Two main features can be observed. One is the occurrence of redox peaks at around 0 V. The other is the oxidation current observed beyond 5 V.

The redox peaks observed around 0 V are typically observed with Li^+ conducting electrolytes in similar cells (Li|Li-electrolyte|Pt) and are attributed to the lithium plating and stripping (reduction and oxidation) at the working electrode[61], [72]–[75]. Considering the structure of LBF, it is unlikely that Li^+ can migrate through the electrolyte from the Li electrode to the Pt electrode. Therefore, these redox peaks can be assigned to redox reactions involving LiF/Li at the Li electrode and LaF_3/La (and BaF_2/Ba) at the Pt electrode. For instance, the reaction

$$LaF_3 + 3\ Li \rightarrow 3\ LiF + La \qquad\qquad 47.$$

gives a $\Delta E° \approx 0.35$ V.
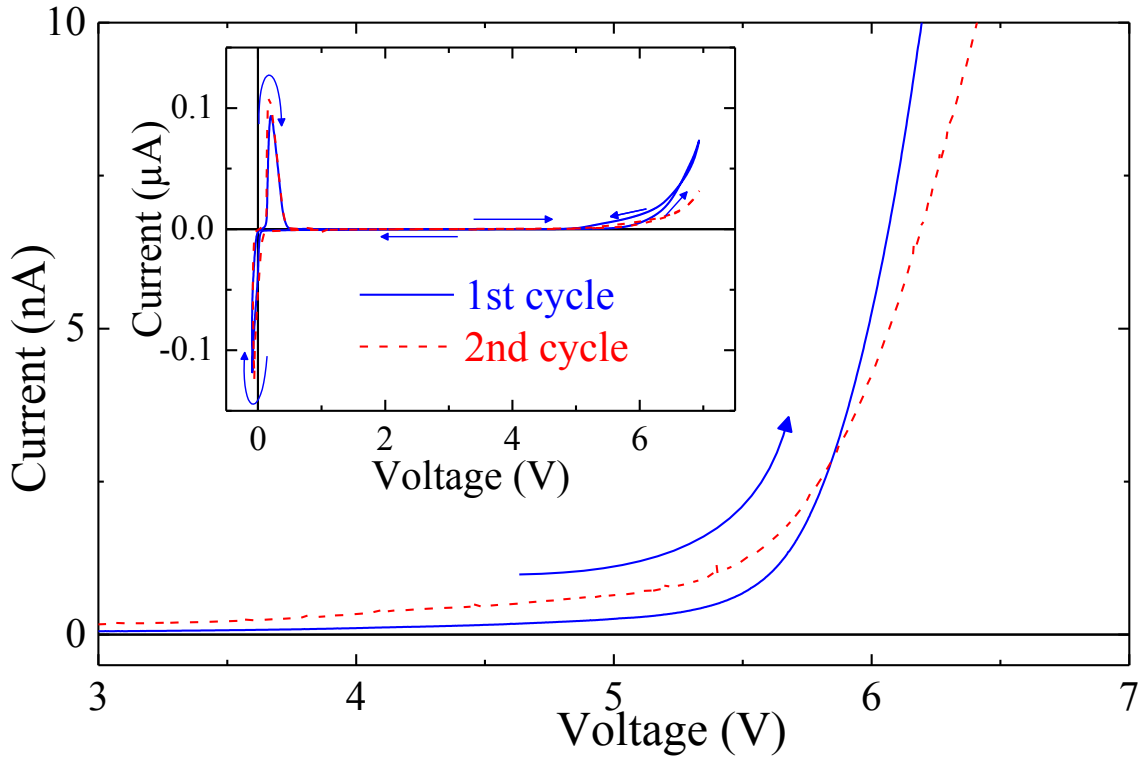
Figure II.11. *iR drop corrected cyclic voltammograms (2 cycles) of the Li|LBF|Pt cell performed at a 0.1 mV/s scan rate, at 30 °C. The figure focuses on the decomposition characterized by a steep increase of the current at around 5.7 V during the forward scan. In inset is the full scan between 7 V and -0.2 V. Measured OCV prior CV was 1.1 V.*

The oxidation current observed beyond 5 V is characterized by a steep increase at around 5.7 V which can be ascribed to the electrochemical decomposition of LBF. The latter can be calculated from thermodynamic properties by considering the following general decomposition reaction:

$$MF_{x\,(s)} \rightarrow M_{(s)} + \frac{x}{2}\,F_{2\,(g)} \tag{48.}$$

The theoretical potential of such reaction is given by:

$$\Delta_r G° = -nF\Delta E° = \Delta_f H° - T\Delta S° \tag{49.}$$

with n the number of moles of electrons exchanged upon decomposition, F the Faraday constant (96485 C.mol^{-1}), T the absolute temperature, and $\Delta_f H°$ and $\Delta S°$ are respectively the standard enthalpy and entropy of the reaction.

Calculations based on equation $48\Delta_r G° = -nF\Delta E° = \Delta_f H° - T\Delta S°$ 49 yields a $\Delta E°$ of 5.73 V for LaF$_3$ (and 6.00 V for BaF$_2$), which is in good agreement with the value of 5.811 V calculated by Roos and Schoonman.[37]

The calculated decomposition potential of LaF$_3$ is in good agreement with our experimental observations, although it seems that the current increases before the value of 5.7 V. This could be due to kinetic effects related to the nanocrystalline nature of the electrolyte.[76] The less steep increase of the decomposition current in the 2nd cycle could to be due to passivation of the Pt working electrode due to the formation of PtF$_x$ at about 4 V. The calculated thermodynamic potential of fluorination of Pt and defluorination of LiF or LaF$_3$ is located between 3.89 and 4.53 V [77].

By polarization a Li|LBF|Pt cell at potential of approximately 5.7 V, the LBF at the Li electrode should be reduced to La/Ba metal while F$_2$ evolution takes place at the Pt electrode. The mechanism is in good agreement with experiments made by Bezmelnitsyn *et al*.[64] who polarized a M|LBF|M cell (M = Ni, Cu or graphite) by applying a galvanostatic current of 1.0 mA revealing F$_2$ and HF gases evolution and the formation of La/Ba dendrites at the negative electrode. XPS analysis of the dendrites showed that it was a mixture of La and Ba metal with a Ba/La ratio corresponding to that in the LBF. As for F$_2$ evolution, Bezmelnitsyn *et al*.[64] propose a recombination type mechanism between holes h$^+$ and fluoride ions F$^-$ to yield elemental fluoride F^0, which then recombines to form F$_2$.

We can summarize the experimental observations by the schematic illustration of the alleged decomposition mechanism displayed on **Figure II.12**.
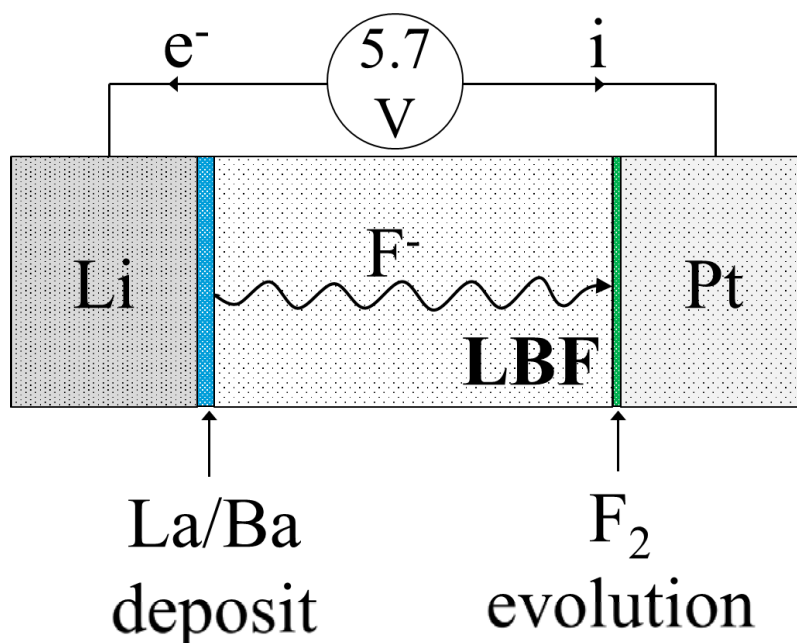
Figure II.12. *Schematic illustration of the decomposition mechanism of LBF.*

In conclusion, we established that lithium is a suitable electrode for the measurement of the electrochemical stability of solid fluoride electrolytes. The SEI formed upon contacting Li with the fluoride solid electrolyte is not entirely blocking, and the presence of the LiF/Li redox couple can be conveniently used to evaluate the electrochemical stability of the solid fluoride electrolyte. Furthermore, this result is very encouraging as it indicates that lithium can be used as a reference electrode for FIBs in a three-electrode setup.

The decomposition potential of LBF starts above 5 V, which is in good agreement with the calculated value of 5.73 V. The suspected mechanism involving reduction of LBF at the cathode and F_2 evolution at the anode is supported by the work of previous authors.

Therefore, FIBs employing nanocrystalline LBF as solid fluoride electrolyte can be operated in a 5 V potential window, safe from the decomposition of LBF.

4.3.3. Chemical and electrochemical compatibility with carbon

Metal fluorides are generally poor electronic conductors due to their large band gap, as predicted by the band theory (e.g 6.043 eV for LaF_3, 6.619 eV for BaF_2)[78]. Their use as active material necessitates the development of composites containing electronic conductive additives

to ensure the electronic percolation in the electrode. This is typically done by mixing carbon black with the active material. Ball-milling is a common method to produce metal fluoride-carbon nanocomposites that present good performance in conventional lithium-ion batteries.[1]

The same approach is generally used to produce electrode composites for solid-state lithium and fluoride-ions batteries. Some metal fluorides that can be used as active material sometimes offer ionic conductivity properties (e.g. BiF_3) but their conductivity remains several orders of magnitude lower than that of LBF. Moreover, upon operation of the FIB, the metal fluoride will lose its ionic conductivity properties when reduced to its metallic state.

In a nutshell, both carbon and electrolyte must be present in the electrode composites to ensure electronic and ionic conductivity upon operation of the FIB. This raises the question of the interaction of carbon additives with the fluoride conducting electrolyte, both upon preparation of the electrode materials and upon operation of the cell.

The carbon chosen to prepare the LBF-C composite is a typical carbon black (Pure Black, Superior Graphite) with particles of about 20 nm in diameter, as determined from TEM investigations. A surface area of 44 m²/g was found from surface area measurements employing N_2 gas and BET theory.

The C (10 wt %) and LBF (90 wt %) powders were first outgassed for 12h at 150 °C under vacuum. The powders were then mixed with an agate mortar and pestle, in a glovebox. Finally, the black powder was ball-milled under Ar in conditions similar to LBF preparation. The X-ray diffraction diagrams of the LBF, carbon and LBF-C composite are presented on **Figure II.13**.
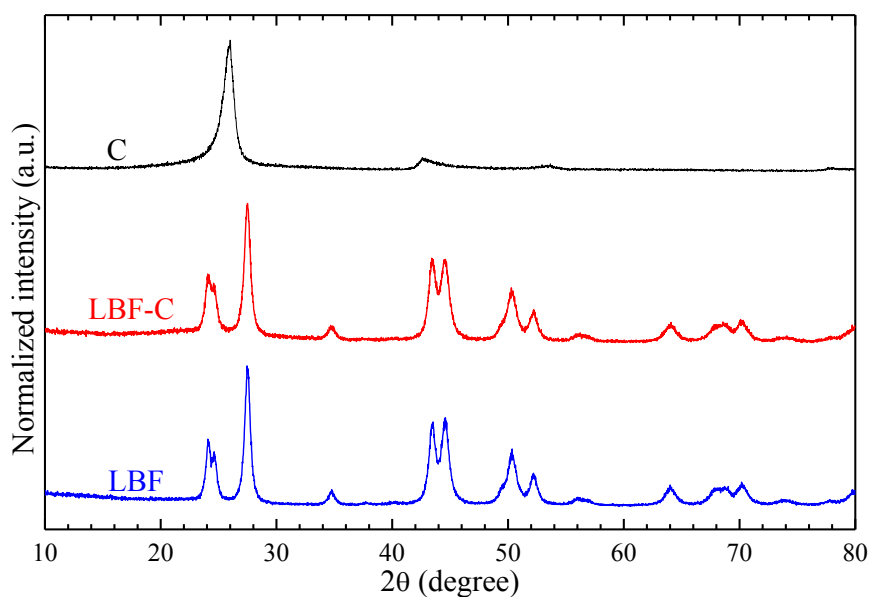
Figure II.13. *Normalized X-ray powder diffraction diagrams of carbon black C, LBF and LBF-C (90:10 wt %) composite ball-milled for 4 hours.*

The result shows that the structure of LBF remains intact. Although a slight amorphisation of LBF seems to occur as the particle size estimated from the (111) peak shifted from 13 nm for the pristine LBF to 12 nm in the LBF-C composite. The carbon however seems to be significantly amorphised, perhaps due to the ball-milling process, as peaks present in the pristine carbon black, which correspond to graphite-3R, are not visible in the LBF-C composite.

Figure II.14 shows TEM images of the ball-milled LBF-C composite. Agglomerates of LBF of size ranging from a few dozen to several hundred nanometers are typically observed. LBF agglomerates are surrounded by the matrix constituted of carbon black, which still exhibits a few graphitic zones.
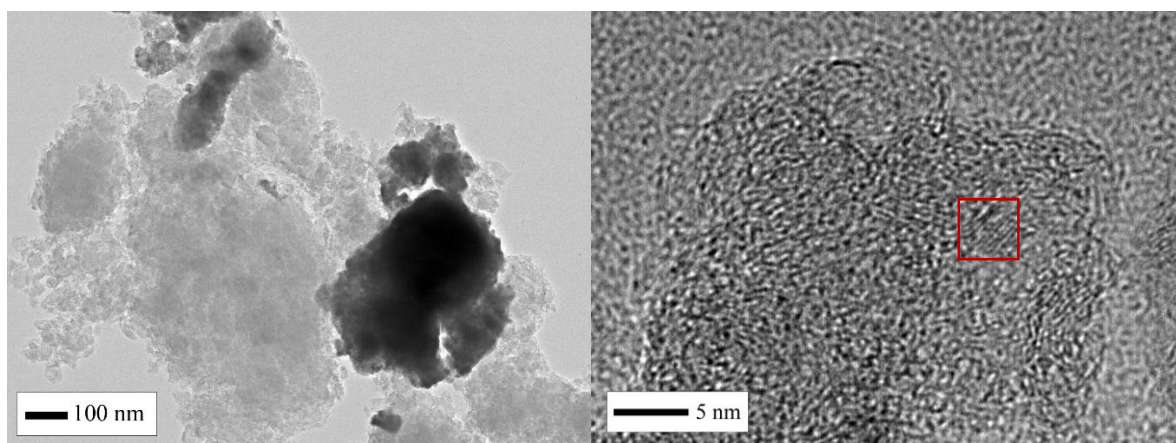
Figure II.14. *Transmission electron microscopy images obtained on the ball-milled LBF-C composite (left) and zoom in on one of the carbon agglomerates present in the LBF-C composite (right). The red square shows a typical graphitic zone presenting a d spacing of 0.33 nm, typical of the (003) plane of graphite (R-3mR) exhibiting a d spacing of 3.35 Å.*

EDX experiments performed on a carbon black zone (not shown) indicate that small amounts of La could be detected, suggesting the presence of small particles of LBF. They could not be observed by high-resolution, due to either their very small size or their amorphous nature.

4.3.3.1. Electrical characterization of the LBF-C composite

The electrochemical properties of the LBF-C composite was first investigated by EIS performed on a graphite|LBF-C|graphite cell denoted Cg|LBF-C|Cg thereafter. A Cg|Cg cell was used as a reference. **Figure II.15** shows the impedance spectra of the Cg|LBF-C|Cg and Cg|Cg cells recorded at 30 °C. The presented impedance spectra are characteristic of electronic conductors (single resistor), but present an inductive contribution, which is probably due to the wiring of the measurement setup. The Nyquist plot of a resistor ($Z_R = R$) is characterized by a single value on the x axis yielding the resistance.
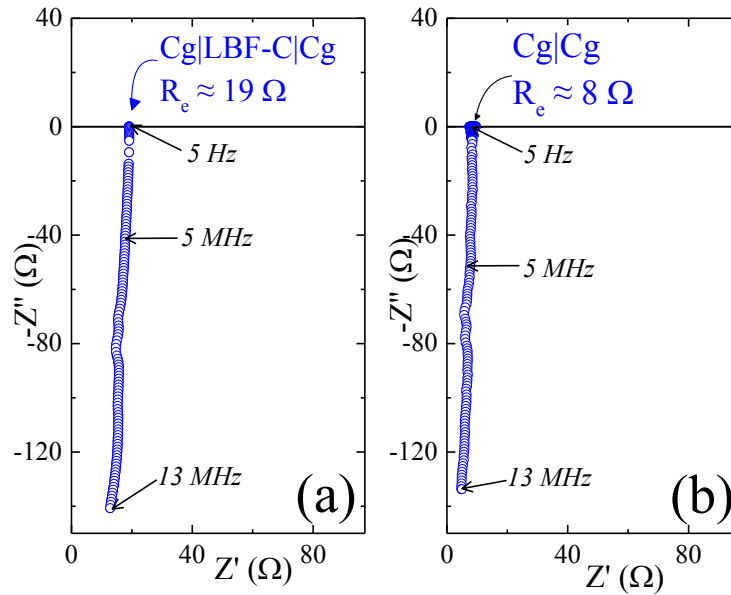
Figure II.15. *Impedance spectra of a Cg|LBF-C|Cg (a) and Cg|Cg (b) cell at 30 °C (Cg = carbon graphite discs).*

The intersection of the inductive tail with the x axis $(-Z'' = 0)$ indicates the electronic resistance R_e of the cells yielding 19 Ω and 8 Ω, for Cg|LBF-C|Cg and Cg|Cg, respectively. An electronic resistance of 11 Ω for the LBF-C composite was deduced, yielding an electronic conductivity of $\sigma_e \approx 10^{-2}$ S.cm^{-1} suggesting that the electronic percolation threshold is reached for 10 wt % C. Moreover, the electronic conductivity of LBF-C is several orders of magnitude higher than the ionic conductivity in pure LBF (almost 5 orders of magnitude at 30 °C), indicating that the electronic conductivity of the electrode it is not the rate limiting phenomena.

The addition of electrolyte to the electrode composite material is essential to ensure ionic conductivity. Nevertheless, the determination of the ionic conductivity in electrode material is particularly challenging as electrical properties are dominated by carbon additives. Thus, the determination of the ionic conductivity of the LBF-C composite in the Cg|LBF-C|Cg setup is not possible due to the short-circuit/shunt created by the carbon. To counter this, we used a setup suggested by Professor Dollé from the University of Montreal. The cell configurations used for the determination of σ_i(LBF-C) is presented in **Figure II.16**. It is possible to obtain the ionic contribution of the LBF-C composite by using LBF as electronically blocking electrodes. The electrons are blocked at the LBF|LBF-C interface so that the electronic conductivity of LBF-C does not short circuit the cell. Consequently, the ionic conductivity of both LBF and LBF-C can be determined.
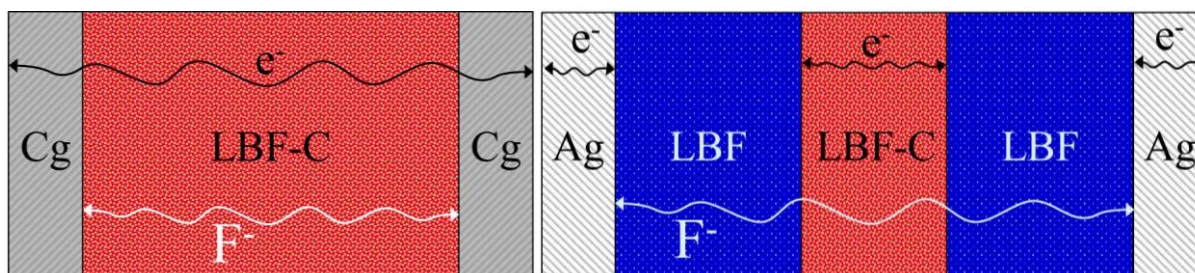
Figure II.16. *Schematic representation of the Cg|LBF-C|Cg and Ag|LBF|LBF-C|LBF|Ag cells used to determine the electronic and ionic conductivity of LBF-C, respectively. Schematic electronic (e⁻) and ionic (F⁻) diffusion routes or blocking effects are shown for the sake of clarity.*

Figure II.17 shows the impedance spectra of the Ag|LBF|LBF-C|LBF|Ag cell recorded at 30 °C. The spectra of the Ag|LBF|Ag recorded at the same temperature is added for comparison purposes. The frequency shift observed for the stack configuration when compared to the sole LBF might be due to the slower migration of F⁻ in the LBF-C layer, thus increasing the characteristic time of the process, thus decreasing the characteristic frequency.
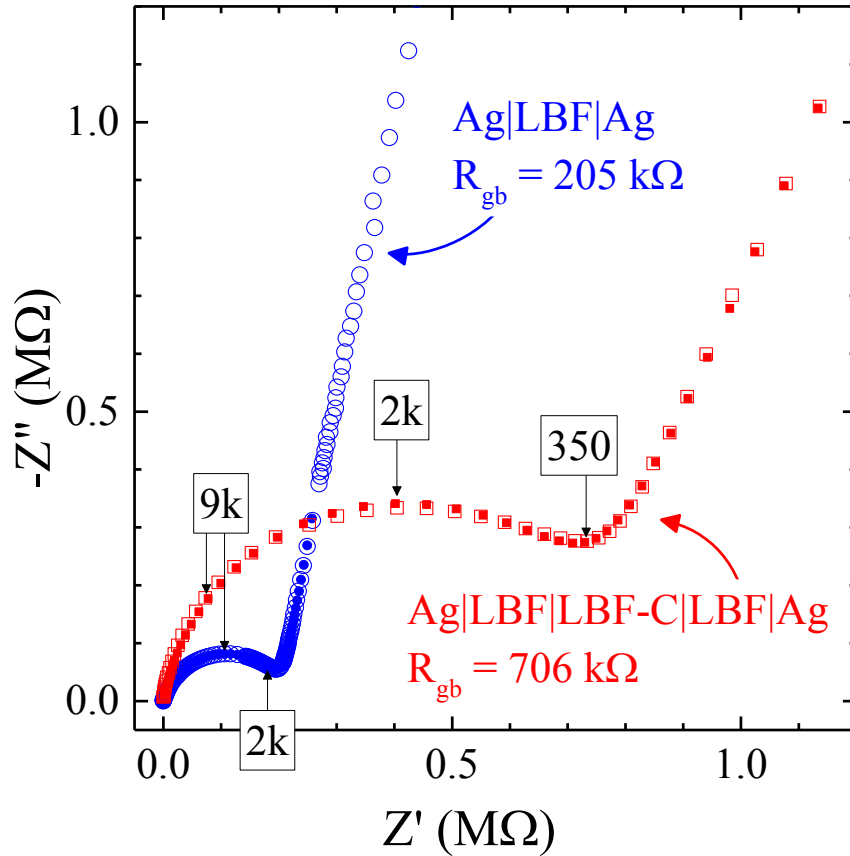
Figure II.17. *(a) Nyquist plot of the impedance spectra of an Ag|LBF|LBF-C|LBF|Ag cell recorded at 30 °C. The results of the Ag|LBF|Ag are shown for comparison purposes. The open symbols represent the data and the closed symbols represent the fit obtained.*

The ionic conductivity of the LBF-C layer can be determined by subtracting the contribution of the LBF layers. It should be noted that using this method, the ionic conductivity of LBF-C might be overestimated as the LBF-C layer may overlap the sides of the LBF pellets having for effect of increasing the contact area at the LBF|LBF-C interfaces, thus increasing the calculated ionic conductivity of the LBF-C composite. The resistance of the LBF-C layer corresponds to the resistance of the Ag|LBF|LBF-C|LBF|Ag stack (706 kΩ) minus the resistance of the two LBF layers (2×205 kΩ). A resistance of 296 kΩ was deduced for the LBF-C layer yielding an ionic conductivity of 5×10^{-8} S.cm^{-1} at 30 °C. This value is about one order of magnitude lower than the ionic conductivity of LBF alone (5.4×10^{-7} S/cm) showing that the ionic percolation is maintained within the LBF-C composite. Moreover, its shows that the interactions with carbon impacts on the ionic transport properties of the electrolyte. This point should be investigated in more details using, for instance, dielectric spectroscopy[79].

In summary, the investigation of the electrical properties of the LBF-C material revealed that both electronic ($\sigma_e \approx 10^{-2}$ S.cm^{-1}) and ionic percolations ($\sigma_i \approx 5\times10^{-8}$ S.cm^{-1}) are insured within the composite. The methodology adopted here provides a versatile tool to optimize the composite electrode by obtaining the best compromise between electronic and ionic conductivity.

4.3.3.2. Electrochemical interaction with carbon

While in lithium batteries, it is well established that carbon additives poorly contribute to the overall capacity, the possible electrochemical fluorination of carbon in FIBs is still an open question. This is particularly relevant since the fluorination of carbon can yield CF$_x$ compounds which are electronic insulators thus preventing the electrochemical reactions to occur. To investigate potential reactions with carbon, the electrochemical reactions occurring in Li|LBF|C and Li|LBF|LBF-C cells were compared with a reference cell with no carbon, *i.e.* Li|LBF|Pt cell. The cells were polarized from the OCV (~3V) to 7V. The complete CV scans on Li|LBF|LBF-C and Li|LBF|C cells can be found in supporting information (**Figure II.20** and **Figure II.21**, respectively). **Figure II.18** shows the 1st cycle forward scans (fresh cell) from 3 V up to 7 V and their corresponding derived curves for Li|LBF|Pt, Li|LBF|C and Li|LBF|LBF-C cells. The comparison is made using the current density i = I/A (A/cm²).

Upon polarization, fluoride ions are moving from the Li cathode towards the Pt or carbon-based working electrode anode **(Inset Figure II.18)**. To ease the discussion, the cells will be referred by the name of their respective working electrode (*i.e.* Pt cell, C cell and LBF-C cell).
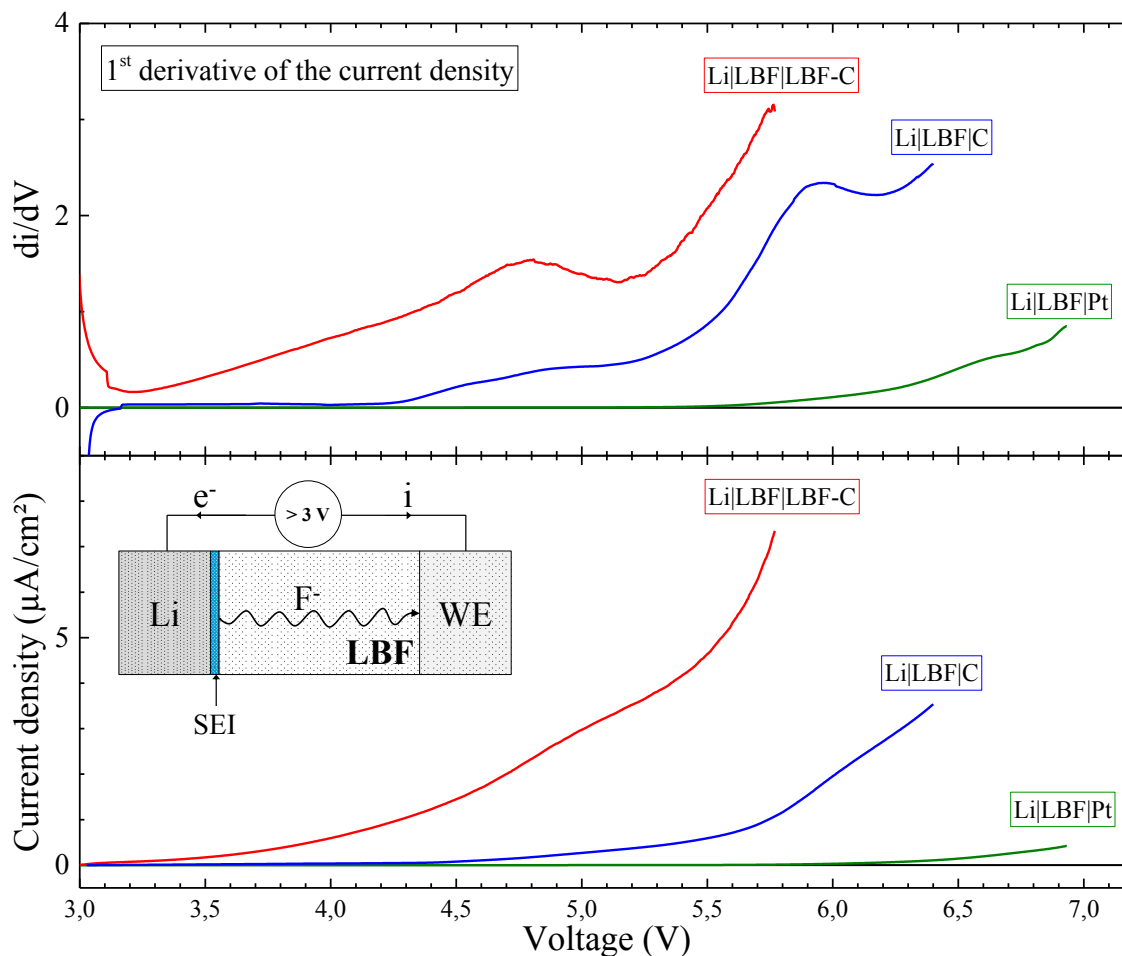
Figure II.18. *Overlaid forward CV scans for the 3 Li based cells with different working electrodes:* ▲ *Pt,* ■ *C and* ● *LBF-C. The curves were corrected for iR drop and normalized with the current density. A schematic representation of the polarized cell illustrating the migration of fluoride ions towards the working electrode is shown in inset. The smoothed 1ˢᵗ derivative of each curve is shown above.*

The voltammogram of the reference cell (Pt) shows a current increase within the electrolyte decomposition region. The derived curve indicates that the decomposition starts at about 5.5 V, which is in good agreement with the calculated value of 5.73 V for LaF_3. It should be noted that the formation of PtF_x cannot be observed in this condition because of a poor contact between LBF and Pt.

In the presence of carbon, i.e. LBF-C and C cells, the current rises before that of the Pt cell, and at potentials below the expected decomposition of LaF_3 (5.73 V). The derivatives feature two main contributions located at 4.2-4.8 V, and beyond 5.2 V. The later can be assigned to the electrochemical decomposition of the electrolyte. The early onset of the decomposition of LBF

might be due to the increased contact area between the solid electrolyte and the carbon that accelerates the kinetic of the reaction.[80]

Since the current observed between 4.2 and 4.8 V involved LBF and carbon, the electrochemical fluorination of carbon was considered. The occurrence of such a reaction was verified by calculation of standard potentials of the reaction of carbon with LiF and LaF$_3$ to yield (CF)$_n$. Both reactions are considered since LiF/Li and LaF$_3$/La could be present at the Li|LBF interface due to the formation of the SEI. The standard potential of the electrochemical fluorination reaction of carbon was calculated using the enthalpy of formation of CF$_x$. According to Valerga et al.[5], the entropy and enthalpy of formation of CF$_x$ depends on the F/C ratio (denoted x, thereafter) and can be calculated (at 298 K) as follows:

$$\Delta_f H^0_{CF_x} = (4.53 - 178.01\, x)\, kJ.mol^{-1}$$ 50.

$$S^0_{CF_x} = (4.62 - 16.91\, x)\, J.K^{-1}.mol^{-1}$$ 51.

Figure II.19 shows the calculated standard potentials of the reaction of carbon with LiF and LaF$_3$ to yield (CF)$_n$, with different degree of fluorination.
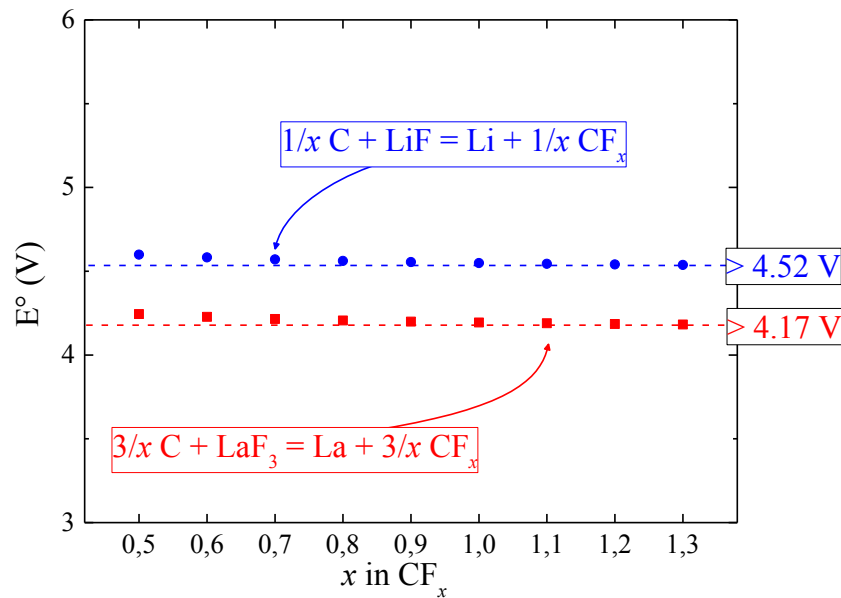
Figure II.19. *Calculated standard potentials of the formation of CF$_x$ against LiF and LaF$_3$ with increasing x value. Thermodynamic data of CF$_x$ were taken from Valerga et al.[5]*

The calculated average potentials yield 4.17 and 4.52 V for reactions involving LaF$_3$ and LiF, respectively. These values correspond to those found experimentally demonstrating that carbon can undergo electrochemical fluorination reactions.

For the C electrode, the derivative shows that a significant increase of the current is observed at about 4.3 V, which is concomitant with the calculated potential for the reaction of LaF_3 to form $(CF)_n$ at the LBF|C interface (4.17 V). The current further increases, characterized by a small bump on the derivative, at about 4.6 V, which might be related to the fluorination reaction but involving LiF (4.52 V). Finally, a frank change of slope is observed above 5.5 V, which corresponds to the decomposition of LaF_3 (5.73 V) yielding elemental fluorine.

Because CF_x exhibit insulative properties due to the covalent nature of the C-F bond inducing a sp^3 hybridization in these compounds[81], the progressive fluorination of the carbon will eventually lead to a progressive loss of the operational electronic conduction pathways. On one hand, it shows that the electrochemical window needs to be narrower to avoid the formation of carbon fluorides. On the other hand, the use of C/CF_x can be considered as an effective active materials as suggested by Potanin.[82]

4.4. Conclusion

In conclusion, the electrochemical stability and electrical properties of nanocrystalline fluoride solid electrolyte $La_{0.95}Ba_{0.05}F_{2.95}$, LBF, were investigated both in its pure and composite form with carbon. Electrochemical characterizations have been performed using a lithium electrode which has been shown to be a versatile CE. It has been shown that upon contact with the solid fluoride electrolyte, a solid electrolyte interface (SEI) made of LiF is formed, providing the Li^+/Li redox couple. This method has allowed to establish the decomposition potential of LBF at 5.4-5.7 V in good agreement with the calculated value.

Subsequently, the electrical properties of the composite LBF-carbon was investigated using a conventional set up. It showed that only the electronic conductivity could be assessed, revealing that 10 wt % of carbon is sufficient to enable electronic percolation. The determination of the ionic conductivity within the composite was probed by a novel set up consisting of LBF|LBF-C|LBF stacks. The results showed that the ionic percolation is maintained within the LBF-C composite and that the interactions with carbon impacts on the ionic transport properties of the electrolyte.

Finally, we demonstrated that carbon underwent electrochemical fluorination reactions which have to be taken into account when setting the operating window of FIBs. While the fluorination of carbon to yield insulative carbon fluoride could be a serious limitation to the operation of

FIBs, notably in terms of operating potential, it also opens new opportunities to develop high-energy FIBs as the fluorination of lightweight carbon might be reversible in such systems.

4.5. Supporting information
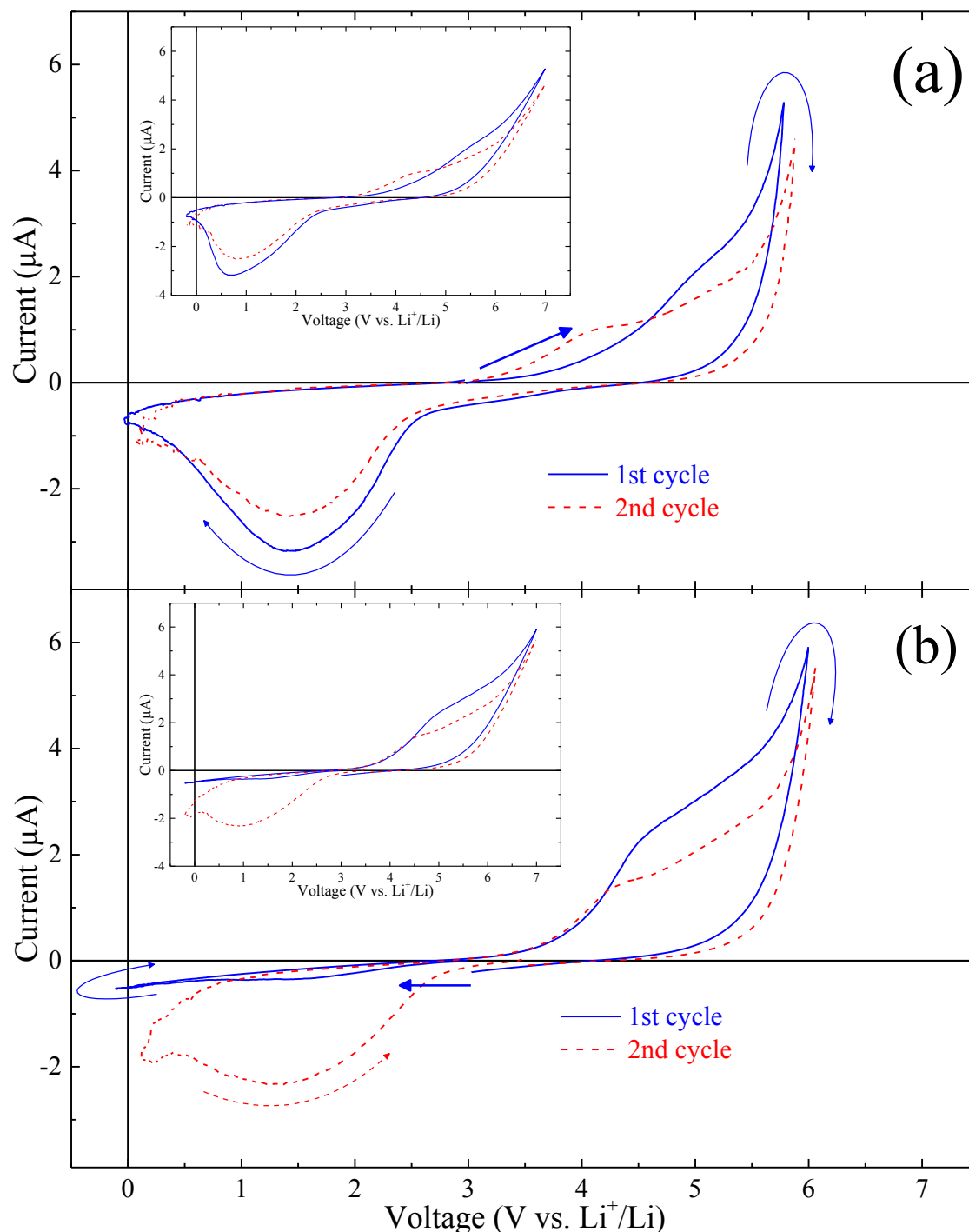
Figure II.20. *iR corrected voltammograms of the Li|LBF|LBF-C cells cycled from OCV up to 7 V then down to - 0.2 V (a) and down to -0.2 V then up to 7 V (b), at a 0.1 mV/s sweep rate at 30 °C. The electrolyte resistance determined from impedance diagrams was used to correct the iR drop. The corresponding non corrected voltammograms are in inset.*
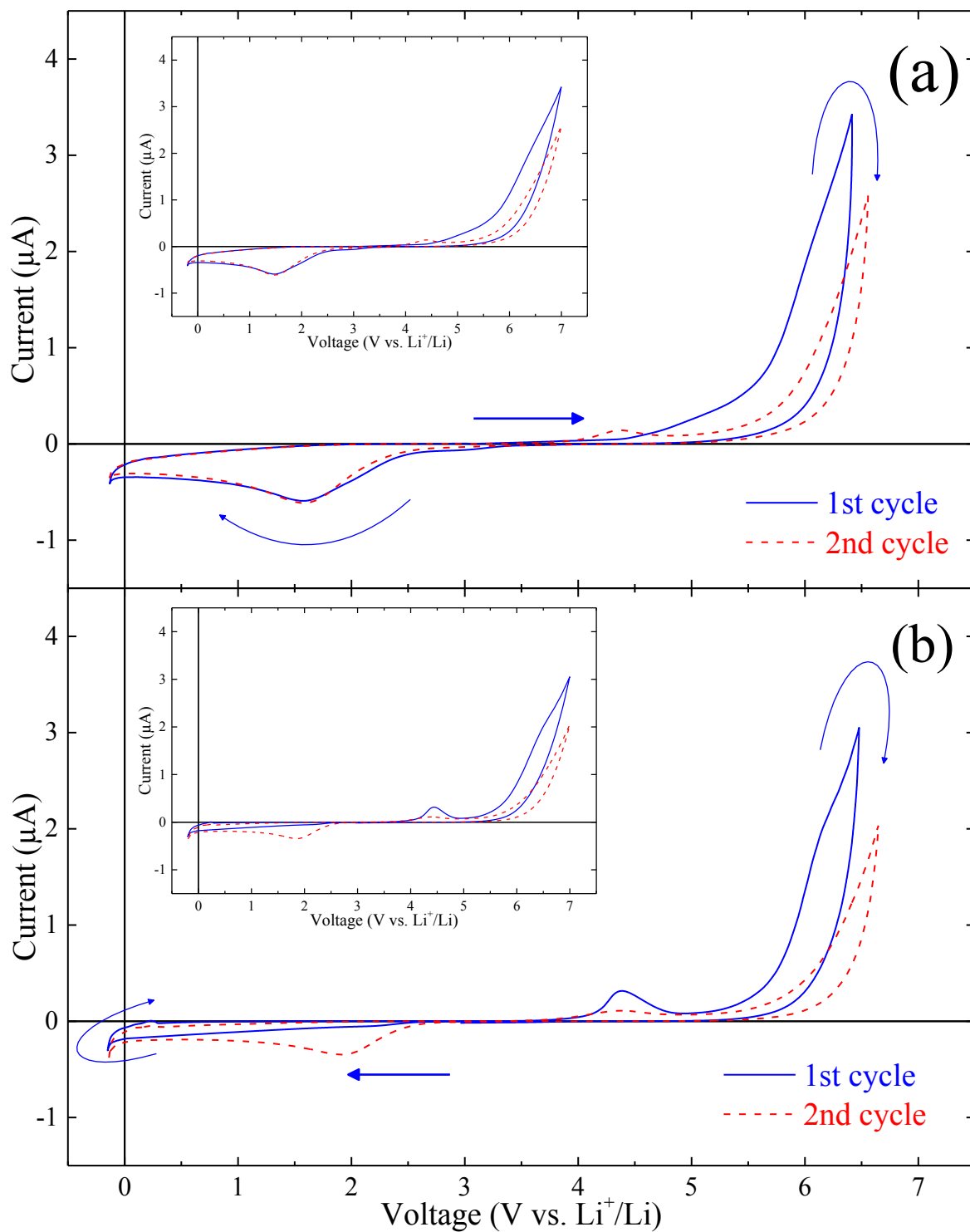
Figure II.21. *iR corrected voltammograms of the Li|LBF|C cells cycled from OCV up to 7 V then down to - 0.2 V (a) and down to -0.2 V then up to 7 V (b), at a 0.1 mV/s sweep rate at 30 °C. The electrolyte resistance determined from impedance diagrams was used to correct the iR drop. The corresponding non corrected voltammograms are in inset.*

Chapter III. Modified coin-cell setup for solid-state fluoride-ion batteries

1. Introduction

In the field of batteries, it can be particularly interesting to perform electrochemical investigations at high-temperature. This is the case for solid-state fluoride-ion batteries where, at room temperature, the resistance of the solid electrolyte is the main contribution to the cell internal resistance. Operating the cell at increased temperatures reduces the internal resistance. Therefore, it allows using higher currents, and thus obtaining faster charge-discharge cycles.

Typical testing systems for batteries rely on coin-cell or Swagelok-type systems. Other commercial systems are available but rely on plastic seals which are not adapted for high-temperature studies.

For instance, coin-cells employ polyethylene (PE) or polypropylene (PP) sealing O-rings that soften and age quickly at increased temperatures, leading to the loss of sealing properties.

Similar observations can be made with Swagelok-type cells. The sealing of Swagelok cells is generally ensured by polytetrafluoroethylene (PTFE) rings. While PTFE presents a high fusion temperature ($T_f > 300$ °C), it is also subject to softening and to significant creeping. The creeping can eventually lead to a loss of the sealing properties of the Swagelok. Early experiments carried out with a conventional Swagelok-type cell placed in an oven at 150 °C confirmed that the sealing properties were lost after a few days. Moreover, the PTFE sealing rings were permanently damaged as they were significantly deformed due to the creeping of PTFE at this temperature. The development of hermetical Swagelok-type cells requires significant modifications[83].

One alternative to the issue of hermetical sealing is the operation of the cell in inert atmosphere. Operating cells at high temperature in a glovebox is constraining and must be carried out with caution as hot metal parts can permanently damage the glovebox. Therefore, it is desirable to develop hermetical high-temperature electrochemical cells and setups that can be easily and rapidly prepared.

Here, we report a simple method to prepare modified coin-cells that allows operating the cells at 150 °C. Sealing is achieved by applying a high-temperature epoxy resin on the outside surface of the cell. The cells are then placed on a custom made test bench for electrochemical

investigations. A symmetrical cell relying on the BiF_3/Bi redox couple was used to confirm that the modified coin-cell remained air-tight for several weeks.

2. Experimental

Unless specified otherwise, all the manipulation of the materials and assembly of the cells were carried out in a dry Ar glove box (H_2O < 2 ppm).

2.1. Materials preparation

All powdered materials were outgassed for 12 hours at 150 °C under vacuum, then placed in the glovebox without any contact with air.

$La_{0.95}Ba_{0.05}F_{2.95}$ (LBF) electrolyte was prepared by ball-milling stoichiometric amounts of LaF_3 (Alfa Aesar, 99.99 %) and BaF_2 (Strem chemicals, 99.99 +%) in Ar atmosphere (Johann Chable and Ana Gil Martin, IMMM, Le Mans). A Fritsch mini pulverisette 7 premium line planetary mill with ZrO_2 grinding bowls and 10 ZrO_2 grinding balls (10 mm diameter) was used. To produce 4 g of LBF, the mixture was ball-milled for a total of 12 hours (48 cycles of 15 min with 15 min pauses) at a rotational speed of 400 rpm.

To prepare the $Bi-BiF_3$-LBF-C composite electrode, β-BiF_3 (Alfa Aesar, 99.999%) and Bi (Alfa Aesar, -200 mesh, 99.999%) commercial powders were mixed with LBF and carbon black in 15:15:60:10 % wt ratio. The mixture was hand-milled for about 30 minutes in the glove box with an agate mortar and pestle.

2.2. Characterization by X-ray diffraction

The $Bi-BiF_3$-LBF-C composite electrode was characterized by X-ray synchrotron diffraction to obtain better 2θ resolution. The powder was sealed in Kapton capillaries (Cole-Parmer®, polyimide tubing, 0.0435" outside diameter, 0.0020" wall) under argon atmosphere, using epoxy resin. Hard X-rays were collected at the 11-ID-B beamline of the Advanced Photon Source of Argonne National Laboratory, USA. Total scattering data were recorded at 58.66 keV ($\lambda_1 = 0.21140$ Å), using a 2D amorphous silicon-based area detector (PerkinElmer). Total scattering data I(Q) were obtained by using the FIT2D software. Conversion of the scattering data I(Q) to classical CuKα ($\lambda_2 = 1.5418$ Å) XRD data I(2θ) was done using the relation:

$$Q = \frac{4\pi \sin \theta}{\lambda_2} \qquad \rightarrow \qquad 2\theta = 2 \arcsin \frac{Q\lambda_2}{4\pi} \qquad\qquad 52.$$

2.3. Cell assembly

Symmetrical cells were assembled using approximately 16 mg of the Bi-BiF$_3$ composite, and 200 mg of LBF. The powdered stack was pressed in a ⌀10 mm stainless steel die with an uniaxial press (Specac Atlas), at a load of 5 tons. Two graphite disks (C$_g$) were pressed with the powdered stack to form a C$_g$|Bi-BiF$_3$-LBF-C|LBF|Bi-BiF$_3$-LBF-C|C$_g$ cell in a single step. The graphite disks were directly pressed with the powders to provide a good contact between the composite and the current collector and to ensure the easy handling of the pellet stack.

Graphite disks (Cg) were cut from high purity graphite rods (Mersen). Graphite rods were previously machined to reduce their diameter so that they would fit the pressing mold. The discs were then polished with grit P400 SiC abrasive paper, degreased in acetone then sonicated three times in ultra-pure water for *ca.* three minutes. Finally, Cg disks were outgassed at 150 °C for 12 h under vacuum, and entered in the glovebox without any contact with air. Typical thickness of the graphite discs was 0.5 – 0.7 mm.

Finally, the C$_g$|Bi-BiF$_3$-LBF-C|LBF|Bi-BiF$_3$-LBF-C|C$_g$ stack was placed in a modified coin-cell as described in the discussion.

Flat PTFE washers (⌀$_{ext}$ 16.0 mm, ⌀$_{int}$ 9.95 mm, 1.5 mm thickness) were machined from a PTFE rod. For the electrochemical investigation, one flat wave spring and one spacer were used to maintain electrical contact within the coin-cell.

2.4. Electrochemical measurements

Electrochemical measurements were performed with an AMETEK PARSTAT PMC 500 potentiostat connected to the cell in a two electrode setup, i.e. the reference and counter electrodes were plugged together. The cells were placed in the oven at 150 °C on the custom-made electrochemical test bench described in the discussion.

Galvanostatic (I = 3.5 µA) charge-discharge experiments were carried out between 1 V and -1 V. For impedance measurements, the cells were left to rest for 2 hours prior to recording. The spectra were recorded between 300 kHz and 10 mHz with a sinusoidal excitation amplitude of 30 mV.

3. Results and discussion

3.1. Cell development

The modification of coin-cells provides a simple and rapid way to obtain electrochemical cells that can achieve high-temperature (150 °C) hermetical sealing. Airtightness may be achieved by using high-temperature resistant epoxy resin. CR2032 coin-cells were chosen as starting setup.

A schematic representation of the modified CR2032 coin-cell is presented on **Figure III.1**. The original CR2032 coin-cell cases and parts were all purchased from MTI-corp. All parts are made from 304 stainless steel. The case sealing O-ring is made of PP, and is already mounted on the negative side of the case.
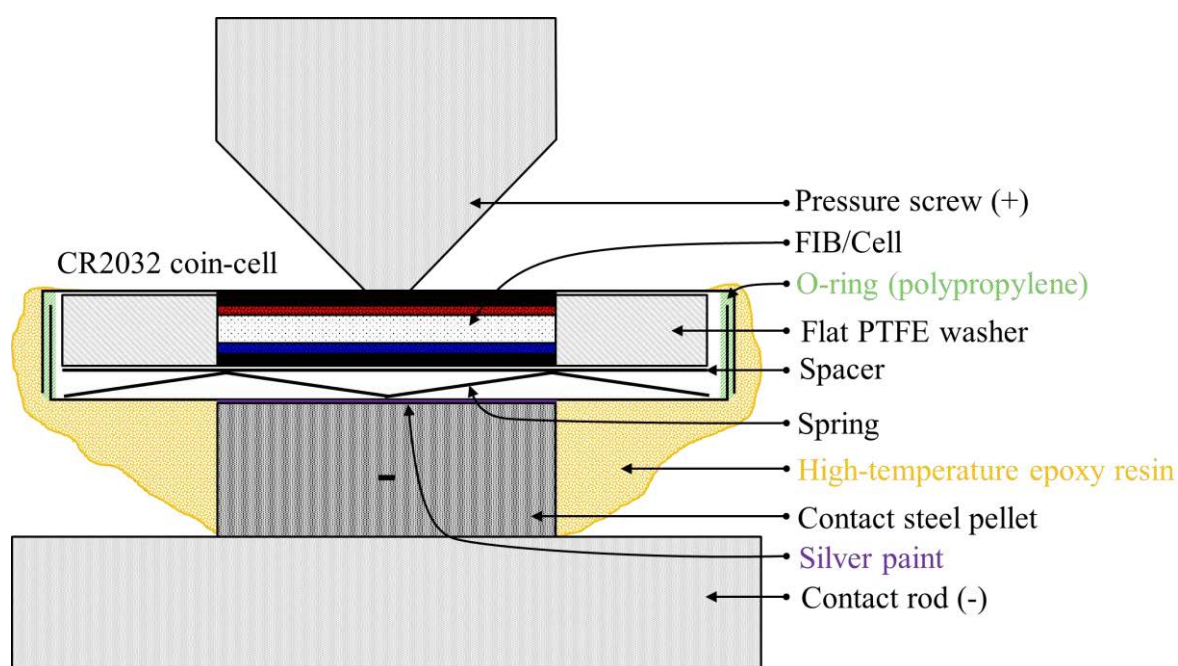
Figure III.1. *Schematic representation of the cross-section of the modified coin-cell placed on the test bench.*

The FIBs/electrochemical cells preparation is described in the experimental section. Some modifications are necessary to adapt the CR2032 coin-cell dimensions ($\varnothing_{int}$ 16.4 mm, 2.8 mm thickness when crimped empty) to the cell dimensions ($\varnothing_{int}$ 10 mm, ~1.5 mm thickness with the graphite disks).

Electrical contact is ensured by a flat wave spring (⌀14.4 mm, 1.5 mm thickness when fully expanded). The number of spacers (⌀15.4 mm, 0.5 mm thickness) is adjusted in function of the thickness of the cell.

A PTFE washer is used to maintain the FIB at the center of the coin-cell.

The crimped coin-cells can then be taken out of the glovebox in order to apply the high-temperature epoxy resin. A steel pellet, used as support and for electrical contact, is attached to the negative side of the coin-cell case. Both the coin-cell and the contact steel pellet are thoroughly degreased with acetone prior to resin application. Additionally, the positive side of the coin-cell is masked with tape which is removed once the resin is cured. The epoxy resin (Loctite EA 9492) used to reinforce the sealing of the coin-cell was selected for its room temperature curing. The technical data sheet indicates that the resin cured at 22 °C offers a lap shear strength with stainless steel of 12 N/mm², and no degradation of the strength retention after 3000 h at 150 °C.

After application, the resin is left to cure for 24 hours, and the tape covering the positive side is removed. A photograph of the modified coin-cells obtained after curing of the epoxy resin is shown **Figure III.2**.
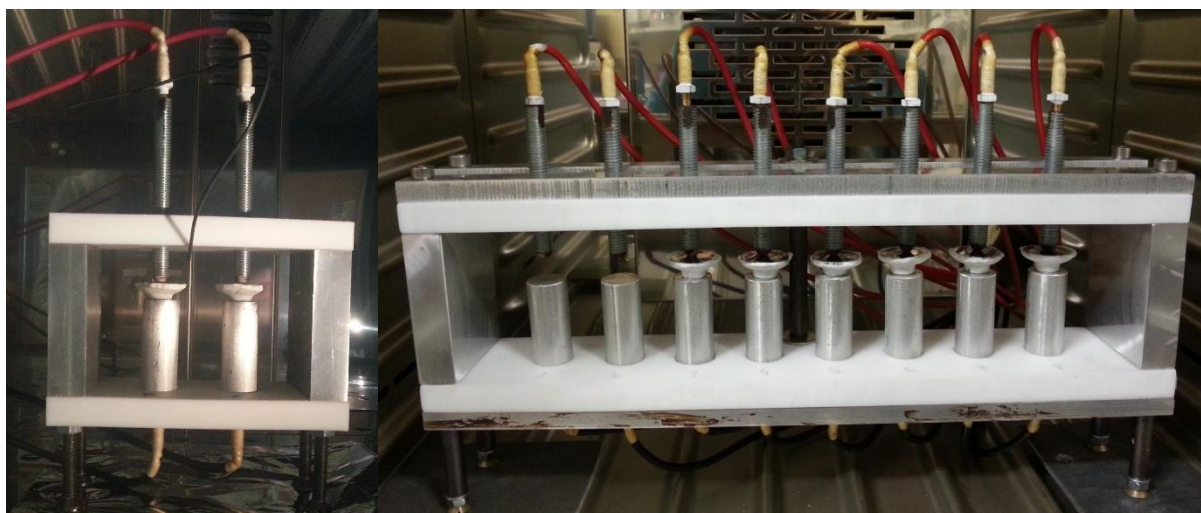

Figure III.2. Photograph of the modified coin-cells.

The as-prepared modified coin-cells can then be placed on the custom made electrochemical test bench for high-temperature testing.

3.2. Electrochemical test bench

The electrochemical test bench needs to be able to withstand continuous operation at 150 °C. Two test benches were built from a metallic structure holding two insulating parallel plates together. The coin cells are tightened between the plates thanks to aluminum contact rods and stainless steel pressure screws (**Figure III.3** and **Figure III.1**). The two insulating plates are composed of PTFE. Considering the low stiffness of PTFE, the 8 ways test bench is reinforced by two steel bars that avoid the bending of the PTFE plates when pressure is applied to the coin-cell by adjusting the screws. The benches are placed in ovens equipped with entry ports, and are connected to the electrochemical measurement apparatus thanks to custom made temperature-resistant silicone-sheath wires and gold plated banana plugs.

Figure III.3. *Photos of the two test benches built to evaluate the electrochemical properties of FIBs and their components.*

The wires are connected to a potentiostat placed next to the oven. The pressure screw maintains the modified coin-cell in place and keeps a constant pressure on the cell placed within the coin-cell to maintain electrical contact.

To confirm the proper sealing provided by the epoxy resin, two symmetrical cells employing the Bi-BiF$_3$-LBF-C composite as electrodes were tested by galvanostatic experiments.

3.3. Structural and electrochemical characterization of the composite

The electrolyte used for our electrochemical investigation is Ba-doped LaF$_3$, which was successfully used in FIBs.[14], [29] Ball-milling LaF$_3$ and BaF$_2$ is an easy method to produce

$La_{1-x}Ba_xF_{3-x}$ (LBF) solid solutions of tysonite-type structure (trigonal, P-3c1) which offer a fluoride-ion conductivity of 9.4×10^{-5} S.cm^{-1} at 150 °C.[34]

We used LBF (60 wt %) and carbon black (10 wt %) with a mixture of Bi and BiF$_3$ (15 - 15 wt %) to produce the Bi-BiF$_3$-LBF-C composite electrode material. The BiF$_3$/Bi mixture should provide a reversible redox couple, as Bi was demonstrated to be reversible by previous authors.[14] Large amounts of LBF and carbon are used to ensure ionic and electronic percolation in the electrode. The mixture was simply hand-milled to avoid any side reactions between the components of the composite.

Figure III.4 shows the XRD pattern of the mixture. Main peaks can be assigned to LBF, Bi or β-BiF3 which correspond to the starting materials. Only small amounts of impurities, α-Bi$_2$O$_3$ and BiO$_{0.55}$F$_{1.90}$, coming from the Bi and BiF$_3$ commercial powders, could be detected. The low intensity of the peaks suggest that the minor phases are only in trace amounts. BiO$_{0.55}$F$_{1.90}$ could be detected in the starting BiF$_3$ commercial powder. The presence of α-Bi$_2$O$_3$ is attributed to surface oxidation of Bi commercial powder.
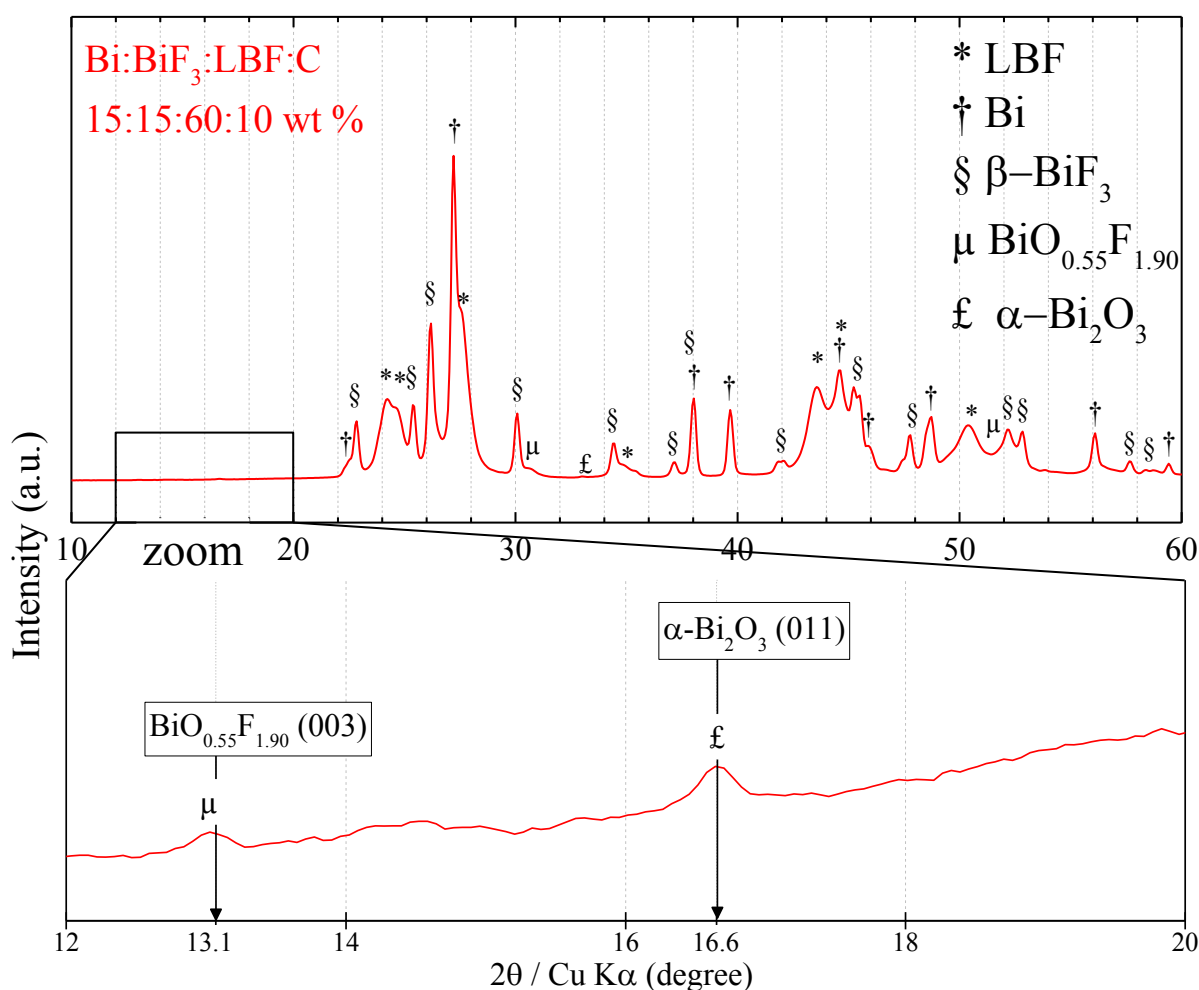
Figure III.4. *HEXRD pattern of the Bi-BiF₃-LBF-C composite prepared by hand-milling. A zoom in on the 12-20° region is added to show the presence of additional minor phases.*

The Bi/BiF$_3$ composite was used in Bi-BiF$_3$|LBF|Bi-BiF$_3$ symmetrical cells by pressing the powder stacks between two graphite disks. The graphite disks act as current collectors and mechanical supports so that the stack can be easily handled and placed in the coin-cell.

Two Bi-BiF$_3$|LBF|Bi-BiF$_3$ symmetrical cells were assembled and crimped in the modified coin-cell. One was covered with epoxy resin as described before and the other was not. The two cells were placed on the electrochemical test bench at 150 °C and cycled between 1 and -1 V at 4.5 µA/cm². The results of the galvanostatic cycling are presented for the two cells on **Figure III.5**.
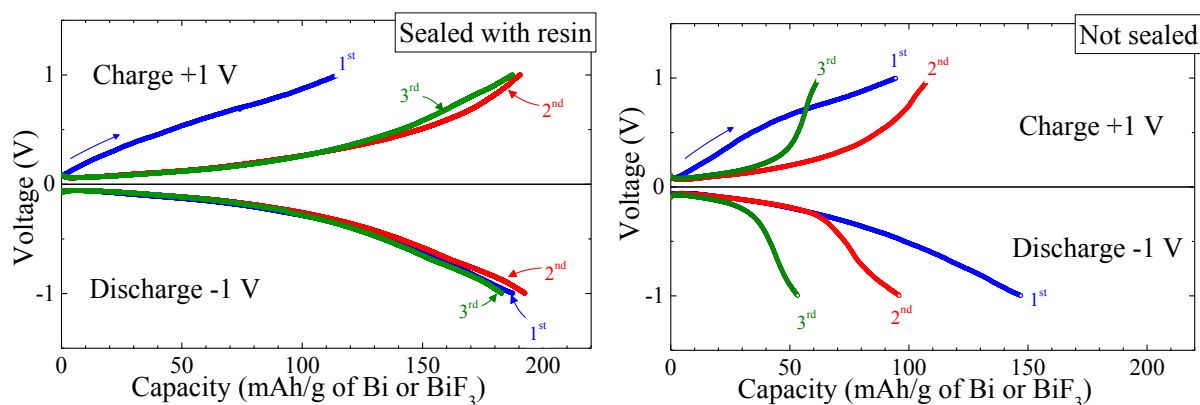
Figure III.5. *Charge-discharge curves obtained for the Bi-BiF₃-LBF-C|LBF|Bi-BiF₃-LBF-C symmetrical cells with epoxy resin sealing (left) or without (right). The cells were cycled with a current of 4.5 µA/cm² between +1 V and -1 V. The numbers indicate the order in which each charge/discharge was recorded.*

The potentials measured in the early stages of the charge/discharge processes for both cells (with or without resin) are not null (0.07 – 0.01 V). These values result from the presence of a resistive contribution which could be due to the resistances related to the charge/mass transport of the species within the electrode, and/or the passivation of the composite electrode resulting from insulating layers (e.g. Bi_2O_3). The larger values in the cell not sealed with resin (≈ 0.1 V), compared to the sealed cell (≈ 0.07 V), shows that the resistive contribution is larger in the former cell.

Both cells show similar behavior in the first cycle with a charge capacity lower than the discharge capacity. The cell sealed with resin exhibits a charge and discharge capacity about 25 % higher than the non-sealed cell, in agreement with the previous observations.

Upon subsequent cycling, charge and discharge capacities are almost identical for the sealed cell, while the cell not sealed with resin shows a progressive loss of capacity upon subsequent charge or discharge.

The discharge capacity higher than the charge capacity during the first cycle can be explained by the fact the BiF_3/Bi ratio is modified after the 1st charge, creating an excess of Bi at the cathode and an excess of BiF_3 at the anode. The Bi and BiF_3 converted during the 1st charge can then participate in the 1st discharge so that a larger capacity (about 70 %) is obtained.

The cycling behavior illustrating the capacities obtained for both cells is shown on **Figure III.6**. The overall capacity of the sealed cell is higher than that of the one that was not sealed. The

discharge capacity of the sealed cell remains stable at around 190 mAh/g for the first two cycles and slightly fades in the 3rd cycle (182 mAh/g).
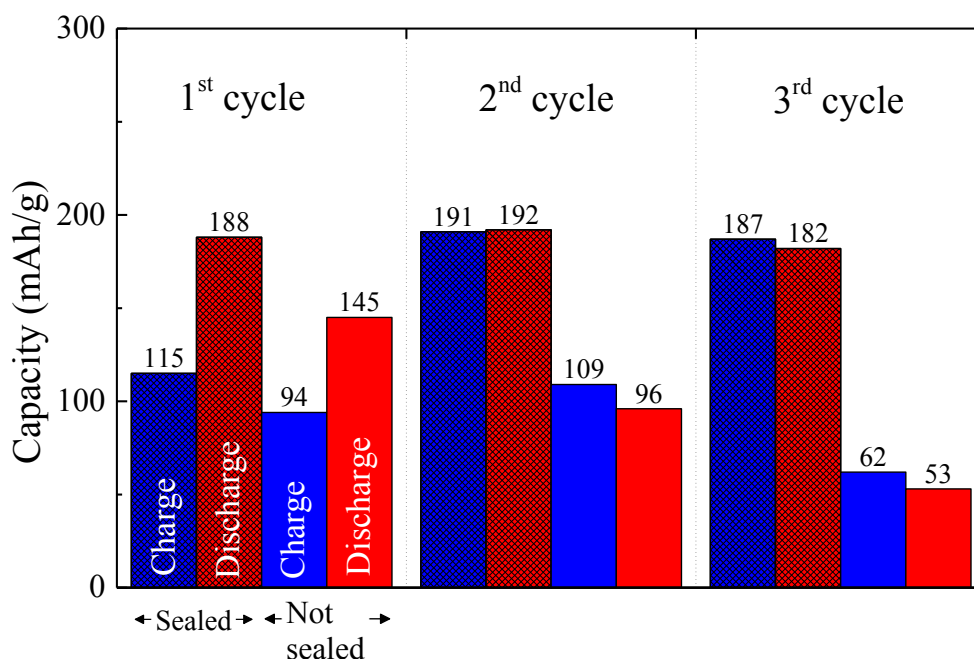

Figure III.6. *Comparative of the cycling behavior of the two Bi-BiF3 symmetrical cells with or without epoxy resin.*

For the non-sealed cell, the discharge capacity fades from 145, to 96, to 53 mAh/g between the 1st and 3rd cycle. The capacity fading observed in the non-sealed cell is significantly higher than in the coin-cell covered with epoxy resin.

Figure III.7 shows the Nyquist plot of impedance spectra recorded for the two cells, after the 1st and the 3rd charge-discharge cycles. The spectra are all composed of a single semi-circle. The low frequency zone of the Nyquist plots (**Figure III.7, insets**) shows the end of another contribution which can be attributed to the LBF layer. It is expected that the electrolyte layer exhibits a semi-circle at high frequencies, but the frequency used here is too low (i.e. 300 kHz) to show the entire semi-circle. A value of approximately 750 Ω for both cells is found, which is concomitant with the resistance given by a layer of LBF in our experimental conditions $(\sigma_i(150\ °C) \approx 9.4\times10^{-5}\ S.cm^{-1}$ for $La_{0.95}Ba_{0.05}F_{2.95})$[34].

The large semi-circle is attributed to electrode phenomena, such as charge transfer resistance. In the case of the sealed coin-cell, the resistance remains relatively similar between the 1st and 3rd cycles. For the coin-cell not sealed with resin, the resistance dramatically increases between the 1st and 3rd cycles.
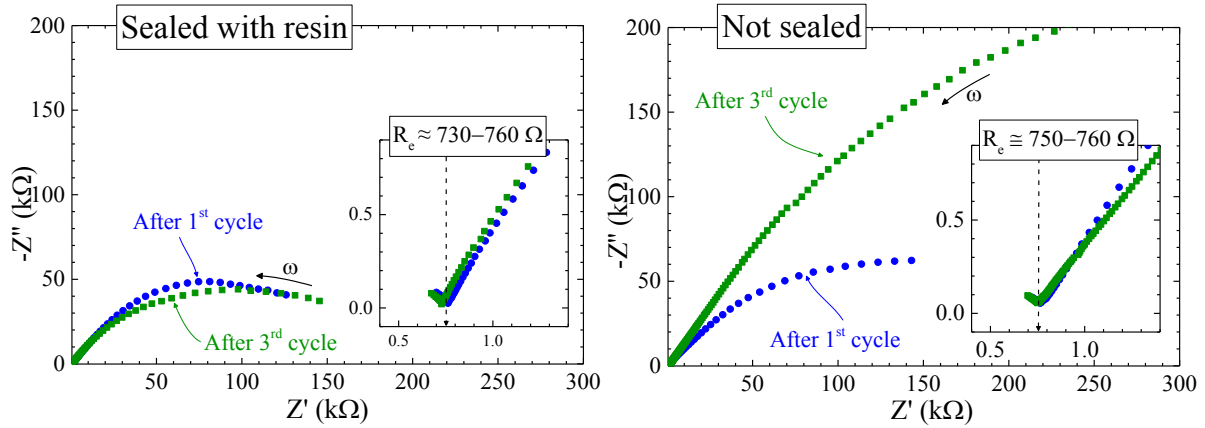
Figure III.7. *Nyquist plots of the impedance spectra recorded on the Bi-BiF₃-LBF-C|LBF|Bi-BiF₃-LBF-C cells with epoxy resin sealing (left) or without (right) after the 1ˢᵗ and 3ʳᵈ cycles. Insets: zoom in on the low frequency regions showing the end of the 1ˢᵗ semi-circle corresponding to the resistance of the LBF layer.*

The results exhibited by the impedance measurements support the capacity fading observed for the coin-cell not sealed with epoxy resin, as the resistance of the electrodes significantly increases upon cycling. In the case of the coin-cell sealed with epoxy, the stable resistance yielded by the electrodes upon cycling supports the capacity retention observed during successive charge-discharge experiments.

Figure III.8 shows photographs on the cells before and after the cycling experiment carried out at 150 °C. The total length of the experiment was approximately 1 month.

After such exposure, the outside surface of the epoxy resin is browned, perhaps due to oxidation. The resin was broken down to observe the condition of the coin-cell O-ring. The resin in contact with the coin-cell was not browned like on the outside surface and adhered relatively well with the metal surface of the coin-cell case. The PP O-ring of the coin-cell protected with resin was swollen but did not present any cracks or any sign of significant aging.
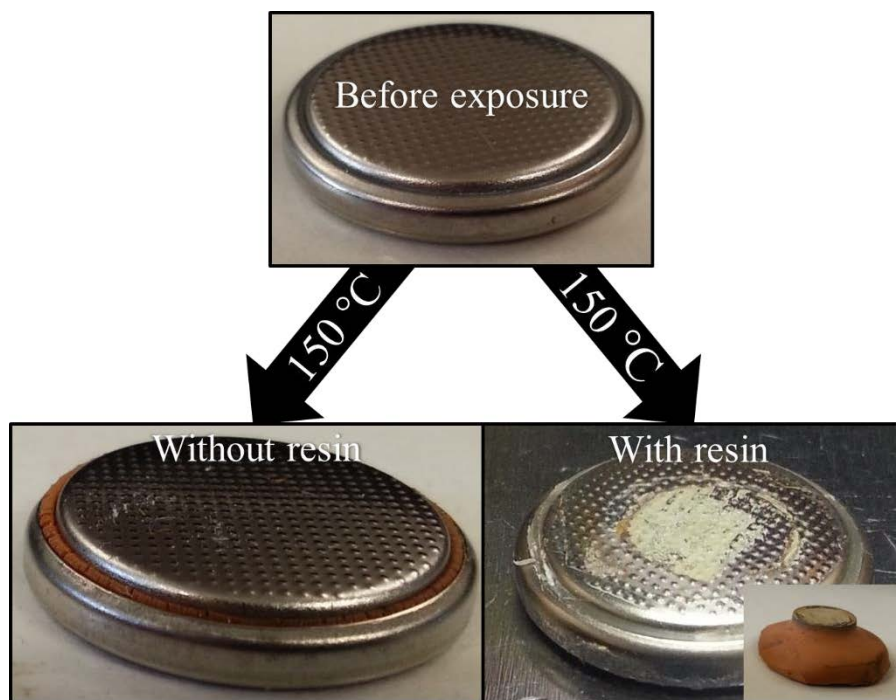
Figure III.8. Photographs of coin-cells before and after exposure at 150 °C for about 1 month, without or with the use of epoxy resin. The browned resin was broken down to let the O-ring visible.

However, the O-ring of the coin-cell not protected with resin was significantly aged and presented multiple cracks. The aged O-ring was brittle and could be readily broken down.

The observations made on the coin-cells suggest that the epoxy resin protected the PP O-ring from significant degradation, which probably allowed the cell to remain hermetical.

For the non-covered cell, the brittle nature and cracks present on the O-ring suggest that the sealing of the coin-cell was not achieved anymore, which may have allowed air to penetrate the coin-cell.

These observations are in agreement with the electrochemical results obtained on the corresponding cells. The penetration of air within the non-sealed coin-cell could be responsible for the progressive oxidation of the Bi-BiF$_3$ composite, leading to progressive capacity fading. The oxidation of the composite would also explain the increase of the resistance contribution given by the electrodes, as shown by impedance.

4. Conclusion

Sealing of coin-cells can be achieved at 150 °C by covering the cells with high-temperature epoxy resin. The operation is simple and rapid and can be applied to other electrochemical systems, provided that proper modification of the coin-cell interior is performed. The cell dimensions can be adapted to the coin-cell dimensions by using a washer to maintain the cell at the center of the coin-cell and with spacers to adjust the thickness.
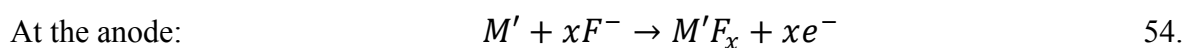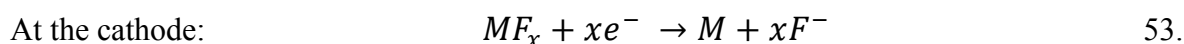
Electrochemical investigation on a Bi-BiF$_3$ symmetrical cell and observation of the coin-cells after experiment suggest that the epoxy-covered coin-cell can remain airtight over long period of time, at 150 °C, so that air-free electrochemical investigations can be performed outside the glovebox.

Chapter IV. Probing the reversible fluoride-ion electrochemical reaction by atomic pair distribution function analysis

1. Introduction

Owing to the high electronegativity of fluorine, the electrochemical reaction of a metal with fluoride ions to form a metal fluoride can lead to a large change in Gibbs energy, inducing high theoretical voltages. Therefore, fluoride-ion batteries (FIBs) which rely on the shuttle of fluoride ions may lead to theoretical energy densities as high as 5000 Wh.L^{-1}, depending on electrode material combinations[29]. Although the study of these systems was first started in the mid 70's[19], [22]–[24], [84], Anji Reddy and Fichtner were only recently the first to demonstrate the feasibility of a rechargeable FIB[14]. The proof of concept relied on the use of a metal as the anode and a metal fluoride as the cathode. Upon discharge, the metal fluoride cathode MF_x underwent a reduction down to its metallic state while the metal anode M' oxidized according to the following reactions:

At the cathode: $$MF_x + xe^- \rightarrow M + xF^-$$ 53.

At the anode: $$M' + xF^- \rightarrow M'F_x + xe^-$$ 54.

Overall: $$M' + MF_x \rightarrow M'F_x + M$$ 55.

Upon charge, the reactions occur in the opposite direction. These reactions imply multi-electronic processes during which fluoride ions flow through the electrolyte enabling the fluorination of the anode. These reactions can be categorized as conversion redox processes.

Since the pioneer work of Poizot *et al.*[8] on conversion reactions taking place in lithium-ion batteries, many researches have been devoted in understanding such complex reactions[85]. Particularly, it has been shown that conversion reactions induce the formation of nano-sized metallic clusters that can be subsequently oxidized while maintaining particle sizes of 1-3 nm. Such atomic re-arrangements have largely contributed to the complexity of these reactions as both finite-size effects and amorphization induce an absence of long-range order which precludes the use of conventional X-ray diffraction methods. To counter this, many techniques such as X-ray absorption, NMR, synchrotron diffraction etc. have been used to understand atomic structure, particle size and chemical compositions changes occurring upon conversion. The use of the atomic pair distribution function obtained from total X-ray scattering data has

been shown to be a powerful method to probe electrochemical reaction mechanisms[10], [13], [86]–[88].

A comprehensive understanding of the electrochemical reaction mechanism occurring in FIBs is of fundamental interest to help developing the next generation of high energy density batteries. Since reaction mechanisms occurring in FIBs have been mostly investigated using conventional techniques such as XPS and laboratory XRD[14], [29] the use of synchrotron diffraction along with PDF analysis will help to obtain deeper structural insights on the mechanisms involving fluoride-ion based conversion reactions. As a model system, the BiF_3/Bi redox couple has been selected due to its proved reversibility. Moreover, since electrodes in solid state batteries require the use of composites containing up to 60 wt % of electrolyte, the use of heavily scattering elements is mandatory to enable probing structural changes occurring in the active material. A symmetrical cell using $Bi-BiF_3-LBF-C$ composites is used to evaluate the reversibility of the BiF_3/Bi redox couple. Synchrotron data coupled with PDF analyses allowed to probe the electrochemical reactions taking place in such cells.

2. Experimental

Unless specified otherwise, all the manipulation of the materials and assembly of the cells were carried out in a dry Ar glove box ($H_2O < 2$ ppm).

2.1. Preparation of the materials

All powdered materials were outgassed for 12 hours at 150 °C in a vacuumed atmosphere, then placed in the glove box without any contact with air.

$La_{0.95}Ba_{0.05}F_{2.95}$ (LBF) electrolyte was prepared by ball-milling stoichiometric amounts of LaF_3 (Alfa Aesar, 99.99 %) and BaF_2 (Strem chemicals, 99.99 +%) in Ar atmosphere (Johann Chable and Ana Gil Martin, IMMM, Le Mans). The powders were placed in the airtight milling bowl inside the glove box then taken out for milling. A Fritsch mini pulverisette 7 premium line planetary mill with ZrO_2 grinding bowls and ZrO_2 grinding balls (10 mm diameter) was used. To produce 4 g of LBF, the mixture was ball-milled for a total of 12 hours (48 cycles of 15 min with 15 min pauses) at a rotational speed of 400 rpm.

To prepare the $Bi-BiF_3-LBF-C$ composite electrode, $\beta-BiF_3$ (Alfa Aesar, 99.999%) and Bi (Alfa Aesar, -200 mesh, 99.999%) commercial powders were mixed with LBF and carbon black in

15:15:60:10 % wt ratio. The mixture was hand-milled for about 30 minutes with an agate mortar and pestle.

2.2. Cell assembly

The symmetrical cell was assembled using 15.6 mg (working electrode) and 16.6 mg (counter electrode) of the Bi-BiF$_3$-LBF-C composite, and 200.0 mg of electrolyte. The powdered stack was pressed in a ⌀10 mm stainless steel die with an uniaxial press (Specac Atlas), at a load of 5 tons. Two graphite disks (C$_g$) were pressed with the powdered stack to form a C$_g$|Bi-BiF$_3$-LBF-C|LBF|Bi-BiF$_3$-LBF-C|C$_g$ cell in a single step. The graphite disks were directly pressed with the powders to provide a good contact between the composite and the current collector and to ensure the easy handling of the pellet stack. Graphite disks (Cg) were cut from high purity graphite rods (Mersen). Graphite rods were previously machined to reduce their diameter so that they would fit the pressing mold. The discs were then polished with grit P400 SiC abrasive paper, degreased in acetone then sonicated three times in ultra-pure water for *ca.* three minutes. Finally, Cg disks were dried at 70 °C under air overnight, and outgassed at 150 °C for 12 h under vacuum atmosphere. The disks were then entered in the glovebox without any contact with air. Typical thickness of the graphite discs was 0.5 – 0.7 mm.

The stack was placed in a CR2032 coin-cell (MTI Corp, 304 stainless steel) with a flat wave spring and a spacer. A flat PTFE washer (⌀$_{ext}$ 16.0 mm, ⌀$_{int}$ 10.5 mm, 1.5 mm thickness) was used to maintain the cell in the center of the coin-cell. Finally, the coin-cell was covered with high-temperature epoxy resin (Loctite EA 9492) to keep the cell airtight for the duration of the electrochemical experiments.

2.3. Electrochemical evaluation

The modified coin-cell was placed on a custom-made electrochemical test bench placed in an oven at 150 °C. The test bench was connected to an AMETEK PARSTAT PMC 500 potentiostat for galvanostatic measurements. The cycling was performed between 1 V and -1 V at a current density of 4.5 µA/cm² ($\approx$ 1.5 mA/g of Bi).

2.4. PDF analysis

After cycling, the cells were opened in the glovebox and the Bi-BiF$_3$-LBF-C composites were scrapped off the surface of the electrolyte with a scalpel. The powdered samples were packed

in Kapton capillaries (Cole-Parmer®, polyimide tubing, 0.0435" outside diameter, 0.0020" wall) and sealed using epoxy resin under argon atsmosphere.

Hard X-rays were collected at the 11-ID-B beamline of the Advanced Photon Source of Argonne National Laboratory, USA. Total scattering data were recorded at 58.66 keV (λ_1 = 0.21140 Å), using a 2D amorphous silicon-based area detector (PerkinElmer). Total scattering data I(Q) were obtained by using the FIT2D software.

Data adapted for XRD were recorded with a sample to detector distance of about 945 mm to optimize them for 2θ resolution. The *I(Q)* data could be conveniently converted to *I(2θ)* classical CuKα XRD (λ_2 = 1.5418 Å) data using the relation:

$$Q = \frac{4\pi \sin\theta}{\lambda_2} \qquad \rightarrow \qquad 2\theta = 2\arcsin\frac{Q\lambda_2}{4\pi} \qquad\qquad 56.$$

For PDF analysis, a sample to detector distance of 175 mm was employed to obtain high values of momentum transfer Q. I(Q) was converted to the PDF using PDFgetX2 software.[89] Data were corrected for background contribution, detector effects, and Compton and diffuse scattering to obtain the PDF $G(r)$. The refinement of the PDF was performed using PDFgui.[90] Structural models were taken from the inorganic crystal structure database (ICSD). The refined parameters were the lattice parameters, scale factor, sratio, spdiameter (if relevant), and isotropic atomic displacement factors (ADPs). Similar isotropic ADPs were set for similar atoms. The Q dampening factor (Q_{damp}) was fixed to 0.045. For minor phases the ADPs were fixed to 0.008 for cations and 0.01 for anions.

3. Results and discussion

3.1. Characterization of the Bi-BiF₃-LBF-C composite

Composite electrodes, particularly for solid-state batteries, can feature complex X-ray diffraction patterns owing to multiple phases which need to be clearly identified to understand electrochemical reactions. **Figure IV.1** shows the HEXRD pattern of the as-prepared Bi-BiF₃-LBF-C composite. In addition to patterns ascribed to starting compounds such as LBF, Bi and β-BiF₃, low intensity peaks distinguishable below 20° (**Figure IV.1, zoom**) indicate the presence of Bi-oxide and oxyfluoride phases.

(N.B.: **Table IV.4** (supporting information) summarizes all the crystalline phases and their crystallographic information.)
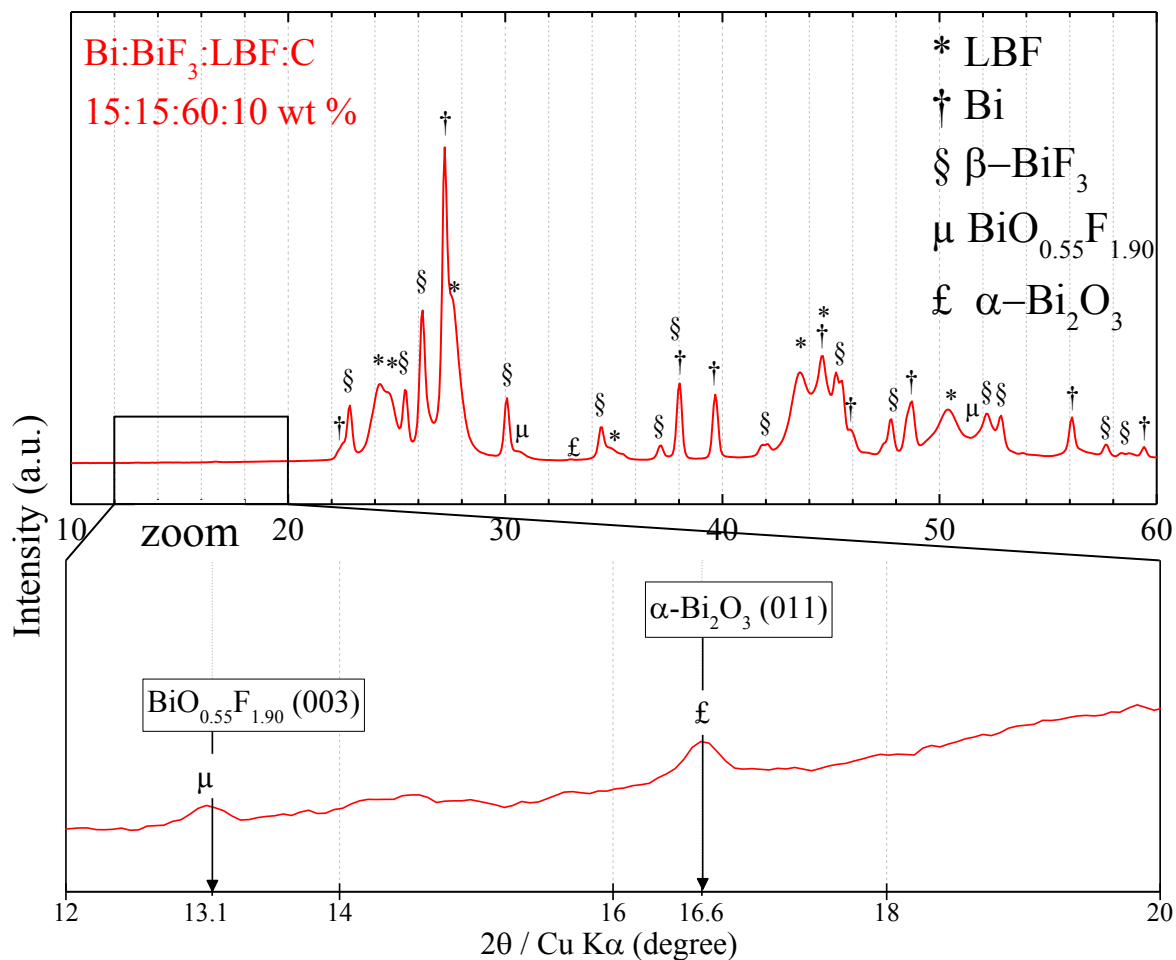
Figure IV.1. *HEXRD pattern of the Bi-BiF₃-LBF-C composite prepared by hand-milling. A zoom in on 12-20° region is added to show the presence of additional minor phases.*

Low intensity peaks at 16.6° and 33.0° can be assigned to α-Bi_2O_3. Its presence is attributed to the starting Bi commercial powder.

The peak at 30.5° and the shoulder at 51.8° can be assigned to either fluorite-type α-BiF_3, or $BiO_{0.55}F_{1.90}$. The latter presents a fluorite-type defect structure,[91] and yields a similar diffraction pattern than α-BiF_3 (**Figure IV.2**). However, the diffraction pattern of $BiO_{0.55}F_{1.90}$ presents additional low intensity peaks (**inset Figure IV.2.**) Particularly, a peak at 13.1°, corresponding to a peak observed on the HEXRD pattern of the composite (**Figure IV.1, zoom**), suggests that the additional phase is $BiO_{0.55}F_{1.90}$ and not α-BiF_3. The presence of $BiO_{0.55}F_{1.90}$ could be detected on the starting β-BiF_3 commercial powder and is not related to a reaction of the materials during the preparation of the composite.
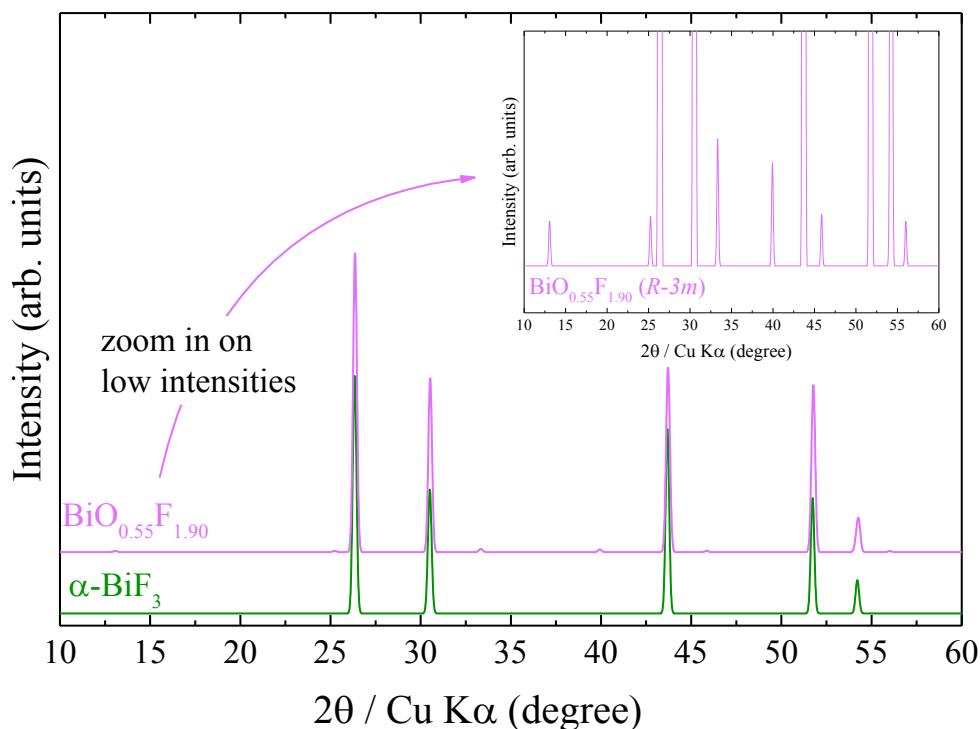
Figure IV.2. *XRD patterns of α-BiF₃ and BiO₀.₅₅F₁.₉₀ taken from ICSD database (see supporting information for details). In inset is a zoom of the low intensity region of the XRD pattern of BiO₀.₅₅F₁.₉₀ showing additional peaks compared to α-BiF₃.*

PDF analysis was further performed on the Bi-BiF₃-LBF-C composite. Refinements of the PDF data were performed aiming to obtain a quantitative analysis. Attempts to refine the data with the presence of Bi-oxide failed resulting in a negative scale factor or erroneous cell parameters. This is probably due to the fact that even if it is detectable by HEXRD, its weak concentration along with probable absence of long-range order prevents its detection by PDF. Moreover, the influence of the addition of $BiO_{0.55}F_{1.90}$ on the quality of the fit and the weight proportion of each phase, was examined. The weight ratio of each phase as well as the value of the reliability factor R_w for both fits are gathered in

Table IV.1.

Weight percent of the phase in the pristine Bi-BiF$_3$-LBF-C composite			
	Refinements		Theoretical
LBF	77.9 (4)	73.0 (5)	66.6
Bi	9.2 (3)	9.4 (2)	16.7
β-BiF$_3$	12.9 (7)	13.0 (3)	16.7
BiO$_{0.55}$F$_{1.9}$		4.6 (4)	
Rw	**0.137**	**0.124**	

Table IV.1. Results of the fits (1.5 – 25 Å) in terms of weight percent for the hand-milled Bi-BiF$_3$-LBF-C composite carried out without (1st column) and with (2nd column) BiO$_{0.55}$F$_{1.9}$ as additional phase. For both fit, the mean crystallite size (spdiameter) of LBF was approximately 7 nm. The mean crystallite size of BiO$_{0.55}$F$_{1.9}$ was 5 nm.

Refinement without BiO$_{0.55}$F$_{1.9}$ results in a satisfactory, but less good Rw of 0.137. The better Rw (0.124) of the fit taking into account the contribution of BiO$_{0.55}$F$_{1.9}$ (4.6 wt %) confirms its presence. The coherence length of BiO$_{0.55}$F$_{1.9}$ obtained by PDF yields 4 nm, showing that this phase features nano-sized crystals and/or disorder. In both fits, the quantity of LBF is overestimated compared to the expected value (66.6 wt %). When BiO$_{0.55}$F$_{1.9}$ is included, the proportions of the main phases draw nearer to the expected values, but the proportion of LBF remains larger than expected. The total weight percentage of β-BiF$_3$ and BiO$_{0.55}$F$_{1.9}$ yields 17.6 wt % and is in good agreement with the 16.7 wt % expected. Note that quantity of Bi detected in all the fits performed This shows that PDF refinement provides quantitative analysis. Therefore, although the presence of Bi-oxide could not be probed by PDF analysis, it can then be estimated by comparing the refined wt % of Bi, i.e. 9.4, with the 16.7 wt % expected, resulting in approximately 7 wt % of Bi-oxide in the composite. Such an amount should be detectable by PDF, suggesting that several Bi-oxide compositions arising from the partial oxidation of Bi are present in the composite. The final refinement along with the contribution of each phase (LBF, Bi, β-BiF$_3$ and BiO$_{0.55}$F$_{1.90}$) to the overall fit curve is shown in **Figure IV.3**.
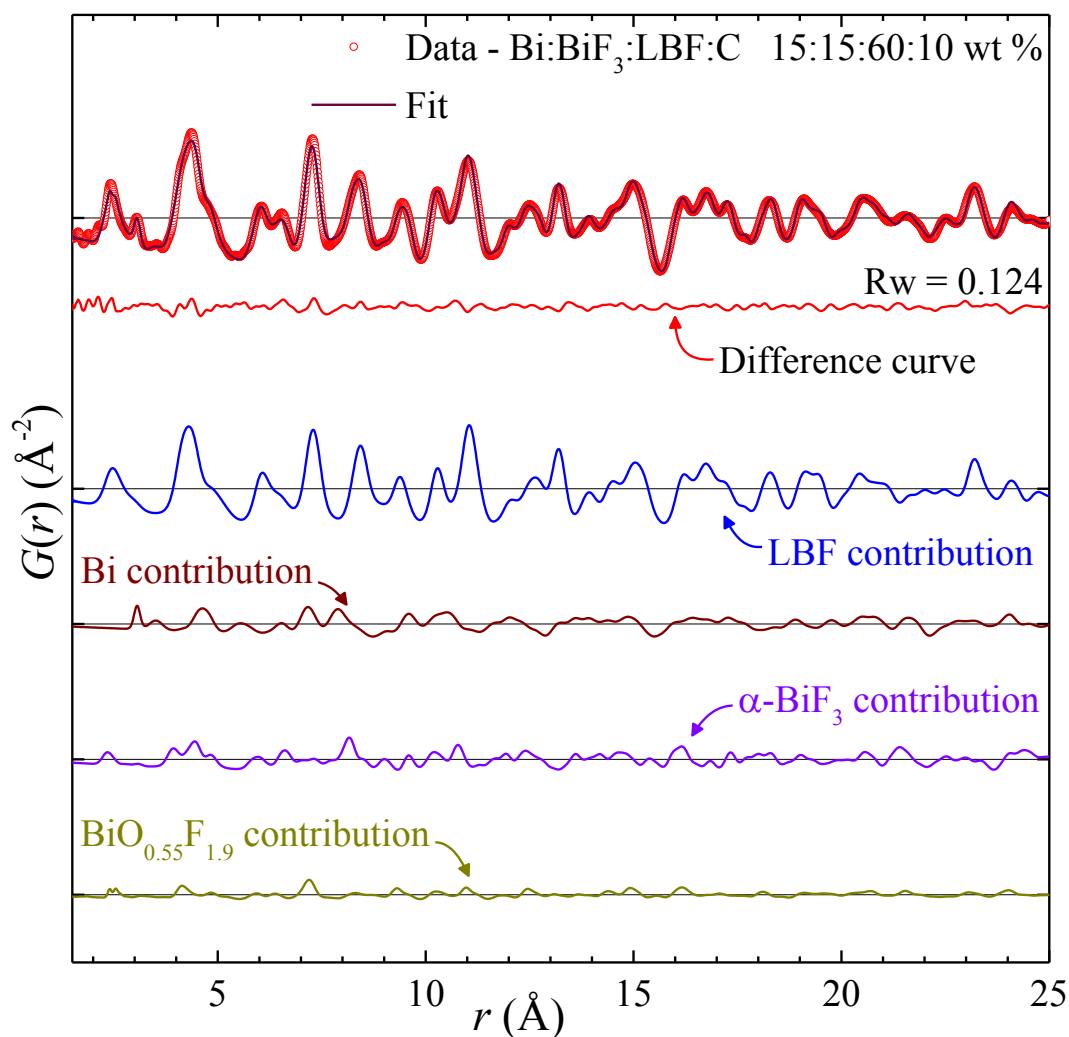
Figure IV.3. *PDF analysis performed between 1.5 and 25 Å on the Bi-BiF₃ composite with 4 phases: LBF, Bi, β-BiF₃ and BiO₀.₅₅F₁.₉. The difference between the data and the refinement is illustrated by the difference curve. The contribution of each phase to the fit is shown for illustration purposes.*

3.2. Electrochemical test

The Bi-BiF₃ composite was tested in a symmetrical cell to evaluate its electrochemical performance and the reversibility of the redox reactions involved. The results of the galvanostatic cycling performed on the cell is shown on **Figure IV.4**. Since the same redox couple is present at each electrode, the cell shows an OCV close to 0 V and is cycled between +1 and -1 V. The first charge (up to 1 V) yields a capacity of 115 mAh/g which is about 30 % and 38 % of the theoretical capacity of Bi (384.7 mAh/g) and BiF₃ (302.3 mAh/g). Note that in this configuration, BiF₃ is the limiting active material.
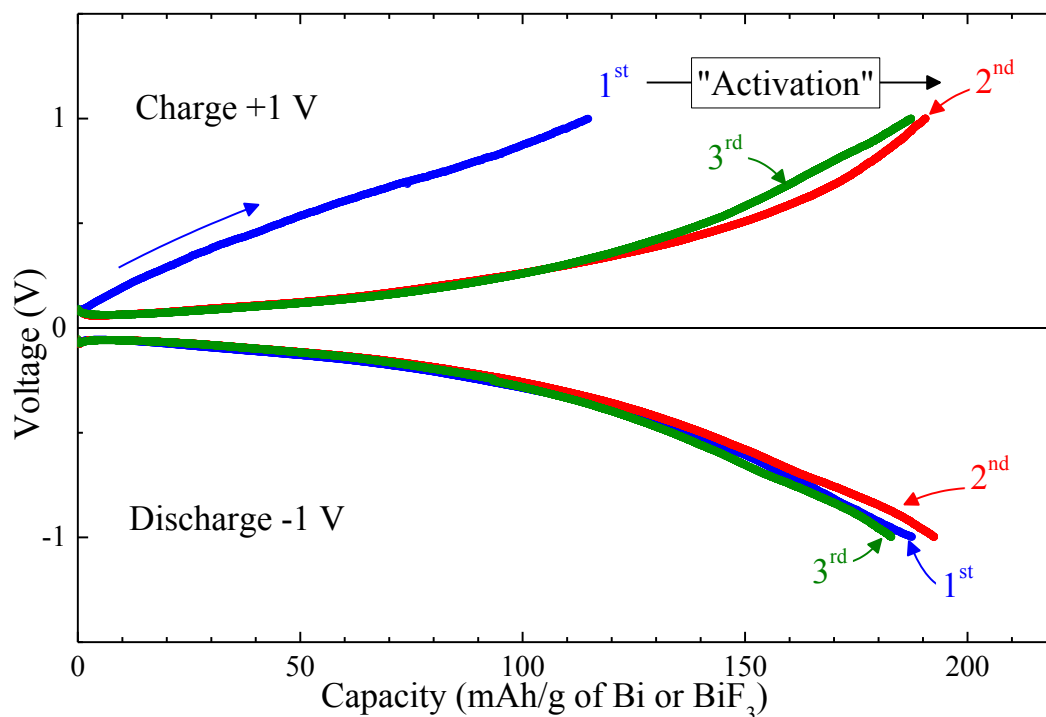
Figure IV.4. *Galvanostatic (3.5 µA) charge-discharge curves between +1 and -1 V for a Bi-BiF₃-LBF-C|LBF|Bi-BiF₃-LBF-C cell using hand-milled Bi-BiF₃-LBF-C (15:15:60:10 wt %) composite electrodes. The experiment started with the charge (+1V), as symbolized by the blue arrow.*

The subsequent discharge (down to -1 V) yields a higher capacity of 190 mAh/g, suggesting an activation of the electrode after the first charge. Upon cycling, the capacity remains stable and similar charge/discharge profiles are observed.

After the first charge, the initial 50/50 ratio between Bi/BiF₃ at each electrode is modified yielding an excess of Bi at the working electrode (cathode), and an excess of BiF₃ at the counter electrode (anode). The configuration is no longer symmetrical, as the electrodes will contain different Bi/BiF₃ ratios (**Figure IV.5**). Upon discharge, additional Bi present at the working electrode (now the anode) and additional BiF₃ present at the counter electrode (cathode) will be available for conversion, yielding higher capacity.
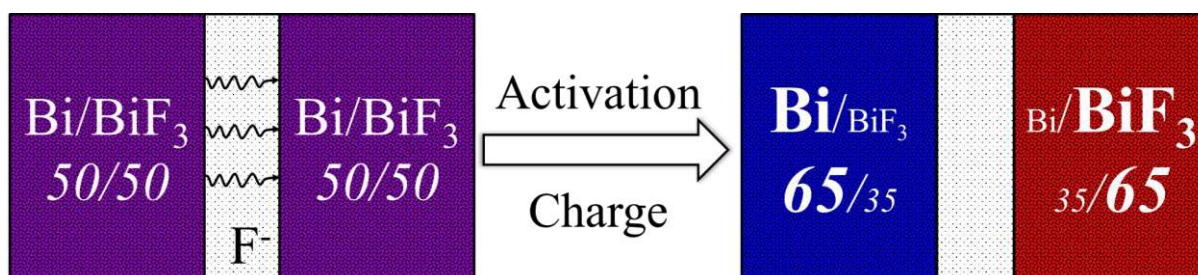
***Figure IV.5.*** *Illustration of the activation process observed on the galvanostatic cycling curves shown in **Figure IV.4**. The 65/35 weight ratio is a rough estimation calculated considering that about 30 % of Bi is converted during the first charge.*

The activated electrodes show a stable capacity with little fading after 3 cycles. To understand the electrochemical reactions involved, cycling was stopped after the third discharge. The electrodes were characterized by means of HEXRD and PDF analyses.

3.3. Characterization of the cycled materials

The HEXRD patterns of the cycled electrodes are presented on **Figure IV.6**. A comparison with the HEXRD pattern of the pristine composite indicates significant changes induced by the electrochemical reactions. The electrode at the cathode side features a reduced state characterized by Bi being less present at the anode side (oxidized state). For both electrodes, the peaks attributed to β-BiF$_3$ have almost entirely disappeared while peaks characteristic of the oxyfluoride phase BiO$_{0.55}$F$_{1.9}$ have increased in intensity. The weak peak at about 16.6°, assigned to α-Bi$_2$O$_3$ in the pristine material, has evolved (either shifted or decreased in intensity) upon cycling, indicating the implication of Bi oxide in the electrochemical reaction. Moreover, low intensity peaks attributed to Bi$_7$F$_{11}$O$_5$, and BiOF can be detected (**Figure IV.6, zoom**) further supporting the implication of O^{2-} in the electrochemical processes. Note that a peak located at 18.6° could not be assigned to any Bi-related phase reported in the ICSD crystallographic database.

The implication of O^{2-} in the electrochemical process is also supported with the work of previous authors who detected the formation of β-BiF$_{3-2x}$O$_x$ with a cubic (fluorite-type) structure ($0.41 \leq x \leq 0.52$) during the charging of a Bi *vs.* CeF$_3$ cell.[29] The formation of the phase was attributed to the fluorination of the Bi$_2$O$_3$ phase present in their starting Bi powder.
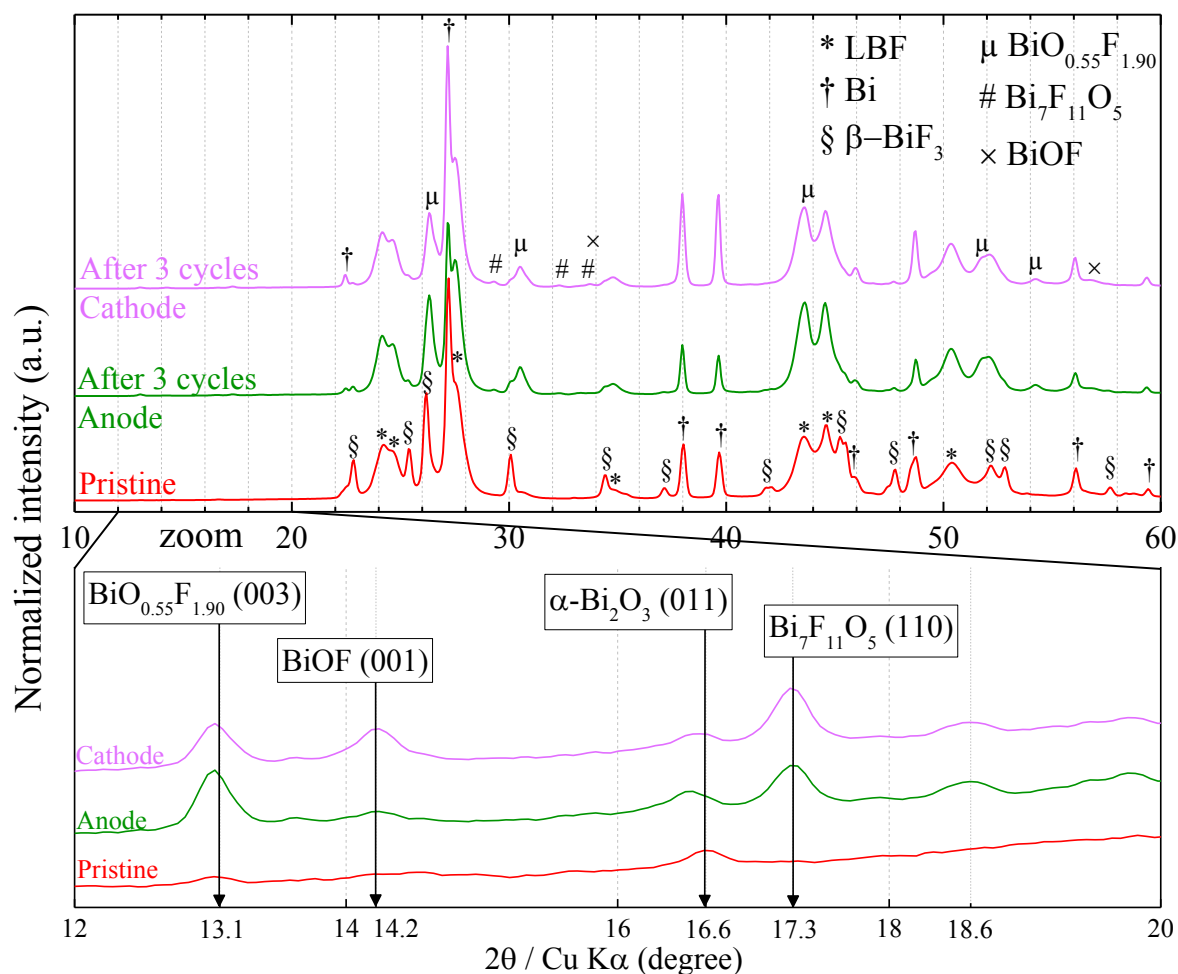
Figure IV.6. *HEXRD pattern of the Bi-BiF₃-LBF-C composites before (pristine) and after 3 cycles between +1 and -1 V at 3.5 µA at 150 °C. CE refers to the counter electrode and WE to the working electrode. During the last discharge (3ʳᵈ cycle), the WE was the anode and the CE the cathode. A zoom in on 12-20° region is added to show the presence of additional minor phases.*

To gain further insight into the electrochemical reaction mechanisms, PDF analysis was carried out on the cycled electrodes and compared to the results obtained for the pristine material. The phases used to perform the fitting of the cycled electrodes include LBF, Bi, β-BiF₃, BiO₀.₅₅F₁.₉₀ and Bi₇F₁₁O₅. Attempts to refine BiOF in the cycled electrodes failed, suggesting that it is present in small amount. **Figure IV.7** shows the results of the PDF refinements with reliability factors of 0.143 and 0.123, for the cathode and anode, respectively. Quantitative phase analysis obtained from the refinements is reported in **Table IV.2**.
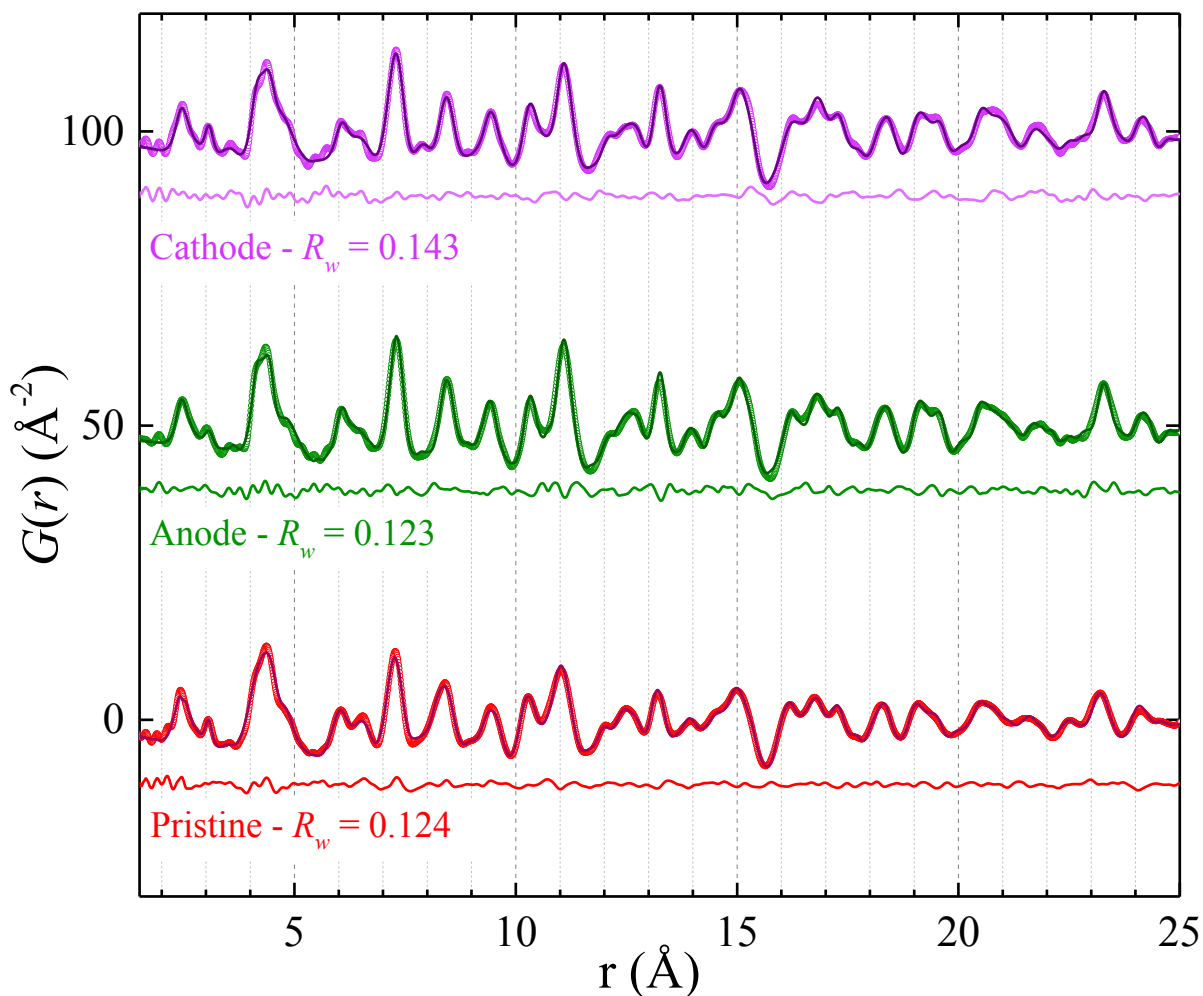
Figure IV.7. *PDF analyses performed between 1.5 and 25 Å on the Bi-BiF₃ composites before and after cycling.*

Weight percent of the phase in the Bi-BiF$_3$-LBF-C composite

	Pristine	Anode	Cathode
LBF	73.0 (5)	72.1 (6)	73.2 (6)
Bi	9.4 (2)	7.4 (3) ↓	14.9 (3) ↑
β-BiF$_3$	13.0 (3)	2.9 (4) ↓	< 1 ↓
BiO$_{0.55}$F$_{1.9}$	4.6 (4)	14.0 (3) ↑	8.1 (3) ↑
Bi$_7$F$_{11}$O$_5$		3.6 (5) ↑	3.8 (5) ↑
R$_w$	**0.124**	**0.123**	**0.143**

Table IV.2. *Quantitative phase analysis obtained from PDF refinements (1.5 – 25 Å) for the pristine and cycled Bi-BiF₃-LBF-C composites.*

The phase analysis provides a direct insight into the reaction mechanism. The difference in the Bi proportions between the anode and the cathode corresponds to 7.5 wt % which translates to a capacity of 191 mAh.g^{-1} based on the Bi to BiF$_3$ conversion mechanism, which is in good agreement with the measured capacity. Strikingly, BiF$_3$ did not form back and instead several oxyfluoride phases appeared, demonstrating the implication of both O^{2-} and F$^-$ anions in the conversion mechanism. The formation of the different Bi oxyfluoride phases is likely due to the fluorination of Bi oxides present at the surface of the Bi particles. Therefore, the stabilization of the oxyfluoride phases depends on the final F/O molar ratio exhibited by the phase. It can be suggested that the fluorination reaction of Bi oxides first yields BiOF (F/O = 1). Then upon increasing fluorination, the different stabilized phases are in the following order: Bi$_7$F$_{11}$O$_5$ (F/O = 2.2), BiO$_{0.55}$F$_{1.9}$ (F/O = 3.45) and finally BiF$_3$. Note that BiO$_{0.1}$F$_{2.8}$ (F/O = 28) presents a tysonite-type structure and yields similar XRD and PDF patterns than LBF which might prevent its detection.

The redox reactions underwent by the oxyfluorinated phases, particularly BiO$_{0.55}$F$_{1.9}$, is an opened question and largely depends on the mobility of oxygen ions. By analogy with electrochemical reaction with lithium,[92] Bi oxyfluoride can be reduced following a two-step process implying anionic partitioning (Eq. 57 & 58) Alternatively, Bi oxyfluoride may undergo a single step redox process (Eq. 59.)

For BiO$_{0.55}$F$_{1.9}$, the two reaction mechanisms can be written as follow:

$$BiO_{0.55}F_{1.9} + 1.9\ e^- \leftrightarrow 0.183\ Bi_2O_3 + 0.634\ Bi^0 + 1.9\ F^- \qquad 57.$$

$$0.183\ Bi_2O_3 + 1.1\ e^- \leftrightarrow 0.366\ Bi^0 + 0.55\ O^{2-} \qquad 58.$$

$$BiO_{0.55}F_{1.9} + 3.0\ e^- \leftrightarrow Bi^0 + 1.9\ F^- + 0.55\ O^{2-} \qquad 59.$$
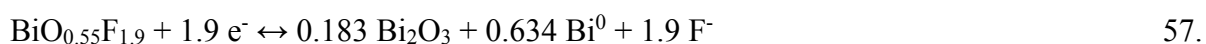
In the above mechanisms, it might possible that under the electric field, both fluoride and oxide anions can migrate through the LBF to further react at the opposite electrode.

The partial replacement of F$^-$ by O^{2-} is a common phenomenon in solid-state chemistry, owed to their relatively similar ionic radius[93], [94]. The migration of oxides through oxygen doped tysonite-type fluoride electrolyte has already been investigated[95]. In our case, the doping of the LBF could come from the migration of oxygen ions under the influence of the electric field. The electroneutrality of the crystal would be maintained by the creation of additional anionic vacancies (2 F$^-$ ↔ O^{2-} + □) to yield La$_{0.95}$Ba$_{0.05}$F$_{2.95-2y}$O$_y$. Because the ionic radius of O^{2-} is slightly larger than that of F$^-$, the migration and possible incorporation of O^{2-} into the LBF might impact the structure of the electrolyte. The cell parameters and volume (**Table IV.3**) of

the electrolyte contained in the cycled electrodes were obtained from PDF refinements. The refinement obtained for a pure LBF reference is added for comparison.

		a = b (Å)	c (Å)	V (Å³)	Estimated particle size (nm)
LBF ref.	Pure LBF	7.188 (1)	7.356 (2)	329.15	8
LBF in the composite	Pristine	7.186 (1)	7.365 (2)	329.37	8
	Anode	7.218 (1) ↑ +0.032	7.390 (1) ↑ +0.025	333.44 ↑ +4.07	12 ↑
	Cathode	7.222 (1) ↑ +0.036	7.393 (2) ↑ +0.028	333.94 ↑ +4.57	15 ↑

Table IV.3. *Results of the fits (1.5 – 25 Å) in terms of cell parameters, cell volume and estimated particle size ("spdiameter") of LBF in the composite before and after cycling.*

The analysis reveals that the electrolyte experiences a volume expansion upon cycling, which might be due to the partial replacement of F⁻ by O²⁻ in the anion sublattice of LBF. Further experiments are underway to evaluate the possibility of a migration of oxygen ions in the LBF.

4. Conclusion

In conclusion we saw that the BiF_3/Bi redox couple provides a reversible electrode. Symmetrical cells with Bi-BiF_3-LBF-C composite prepared by simple hand-milling could by cycled without significant capacity fading for 3 cycles. This is attributed to the reorganization of the electrode's structure after an activation process occurring during the first cycle, allowing mass and charge transport throughout the bulk of the electrode.

Thanks to *ex-situ* synchrotron XRD associated with PDF analysis, we determined that the electrochemical reactions involve Bi, β-BiF_3 and a large range of bismuth oxyfluoride compounds, including $BiO_{0.55}F_{1.9}$, $BiOF$ and $Bi_7F_{11}O_5$. This observation suggests the formation of successive bismuth oxyfluoride/fluoride layers with increasing F/Bi ratios forming a gradient of concentration upon fluorination of the Bi. We assume the high reversibility and relatively good capacity (about 190 mAh/g) is owed to conductivity properties of bismuth oxide, fluoride and oxyfluorides. Moreover, the results suggest that both fluoride and oxygen ions can migrate through the LBF due to a partial replacement of F⁻ by O²⁻ in the anion sublattice of LBF.

These promising results open the path to the study of other active materials for FIBs and the evaluation of their reversible oxyfluoride-based electrochemical conversion.

5. Supporting information

Phase name	Crystal system	Space group	a (Å)	b (Å)	c (Å)	α (°)	β (°)	γ (°)	Ref./ICSD Coll. Code
$La_{0.95}Ba_{0.05}F_{2.95}$	Trigonal	$P\text{-}3c1$	7.20	7.20	7.37	90	90	120	Rongeat *et al.*[34]
$La_{0.95}Ba_{0.05}F_{2.95}$	Trigonal	$P\text{-}3c1$	7.205	7.205	7.371	90	90	120	Chable J.[43]
LaF_3	Trigonal	$P\text{-}3c1$	7.185	7.185	7.351	90	90	120	23972
$Ce_{0.95}Bi_{0.05}O_{0.05}F_{2.90}$	Trigonal	$P\text{-}3c1$	7.131	7.131	7.290	90	90	120	Rhandour *et al.*[96]
CeF_3	Trigonal	$P\text{-}3c1$	7.131	7.131	7.286	90	90	120	4
Bi	Trigonal	$R\text{-}3m$	4.546	4.546	11.862	90	90	120	64703
$\alpha\text{-}Bi_2O_3$	Monoclinic	$P21/c$	5.844	8.157	7.503	90	113	90	94229
$\beta\text{-}BiF_3$	Orthorhombic	$Pnma$	6.561	7.015	4.841	90	90	120	1269
$\alpha\text{-}BiF_3$	Cubic	$Fm\text{-}3m$	5.861	5.861	5.861	90	90	90	24522
$BiO_{0.1}F_{2.8}$	Hexagonal	$P63/mmc$	4.083	4.083	7.323	90	90	120	24056
$BiO_{0.55}F_{1.9}$	Trigonal	$R\text{-}3m$	4.138	4.138	20.321	90	90	120	Laval *et al.*[91]/50823
$Bi_7F_{11}O_5$	Monoclinic	$C121$	13.524	5.529	9.189	90	96	90	167074
BiOF	Tetragonal	$P4/nmm$	3.747	3.747	6.226	90	90	90	24096

Table IV.4. *Crystallographic data relevant to the phases observed during the study of the Bi-BiF₃ composite electrodes. Please refer to the corresponding reference or ICSD collection code for more details. a, b and c represent the lattice parameters and α, β and γ the lattice angles.*

Conclusion and outlooks

Solid-state fluoride-ion batteries are considered in the literature and from a theoretical point of view, as promising electrochemical devices, since these batteries are able to deliver high energy densities compared to commercial ones. However, the scarcity of literature as compared to their Li-ion homologue makes the development of rechargeable F-ion batteries (FIBs) particularly challenging. One of the main objective of this work was to explore and discuss the challenges and pertinent approaches to help developing FIBs through the investigation of all of the cell components.

The first challenge that needed to be addressed was the absence of a reference electrode well adapted to the electrochemical studies. Indeed, most battery chemistries rely on the shuttle of metallic cation charge carries such as Li^+, Na^+, Mg^{2+} etc. The corresponding metal can thus be conveniently used as reference electrode. However, for FIBs, the elemental form of fluoride is fluorine, a highly toxic and corrosive gas, which is obviously not adapted as reference electrode. We established that lithium can act as a proper reference electrode for FIBs. Indeed, the solid electrolyte interface (SEI) formed upon contacting lithium with the state of the art fluoride solid electrolyte $La_{1-x}Ba_xF_{3-x}$, is stable. Time-resolved impedance measurements revealed that this SEI is not blocking, as its resistance is inferior to the resistance of the LBF in our experimental setup. The SEI is probably formed of LiF and a mixture of La/Ba created upon spontaneous reduction of LBF. The LiF/Li redox couple thus created, allowed the evaluation of the electrochemical properties of LBF. Moreover, cyclic voltammetry experiments performed with a LBF-carbon composite seems to confirm the thermodynamically predicted reaction of carbon with fluorides to yield graphite fluoride CF_x, at potentials lower than the decomposition of LBF. Potentiostatic measurements associated with ^{19}F NMR measurements are planned to confirm the formation of CF_x in the LBF-C composite. The fluorination of carbon to give insulating graphite fluoride could be a serious limitation to operate FIBs, notably in terms of operating potential. However, it also opens the way for new opportunities to develop high-energy FIBs as the fluorination of lightweight carbon could be reversible in such systems. Moreover, these results open a new way to better understand the underlying electrochemical mechanisms taking place in FIBs. Indeed, the use of three-electrode setups will allow to observe the potential of a single electrode, allowing to perform kinetic studies on the electrode reactions. It consequently enables the observation of the evolution of a single interface upon operation of the battery *via*

electrochemical impedance spectroscopy, providing that the interface formed at the reference electrode remains stable, which was suggested by the study of the Li|LBF|Li cell.

Another challenge is the relatively poor ionic conductivity of some fluoride solid electrolytes. The use of electrochemically stable fluoride solid electrolytes (e.g. LBF) in practical electrochemical cells implicates the employment of heightened temperatures. Therefore, a large part of this thesis was devoted to the development of a simple cell that would provide hermetical sealing over long periods of time at increased temperature. We saw that a coin-cell covered with the appropriate epoxy resin yielded a hermetical cell that could be used at 150 °C, outside the glovebox. The setup allowed probing the electrochemical reactions taking place at an electrode composed of a mixture of Bi, BiF_3, LBF and carbon. The electrochemical results obtained on a symmetrical cell relying on the BiF_3/Bi redox couple were very encouraging, as almost no capacity ($\approx$ 190 mAh/g of BiF_3) fading was observed for 3 cycles (charge/discharge rate $\approx$ 4.5 µA/cm²), even though the composition and preparation of the Bi-BiF_3 composite was not optimized. While the capacities obtained on such system are below the theoretical values (302 mAh/g for BiF_3), steps taken towards the optimization on the electrode should substantially improve their performance.

Several areas of improvement are available to optimize the electrochemical performance of the composite electrodes. The adjustment of the proportion of each component of the composite, as well as the control of their microstructure, is an important factor to take into account. For instance, the increase of the particle size of LBF would lead to an increase of the fluoride conductivity. Indeed, the nanostructuration of LBF is not beneficial as the conductivity is faster in the bulk of the crystal than at the grain boundaries. Inversely, the reduction in size of the active material, down to the nanoscale, would allow a more thorough conversion process and faster reaction kinetics, resulting in an increased capacity and the use of higher charge/discharge rates. The use of ball-milling in appropriate conditions would lead to a more intimate mixing of the components of the electrode composite. This would consequently increase the capacity of the electrode as the presence of isolated particles of electroactive species not available for conversion would be reduced. Then, the partial replacement of carbon black with nanotubes is another route to explore for improving the mechanical strength of the composite and perhaps better accommodate the volumetric variations of the active materials during their fluorination/defluorination. Finally, more elaborate methods of preparation, such as spark plasma sintering of the whole cell stack, are promising routes to enhance the performance of FIBs.

X-ray synchrotron radiation associated with diffraction and atomic pair distribution function (PDF) analyses proved to be powerful techniques to probe the conversion reactions taking place in FIBs. Even though the study was rendered difficult by the presence of large amounts of electrolyte in the composite electrodes, results obtained on a Bi-BiF$_3$ symmetrical cell allowed a quantitative analysis of the phases present after cycling of the electrode. The results suggest that a conversion mechanism involving both fluoride and oxygen ions is involved. These results open a new path for the investigation of oxyfluorides as active materials for FIBs.

References

[1] F. Badway, F. Cosandey, N. Pereira, and G. G. Amatucci, Carbon Metal Fluoride Nanocomposites, *J. Electrochem. Soc.*, vol. 150, no. 10, pp. A1318–A1327, 2003.

[2] F. Gschwind, G. Rodriguez-Garcia, D. J. S. Sandbeck, A. Gross, M. Weil, M. Fichtner, and N. Hörmann, Fluoride ion batteries: Theoretical performance, safety, toxicity, and a combinatorial screening of new electrodes, *J. Fluor. Chem.*, vol. 182, pp. 76–90, 2016.

[3] N. Nitta, F. Wu, J. T. Lee, and G. Yushin, Li-ion battery materials: Present and future, *Mater. Today*, vol. 18, no. 5, pp. 252–264, 2015.

[4] G. Girishkumar, B. McCloskey, A. C. Luntz, S. Swanson, and W. Wilcke, Lithium-air battery: Promise and challenges, *J. Phys. Chem. Lett.*, vol. 1, no. 14, pp. 2193–2203, 2010.

[5] A. J. Valerga, R. B. Badachhape, G. D. Parks, P. Karmachik, J. L. Wood, and J. L. Margrave, Thermodynamic and kinetic data of carbon-fluorine compounds, Report Rice University, Houston, 1974.

[6] H. Gamsjäger, Chemical Thermodynamics of Tin, in *Chemical Thermodynamics*, Paris: OECD Publishing, 2012, p. 646.

[7] J. Schoonman, K. E. D. Wapenaar, G. Oversluizen, and G. J. Dirksen, Fluoride-Conducting Solid Electrolytes in Galvanic Cells, *J. Electrochem. Soc.*, vol. 126, pp. 709–713, 1979.

[8] P. Poizot, S. Laruelle, S. Grugeon, L. Dupont, and J.-M. Tarascon, Nano-sized transition-metal oxides as negative-electrode materials for lithium-ion batteries, *Nature*, vol. 407, no. 6803, pp. 496–499, 2000.

[9] G. G. Amatucci and N. Pereira, Fluoride based electrode materials for advanced energy storage devices, *J. Fluor. Chem.*, vol. 128, no. 4, pp. 243–262, 2007.

[10] K. M. Wiaderek, O. J. Borkiewicz, E. Castillo-Martínez, R. Robert, N. Pereira, G. G. Amatucci, C. P. Grey, P. J. Chupas, and K. W. Chapman, Comprehensive Insights into the Structural and Chemical Changes in Mixed-Anion FeOF Electrodes by Using Operando PDF and NMR Spectroscopy, *J. Am. Chem. Soc.*, vol. 135, no. 10, pp. 4070–4078, 2013.

[11] M. Armand and J.-M. Tarascon, Building better batteries, *Nature*, vol. 451, no. 7179, pp. 652–657, 2008.

[12] K. Rui, Z. Wen, Y. Lu, J. Jin, and C. Shen, One-Step Solvothermal Synthesis of Nanostructured Manganese Fluoride as an Anode for Rechargeable Lithium-Ion Batteries and Insights into the Conversion Mechanism, *Adv. Energy Mater.*, vol. 5, no. 7, n° 1401, 2015.

[13] F. Wang, R. Robert, N. A. Chernova, N. Pereira, F. Omenya, F. Badway, X. Hua, M. Ruotolo, R. Zhang, L. Wu, V. Volkov, D. Su, B. Key, M. Stanley Whittingham, C. P. Grey, G. G. Amatucci, Y. Zhu, and J. Graetz, Conversion reaction mechanisms in lithium ion batteries: Study of the binary metal fluoride electrodes, *J. Am. Chem. Soc.*, vol. 133, no. 46, pp. 18828–18836, 2011.

[14] M. Anji Reddy and M. Fichtner, Batteries based on fluoride shuttle, *J. Mater. Chem*, vol. 21, no. 43, pp. 17059–17062, 2011.

[15] I. Kovalenko, B. Zdyrko, A. Magasinski, B. Hertzberg, Z. Milicev, R. Burtovyy, I. Luzinov, and G. Yushin, A Major Constituent of Brown Algae for Use in High-Capacity Li-Ion Batteries, *Science (80-.).*, vol. 334, no. 6052, pp. 75–79, 2011.

[16] A. S. Arico, P. G. Bruce, B. Scrosati, J.-M. Tarascon, and W. Van Schalkwijk, Nanostructured materials for advanced energy conversion and storage devices, *Nat. Mater.*, vol. 4, pp. 366–377, 2005.

[17] S. H. Ng, J. Wang, D. Wexler, K. Konstantinov, Z. P. Guo, and H. K. Liu, Highly reversible lithium storage in spheroidal carbon-coated silicon nanocomposites as anodes for lithium-ion batteries, *Angew. Chemie - Int. Ed.*, vol. 45, no. 41, pp. 6896–6899, 2006.

[18] C. K. Chan, H. L. Peng, G. Liu, K. McIlwrath, X. F. Zhang, R. A. Huggins, and Y. Cui, High-performance lithium battery anodes using silicon nanowires, *Nat. Nanotechnol.*, vol. 3, no. 1, pp. 31–35, 2008.

[19] W. Baukal, Electrochemical secondary cells which contains only solid materials, Patent CA 953780 A1, 1974.

[20] J. H. Kennedy, R. Miles, and J. Hunter, Solid Electrolyte Properties and Crystal Forms of Lead Fluoride, *J. Electrochem. Soc.*, vol. 120, no. 11, pp. 1441–1446, 1973.

[21] J. H. Kennedy and R. C. Miles, Ionic Conductivity of Doped Beta-Lead Fluoride, *J. Electrochem. Soc.*, vol. 123, no. 1, pp. 47–57, 1976.

[22] J. H. Kennedy and J. C. Hunter, Thin-Film Galvanic Cell Pb/PbF2/PbF2,CuF2/Cu, *J. Electrochem. Soc.*, vol. 123, no. 1, pp. 10–14, 1976.

[23] J. Schoonman, A Solid-State Galvanic Cell with Fluoride-Conducting Electrolytes, *J. Electrochem. Soc.*, vol. 123, no. 12, pp. 1772–1775, 1976.

[24] W. Borger, U. Hullmeine, and E. Voss, Galvanic cell with solid fluoride ion-conductive electrolyte, Patent US 3973990 A1, 1976.

[25] Y. Danto, G. Poujade, J. D. Pistre, C. Lucat, and J. Salardenne, A Pb/PbF2/BiF3/Bi thin solid film reversible galvanic cell, *Thin Solid Films*, vol. 55, no. 3, pp. 347–354, 1978.

[26] W. Puin, S. Rodewald, R. Ramlau, P. Heitjans, and J. Maier, Local and overall ionic conductivity in nanocrystalline CaF2, *Solid State Ionics*, vol. 131, no. 1, pp. 159–164, 2000.

[27] J. Schoonman and A. Wolfert, Alloy-Anodes in Fluoride Solid-State Batteries, *J. Electrochem. Soc.*, vol. 128, no. 7, pp. 1522–1523, 1981.

[28] J. Schoonman and A. Wolfert, Solid-state galvanic cells with fast fluoride conducting electrolytes, *Solid State Ionics*, vol. 3–4, pp. 373–379, 1981.

[29] C. Rongeat, M. Anji Reddy, T. Diemant, R. J. Behm, and M. Fichtner, Development of new anode composite materials for fluoride ion batteries, *J. Mater. Chem. A*, vol. 2, no. 48, pp. 20861–20872, 2014.

[30] A. A. Potanin, Solid-State secondary power supply, Patent US 20080102373 A1, 2008.

[31] I. Darolles, C. Weiss, M. Alam, A. Tiruvannnamalai, and S. C. Jones, Fluoride Ion Battery Composition, Patent US 20120164541 A1, 2012.

[32] F. Gschwind, Z. Zhao-Karger, and M. Fichtner, Fluoride-doped PEG matrix as an electrolyte for anion transportation in a room-temperature fluoride ion battery, *J. Mater. Chem. A*, vol. 2, no. 5, pp. 1214–1218, 2014.

[33] C. Rongeat, M. Anji Reddy, R. Witter, and M. Fichtner, Nanostructured Fluorite-Type Fluorides As Electrolytes for Fluoride Ion Batteries, *J. Phys. Chem. C*, vol. 117, pp. 4943–4950, 2013.

[34] C. Rongeat, M. Anji Reddy, R. Witter, and M. Fichtner, Solid Electrolytes for Fluoride Ion Batteries: Ionic Conductivity in Polycrystalline Tysonite-Type Fluorides, *ACS Appl. Mater. Interfaces*, vol. 6, no. 3, pp. 2103–2110, Feb. 2014.

[35] L. N. Patro and K. Hariharan, Fast fluoride ion conducting materials in solid state ionics: An overview, *Solid State Ionics*, vol. 239, pp. 41–49, 2013.

[36] V. Trnovcová, P. P. Fedorov, I. I. Buchinskaya, V. Šmatko, and F. Hanic, Fast ionic conductivity of PbF2:MF2 (M = Mg, Ba, Cd) and PbF2:ScF3 single crystals and composites, *Solid State Ionics*, vol. 119, no. 1, pp. 181–189, 1999.

[37] A. Roos and J. Schoonman, Electronic conductivity in La1−xBaxF3−x crystals, *Solid State Ionics*, vol. 13, no. 3, pp. 205–211, 1984.

[38] P. G. Bruce, A. R. West, J. B. Goodenough, J. L. Souquet, D. F. Shriver, F. M. Gray, W.

R. McKinnon, W. Weppner, B. Scrosati, R. D. Armstrong, M. Todd, and O. Yamamoto, *Solid State Electrochemistry*. Cambridge: Cambridge University Press, 1997.

[39] P. J. Mohr and B. N. Taylor, CODATA Recommended Values of the Fundamental Physical Constants: 1998, Fundamental Physical Constants — Complete Listing, *J. Phys. Chem. Ref. Data*, vol. 28, no. 6, pp. 1–7, 1999.

[40] J. Schoonman, G. Oversluizen, and K. E. D. Wapenaar, Solid electrolyte properties of LaF3, *Solid State Ionics*, vol. 1, no. 3, pp. 211–221, 1980.

[41] J. Chable, B. Dieudonné, M. Body, C. Legein, M.-P. Crosnier-Lopez, C. Galven, F. Mauvy, E. Durand, S. Fourcade, D. Sheptyakov, M. Leblanc, V. Maisonneuve, and A. Demourgues, Fluoride solid electrolytes: investigation of the tysonite-type solid solutions La1−xBaxF3−x (x < 0.15), *Dalt. Trans.*, vol. 44, no. 45, pp. 19625–19635, 2015.

[42] N. I. Sorokin and B. P. Sobolev, Nonstoichiometric fluorides—Solid electrolytes for electrochemical devices: A review, *Crystallogr. Reports*, vol. 52, no. 5, pp. 842–863, 2007.

[43] J. Chable, Électrolytes solides fluorés pour batteries tout solide à ions F-, thesis, Université de Bordeaux, 2015.

[44] A. Roos, A. F. Aalders, J. Schoonman, A. F. M. Arts, and H. W. de Wijn, Electrical Conduction and 19F NMR of Solid Solutions La1-xBaxF3-x, *Solid State Ionics*, vol. 9 & 10, pp. 571–574, 1983.

[45] A. Roos, F. C. M. van de Pol, R. Keim, and J. Schoonman, Ionic conductivity in tysonite-type solid solutions La1-xBaxF3-x, *Solid State Ionics*, vol. 13, no. 3, pp. 191–203, 1984.

[46] R. A. Huggins, Simple method to determine electronic and ionic components of the conductivity in mixed conductors a review, *Ionics (Kiel).*, vol. 8, no. 3–4, pp. 300–313, 2002.

[47] W. Weppner, Engineering of solid state ionic devices, *Ionics (Kiel).*, vol. 9, no. 5–6, pp. 444–464, 2003.

[48] H. L. Tuller, Ionic conduction in nanocrystalline materials, *Solid State Ionics*, vol. 131, no. 1, pp. 143–157, 2000.

[49] C. Wagner, The electrical conductivity of semi-conductors involving inclusion of another phase, *J. Phys. Chem. Solids*, vol. 33, pp. 1051–1059, 1972.

[50] J. Maier, Ionic conduction in space charge regions, *Prog. Solid State Chem.*, vol. 23, no. 3, pp. 171–263, 1995.

[51] N. Sata, K. Eberman, K. Eberl, and J. Maier, Mesoscopic fast ion conduction in nanometre-scale planar heterostructures., *Nature*, vol. 408, no. 6815, pp. 946–949, 2000.

[52] A. C. Luntz, J. Voss, and K. Reuter, Interfacial Challenges in Solid-State Li Ion Batteries, *J. Phys. Chem. Lett.*, vol. 6, no. 22, pp. 4599–4604, 2015.

[53] K. Takada, T. Inada, A. Kajiyama, H. Sasaki, S. Kondo, M. Watanabe, M. Murayama, and R. Kanno, Solid-state lithium battery with graphite anode, *Solid State Ionics*, vol. 158, no. 3–4, pp. 269–274, 2003.

[54] N. Ohta, K. Takada, L. Zhang, R. Ma, M. Osada, and T. Sasaki, Enhancement of the high-rate capability of solid-state lithium batteries by nanoscale interfacial modification, *Adv. Mater.*, vol. 18, no. 17, pp. 2226–2229, 2006.

[55] C. Julien and N. Gholam-Abbas, *Solid State Batteries: Materials Design and Optimization*. Boston: Kluwer Academic, 1994.

[56] A. Aboulaich, R. Bouchet, G. Delaizir, V. Seznec, L. Tortet, M. Morcrette, P. Rozier, J. M. Tarascon, V. Viallet, and M. Dollé, A new approach to develop safe all-inorganic monolithic li-ion batteries, *Adv. Energy Mater.*, vol. 1, no. 2, pp. 179–183, 2011.

[57] G. Delaizir, V. Viallet, A. Aboulaich, R. Bouchet, L. Tortet, V. Seznec, M. Morcrette, J. M. Tarascon, P. Rozier, and M. Dollé, The stone age revisited: Building a monolithic

inorganic lithium-ion battery, *Adv. Funct. Mater.*, vol. 22, no. 10, pp. 2140–2147, 2012.

[58] S. Larfaillou, Application de la spectroscopie d'impédance électrochimique à la caractérisation et au diagnostic de microbatteries tout solide, Thesis, Université Paris Sud, 2015.

[59] N. I. Sorokin, P. P. Fedorov, O. K. Nikol, O. A. Nikeeva, E. G. Rakov, and E. I. Ardashnikova, Electrical Properties of PbSnF4 Materials Prepared by Different Methods, *Inorg. Mater.*, vol. 37, no. 11, pp. 1378–1382, 2001.

[60] V. Thangadurai, S. Narayanan, and D. Pinzaru, Garnet-type solid-state fast Li ion conductors for Li batteries: critical review., *Chem. Soc. Rev.*, vol. 43, no. 13, pp. 4714–27, 2014.

[61] N. Kamaya, K. Homma, Y. Yamakawa, M. Hirayama, R. Kanno, M. Yonemura, T. Kamiyama, Y. Kato, S. Hama, K. Kawamoto, and A. Mitsui, A lithium superionic conductor, *Nat. Mater.*, vol. 10, no. 9, pp. 682–686, 2011.

[62] R. Kanno, S. Nakamura, K. Ohno, and Y. Kawamoto, Ionic conductivity of tetragonal PbSnF4 prepared by solid state reaction in HF atmosphere, *Mater. Res. Bull.*, vol. 26, no. 11, pp. 1111–1117, 1991.

[63] OECD, Chemical Thermodynamics of Tin – Volume 12, in *Chemical Thermodynamics*, OECD Publishing, Paris, 2012.

[64] V. N. Bezmelnitsyn, A. V. Bezmelnitsyn, and A. A. Kolmakov, New solid-state electrochemical source of pure fluorine, *J. Fluor. Chem.*, vol. 77, no. 1, pp. 9–12, 1996.

[65] Y. Zhu, X. He, and Y. Mo, Origin of Outstanding Stability in the Lithium Solid Electrolyte Materials: Insights from Thermodynamic Analyses Based on First-Principles Calculations, *ACS Appl. Mater. Interfaces*, vol. 7, no. 42, pp. 23685–23693, 2015.

[66] W. D. Richards, L. J. Miara, Y. Wang, J. C. Kim, and G. Ceder, Interface Stability in Solid-State Batteries, *Chem. Mater.*, p. acs.chemmater.5b04082, 2015.

[67] X.-B. Cheng, R. Zhang, C.-Z. Zhao, F. Wei, J.-G. Zhang, and Q. Zhang, A Review of Solid Electrolyte Interphases on Lithium Metal Anode, *Adv. Sci.*, vol. 3, no. 3, article number 1500213, 2016.

[68] J. T. S. Irvine, D. C. Sinclair, and A. R. West, Electroceramics : Characterization by Impedance Spectroscopy, *Adv. Mater.*, vol. 2, no. 3, pp. 132–138, 1990.

[69] I. D. Raistrick, C. Ho, Y. W. Hu, and R. A. Huggins, Ionic conductivity and electrode effects on β-PbF2, *J. Electroanal. Chem. Interfacial Electrochem.*, vol. 77, no. 3, pp. 319–337, 1977.

[70] J. R. Macdonald and W. R. Kenan, *Impedance spectroscopy: emphasizing solid materials and systems*, John Wiley. New York, 1987.

[71] B. Hirschorn, M. E. Orazem, B. Tribollet, V. Vivier, I. Frateur, and M. Musiani, Determination of effective capacitance and film thickness from constant-phase-element parameters, *Electrochim. Acta*, vol. 55, no. 21, pp. 6218–6227, 2010.

[72] S. Boulineau, M. Courty, J.-M. Tarascon, and V. Viallet, Mechanochemical synthesis of Li-argyrodite Li6PS5X (X=Cl, Br, I) as sulfur-based solid electrolytes for all solid state batteries application, *Solid State Ionics*, vol. 221, pp. 1–5, 2012.

[73] M. Kotobuki, K. Kanamura, Y. Sato, and T. Yoshida, Fabrication of all-solid-state lithium battery with lithium metal anode using Al2O3-added Li7La3Zr2O12 solid electrolyte, *J. Power Sources*, vol. 196, no. 18, pp. 7750–7754, 2011.

[74] J. K. Feng, L. Lu, and M. O. Lai, Lithium storage capability of lithium ion conductor Li1.5Al0.5Ge1.5(PO4)3, *J. Alloys Compd.*, vol. 501, no. 2, pp. 255–258, 2010.

[75] Y. Seino, K. Takada, B.-C. Kim, L. Zhang, N. Ohta, H. Wada, M. Osada, and T. Sasaki, Synthesis of phosphorous sulfide solid electrolyte and all-solid-state lithium batteries with graphite electrode, *Solid State Ionics*, vol. 176, no. 31–34, pp. 2389–2393, 2005.

[76] J. Jamnik and J. Maier, Nanocrystallinity effects in lithium battery materials - Aspects

of nano-ionics. Part IV, *Phys. Chem. Chem. Phys.*, vol. 5, no. 23, pp. 5215–5220, 2003.

[77]   A. Glassner, The thermochemical properties of the oxides, fluorides, and chlorides to 2500° K, report ANL-5750, Argonne National Laboratory, Lemont, 1957.

[78]   A. Jain, S. P. Ong, G. Hautier, W. Chen, W. D. Richards, S. Dacek, S. Cholia, D. Gunter, D. Skinner, G. Ceder, and K. A. Persson, Commentary: The materials project: A materials genome approach to accelerating materials innovation, *APL Mater.*, vol. 1, no. 1, article numer 011002, 2013.

[79]   K. A. Seid, J. C. Badot, C. Perca, O. Dubrunfaut, P. Soudan, D. Guyomard, and B. Lestriez, An in situ multiscale study of ion and electron motion in a lithium-ion battery composite electrode, *Adv. Energy Mater.*, vol. 5, no. 2, pp. 1–10, 2015.

[80]   F. Han, Y. Zhu, X. He, Y. Mo, and C. Wang, Electrochemical Stability of Li10GeP2S12 and Li7La3Zr2O12 Solid Electrolytes, *Adv. Energy Mater.*, p. 1501590, 2016.

[81]   T. Nakajima and N. Watanabe, *Graphite fluorides and carbon-fluorine compounds*. Boca Raton: CRC Press, 1991.

[82]   A. A. Potanin, Chemical current source, Patent US 20120148906A1, 2012.

[83]   D. Muñoz-Rojas, J.-B. Leriche, C. Delacourt, P. Poizot, M. R. Palacín, and J.-M. Tarascon, Development and implementation of a high temperature electrochemical cell for lithium batteries, *Electrochem. commun.*, vol. 9, pp. 708–712, 2007.

[84]   C. Lucat, Etude des propriétés de conductivité ionique de quelques fluorures de structure fluorine, Thesis, Université de Bordeaux I, 1976.

[85]   J. Cabana, L. Monconduit, D. Larcher, and M. R. Palacín, Beyond intercalation-based Li-ion batteries: The state of the art and challenges of electrode materials reacting through conversion reactions, *Adv. Mater.*, vol. 22, no. 35, pp. 170–192, 2010.

[86]   Y.-Y. Hu, Z. Liu, K.-W. Nam, O. J. Borkiewicz, J. Cheng, X. Hua, M. T. Dunstan, X. Yu, K. M. Wiaderek, L.-S. Du, K. W. Chapman, P. J. Chupas, X.-Q. Yang, and C. P. Grey, Origin of additional capacities in metal oxide lithium-ion battery electrodes., *Nat. Mater.*, vol. 12, no. 12, pp. 1130–6, 2013.

[87]   X. Hua, R. Robert, L.-S. Du, K. M. Wiaderek, M. Leskes, K. W. Chapman, P. J. Chupas, and C. P. Grey, Comprehensive Study of the CuF2 Conversion Reaction Mechanism in a Lithium Ion Battery, *J. Phys. Chem. C*, vol. 118, no. 28, pp. 15169–15184, 2014.

[88]   B. Shyam, K. W. Chapman, M. Balasubramanian, R. J. Klingler, G. Srajer, and P. J. Chupas, Structural and mechanistic revelations on an iron conversion reaction from pair distribution function analysis, *Angew. Chemie - Int. Ed.*, vol. 51, no. 20, pp. 4852–4855, 2012.

[89]   X. Qiu, J. W. Thompson, and S. J. L. Billinge, PDFgetX2: a GUI-driven program to obtain the pair distribution function from X-ray powder diffraction data, *J. Appl. Crystallogr.*, vol. 37, no. 4, p. 678, Aug. 2004.

[90]   C. L. Farrow, P. Juhas, J. W. Liu, D. Bryndin, E. S. Božin, J. Bloch, T. Proffen, and S. J. L. Billinge, PDFfit2 and PDFgui: computer programs for studying nanostructure in crystals., *J. Phys. Condens. Matter*, vol. 19, no. 33, article number 335219, 2007.

[91]   J. P. Laval, Bi (F , O) 2 . 45 : An Anion-Excess Fluorite Defect Structure Deriving from Rhombohedral LnFO Type, *J. Solid State Chem.*, vol. 59, pp. 51–59, 1999.

[92]   M. Bervas, L. C. Klein, and G. G. Amatucci, Reversible Conversion Reactions with Lithium in Bismuth Oxyfluoride Nanocomposites, *J. Electrochem. Soc.*, vol. 153, no. 1, pp. A159–A170, 2006.

[93]   P. Hagenmuller, *Inorganic Solid Fluorides: Chemistry And Physics*. New York: Academic Press, 1985.

[94]   A. Tressaud, *Functionalized Inorganic Fluorides: synthesis, characterization and properties of nanostructured solids*. Chippenham: Wiley, 2010.

[95]   M. Ando, M. Enoki, H. Nishiguchi, T. Ishihara, and Y. Takita, Oxide ion conductivity

and chemical stability of lanthanum fluorides doped with oxygen, La(Sr,Na)F3-2xOx, *Chem. Mater.*, vol. 16, no. 21, pp. 4109–4115, 2004.

[96] A. Rhandour, J. M. Reau, S. Matar, and P. Hagenmuller, Effect of oxygen on the crystallographic and electric properties of fluocerite-type materials, *J. Solid State Chem.*, vol. 64, no. 2, pp. 206–216, 1986.

[97] T. Egami and S. J. L. Billinge, *Underneath the Bragg Peaks*, Pergamon., vol. 6, no. 6. Amsterdam: Elsevier B.V, 2003.

[98] P. K. Allan, J. M. Griffin, A. Darwiche, O. J. Borkiewicz, K. M. Wiaderek, K. W. Chapman, A. J. Morris, P. J. Chupas, L. Monconduit, and C. P. Grey, Tracking Sodium-Antimonide Phase Transformations in Sodium-Ion Anodes: Insights from Operando Pair Distribution Function Analysis and Solid-State NMR Spectroscopy, *J. Am. Chem. Soc.*, p. jacs.5b13273, 2016.

[99] D. Dambournet, K. W. Chapman, P. J. Chupas, R. E. Gerald, II, N. Penin, C. Labrugere, A. Demourgues, A. Tressaud, and K. Amine, Dual Lithium Insertion and Conversion Mechanisms in a Titanium-based Mixed Anion Nanocomposite Dual Lithium Insertion and Conversion Mechanisms in a Titanium-based Mixed Anion Nanocomposite, *J. Am. Chem. Soc.*, vol. 133, no. 34, pp. 13240–13243, 2011.

[100] T. Proffen and S. J. L. Billinge, PDFFIT, a program for full profile structural refinement of the atomic pair distribution function, *J. Appl. Crystallogr.*, vol. 32, no. 3, pp. 572–575, 1999.

Appendix

1. Introduction to X-ray diffraction (XRD) and atomic pair distribution function (PDF) analysis

XRD is a well-established technique used to characterize the structure of crystalline compounds. In order to efficiently discuss PDF analysis, a small introduction to conventional XRD is proposed here.

1.1. Conventional XRD

The periodic disposition of atoms in a crystal forms planes. The planes are separated by specific distances (d-spacings) along defined directions in the crystal lattice. The distances separating the atomic planes can be investigated using the scattering properties of quantic particles such as electrons, neutrons, and photons. X-rays are particularly employed as their wavelength are in the same order of magnitude that the distances separating atoms (ångströms, Å).

When an incoming X-ray beam collides with an array of planes of the crystal structure, X-rays interact with the atoms present in the planes, and emit back X-rays (i.e. elastic scattering). When the scattered X-rays add constructively, they form a pattern (spots) that can be detected and recorded as a 2D image by the X-ray detector (image plate). This pattern is called a diffraction pattern.

The angle at which the X-rays scatter is function of the X-ray wavelength (energy) and d-spacing, according to Bragg's law:

$$2d \sin \theta = n\lambda \qquad\qquad 60.$$

With d the d-spacing, θ and λ the incident angle and wavelength of the X-rays, and n an integer. By varying θ and measuring the intensity of the diffracted X-rays, it is possible to obtain the diffraction pattern (2θ in function of the intensity) of the crystal or crystalline powder.

Conventional powder X-ray experiments are generally carried out using copper excitation sources by bombarding a copper target with electrons. The X-rays are then filtered by a monochromator so that a single wavelength is obtained ($\lambda_{CuK\alpha}$ = 1.5418 Å).

1.2. Hard and high-energy X-rays

High-energy X-rays (HEX-rays), are very hard X-rays with typical energies ranging from 80 to 1000 keV, more than one order of magnitude higher than conventional X-rays (about 8 keV). Hard X-rays are generally considered for energies about 10 keV, but there is no general consensus on these denominations. The energy E of the X-ray photon is linked to its wavelength λ by the Planck-Einstein relation:

$$E = \frac{hc}{\lambda} \qquad\qquad 61.$$

With h the Planck's constant (h = $6.62607004 \times 10^{-34}$ m^2.kg.s^{-1}) and c the speed of light in vacuum (299,792,458 m.s^{-1}).

HEX-rays can be obtained from synchrotron radiation facilities. In a synchrotron, high-energy particles such as high energy electrons (energies in the order of GeV) are accelerated with electromagnets in the storage ring, a large tubular structure that can reach a circumference of more than 1 km. When the high-energy particles are forced to travel in a curved path, synchrotron radiation is emitted tangent to their circular path. The emitted light is then gathered in so-called beam-lines, where they can be used for various characterization techniques, including XRD and PDF.

The use of HEX-rays can be advantageous in many ways (high penetration into materials, negligible polarization etc.) In our case specifically, the advantage relies in their use in both XRD and PDF analyses.

First, using HEX-rays for XRD (HEXRD) is useful as very high 2θ resolution and/or 2θ values can be achieved, yielding little background noise and very clean patterns. This is particularly interesting when investigating nanosized materials as the intensity of diffraction peaks depends on the crystallinity of the phase (i.e. low crystallinity yields low intensity). The absence of significant background noise and the high 2θ resolution makes it possible to see even low intensity peaks. These peaks would normally be hidden by the background in a conventional XRD experiment, but can be clearly visible in HEXRD.

Secondly, and more importantly, HEX-rays provide optimal data for use in PDF analysis as the high magnitude of scattering vector $|Q|$ provides high values of momentum transfer Q (amount of momentum that a particle gives to another particle).

$$|Q| = Q = \frac{4\pi \sin\theta}{\lambda} \qquad\qquad 62.$$

A higher energy yields smaller λ and thus larger Q. The effect of Q on the PDF is discussed in the next section.

1.3. What is PDF analysis

The Pair Distribution Function, or PDF in short, also noted $G(r)$, is a real space function giving the probability of finding pairs of atoms separated by the distance r, in the material[97]. It is a powerful technique capable to probe both the local (low r) and intermediate (high r) range structure of materials. Unlike Bragg scattering which only gives information about the average structure, PDF analysis is able to shed light on the local structure of amorphous materials (glasses and even liquids) and highly disordered crystalline materials (nanomaterials), which is very useful when investigating electrochemical processes happening in electrode materials[10], [98], [99]. Indeed, electrochemical conversion tends to create disordered nano-domains which can be hardly detected by conventional XRD. For instance, in Li batteries using conversion materials, the metal fluoride MF_x electrode is converted to nano-domains (a few nm wide) of the corresponding metal M, embedded in a LiF matrix. These reactions cannot be probed by conventional diffraction techniques, unlike with PDF analysis. Indeed, PDF takes benefit of the information contained in the diffuse intensity which contains information about the discrepancies in the local structure of the analysed material.

From a conceptual point of view, $G(r)$ can be expressed in function of the atom-pair density function (or microscopic pair density), $\rho(r)$, and the atomic number density (or average number density), ρ_0, as follow:

$$G(r) = 4\pi r[\rho(r) - \rho_0] = 4\pi r \rho_0[g(r) - 1] \qquad 63.$$

With $g(r)$ the atomic pair distribution function. **Consequently, the amplitude of $G(r)$ will be thus dependent upon the mass number of the considered atoms, their density (i.e. quantity), and the probability of finding them separated by the distance r.**

The PDF obtained can be expressed as follow:

$$G(r) = \frac{2}{\pi} \int_0^\infty F(Q) \sin(Qr) dQ \qquad 64.$$

With $F(Q)$ the reduced structure function, which can be expressed in function of the total scattering is the normalized structure function $S(Q)$:

$$F(Q) = Q[S(Q) - 1] \qquad 65.$$

In practice, only finite Q values can be reached. The PDF is therefore obtained by a sine Fourier transform of the total scattering structure function with limited Q boundaries:

$$G(r) = \frac{2}{\pi} \int_{Q_{min}}^{Q_{max}} Q[S(Q) - 1] \sin(Qr) dQ \qquad \qquad 66.$$

$S(Q)$ is obtained from experimental diffraction intensity $I(Q)$ after application of corrections accounting for sample and instrument contributions. High Q_{max} thus yields better resolution in PDF analysis. In order to illustrate what a PDF looks like and the influence of Q on the resolution of the PDF, **Figure 0.1** shows the PDF of LBF with various Q values.
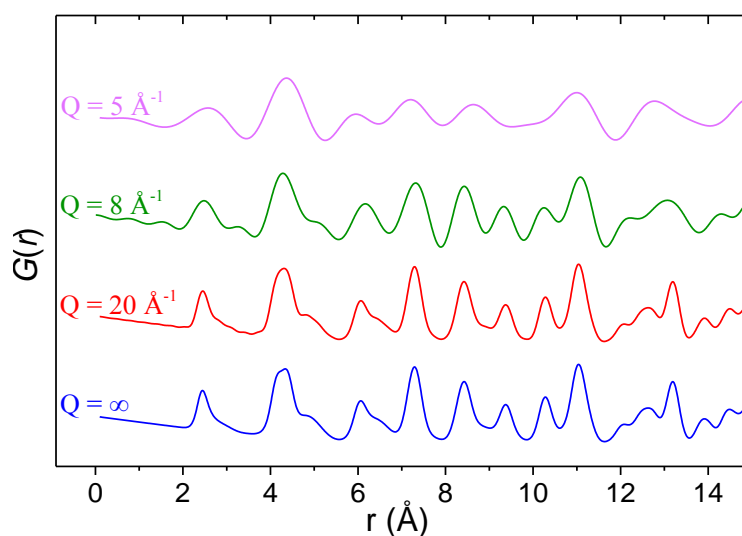
Figure 0.1. *PDF of La$_{0.95}$Ba$_{0.05}$F$_{2.95}$ calculated for different Q values.*

Using conventional X-rays sources like $\lambda_{CuK\alpha} = 1.5418$ Å, and considering that $\sin\theta \leq 1$, $Q \leq 4\pi/\theta$ and thus $Q \leq 8$ Å^{-1}. **Figure 0.2** illustrates well that the amplitude of $G(r)$ is dependent upon the mass number of the relevant atom.
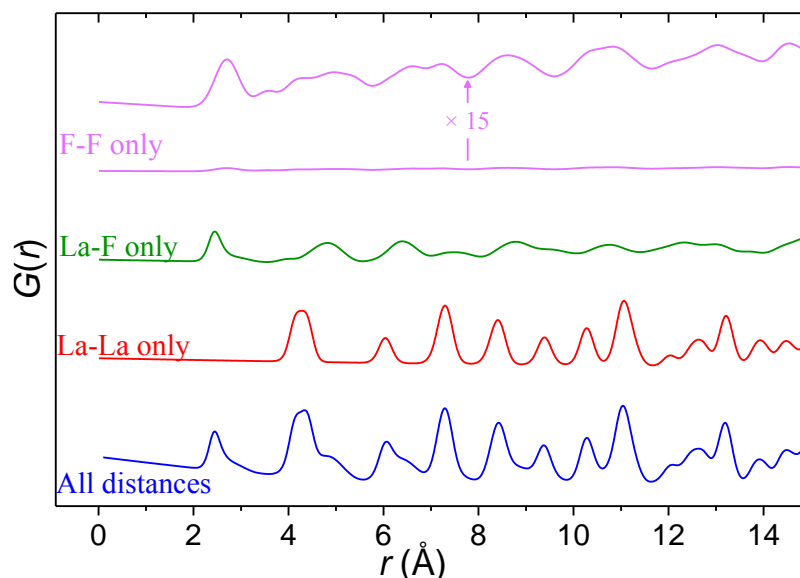
Figure 0.2. *PDF of La$_{0.95}$Ba$_{0.05}$F$_{2.95}$ and the corresponding reduced PDF of the La-La, La-F and F-F distances (Q = ∞). The G(r) amplitude for the F-F distances was multiplied by 15 to illustrate the low intensity of the F-F reduced PDF.*

Even if the ratio F/La is around 3 in LBF, the amplitude of the F-F contribution to the PDF is almost not visible when compared to that of the La-La and La-F contributions, due to the large mass of La (138.9 u) compared to that of F (19.0 u).

1.3.1. PDF analysis and HEXRD in practice

Hard X-rays were collected at the 11-ID-B beamline of the Advanced Photon Source of Argonne National Laboratory, USA. The powdered samples were sealed in Kapton capillaries (Cole-Parmer®, polyimide tubing, 0.0435" outside diameter, 0.0020" wall) under argon atsmosphere, using epoxy glue.

The PDF analysis results used total scattering data recorded at 58.66 or 86.7 keV, i.e., 0.21140 and 0.1430 Å, with sample to detector distances of 175 and 245 mm, respectively. Such sample to detector distance was employed to obtain high Q-range. The data were recorded using an amorphous silicon-based area detector (PerkinElmer).

Diffraction data were simultaneously recorded with a sample to detector distance of about 945 mm to optimize them for 2θ resolution. The *I(Q)* data (intensity presented in Q space) could be conveniently converted to *I(2θ)* classical CuKα XRD data using the relation:

$$Q = \frac{4\pi \sin\theta}{\lambda} \qquad \rightarrow \qquad 2\theta = 2\arcsin\frac{Q\lambda}{4\pi} \qquad\qquad 67.$$

Such diffraction patterns are captioned as HEXRD patterns.

1.3.1.1. Conversion of total scattering data to the PDF

Total scattering data (.chi files) were converted to the PDF using PDFgetX2 software[89]. Various S(Q) optimization/corrections were applied to the total scattering data to obtain quality PDFs. Most of these corrections can be found on the annotated demo (https://www.youtube.com/watch?v=9qarGvEYTvQ) of PDFgetX2 provided by Karena Chapman of the Advanced Photon Source. Many useful videos relevant to PDF analysis, including an introduction to PDFgui (software for the refinement of PDF data), can be found on her youtube channel.

First, the background (empty capillary) contribution was corrected. For the samples containing LBF, some fluorescence coming from LaF$_3$ (K-edge = 39 keV) could be observed, particularly when data were recorded at 58.66 keV. Recording at 86.7 keV helped but did not entirely solve the problem. To palliate this, a large constant ("Add Sam. Bkg") was added to the kapton background contribution. Using the fluorescence S(Q) correction with a constant of the same value provided similar results.

To adequately account for Compton (inelastic) scattering, which is a crucial correction, the weight ratios of each atom present in the analyzed powder was calculated and entered in the sample information page. When discharged products were analyzed, a rough estimation of the ratios was calculated. The intensity of the relative phases observed on the HEXRD patterns helped doing so. A 1/E quadratic energy dependence (a & b factors) was employed to efficiently correct Compton scattering.

Laue diffuse scattering was also accounted. A weighting function type "<asf>^2" was used. Oblique incidence was corrected using a transmission coefficient of 0.2 unless significant deviation at high-Q was observed (i.e. increasing intensity at high-Q). A superior value, up to 0.4 was then used, although the correction did not significantly modify the G(r) yielded.

1.3.1.2. PDF analysis, refinement of the PDF

The refinement of the PDF was performed using PDFgui[90], a graphical user interface (GUI) based on the PDFfit2[100] software used for the full-profile fitting of PDF data by least square refinement.

In a typical fit, PDF data obtained from PDFgetX2 (.gr files) are refined using one or multiple phases. Each phase contains a set of parameters (lattice parameters and angles, atoms etc.) that can be constrained for refinement. In all of the PDF refinements exhibited in this manuscript, the following phase parameters were constrained:

- Lattice parameters *a, b, c,* with a same constraint for similar values (e.g. a single constraint for cubic systems)
- *scale factor* (related to the ratio of the concerned phase and scale of the PDF data)
- *delta2* (quadratic atom correlation factor, peak sharpening),
- *sratio* (low *r* peak sharpening), only if delta2 is not employed, with a *rcut* fixed right after the 1st interatomic distance
- *spdiameter* (crystallite size), only if relevant,
- isotropic atomic displacement factors (ADPs) *u11, u22, u33*, with an identical constraint for similar atoms (e.g. same constraint for all La atoms, another for all F atoms, etc.)

For more details about the parameters, please refer to the PDFgui manual/user guide (http://www.diffpy.org/doc/pdfgui/pdfgui.pdf).

Unacceptably high ADPs (> 0.04) were usually due to low scale factors (< 0.02), generally meaning that the weight ratio of the concerned phase was below 1 %. In this case, a value of 0.008 was fixed for cations and 0.01 for anions and no further refinement on ADPs was performed until the scale factor was sufficiently high.

For multiphased refinements, the lattice parameters were carefully refined. Once again, when the weight ratio of the concerned phased was very low, refinement of the lattice parameters usually lead to unlikely values. For instance, a refined value of 6.60 Å for a starting value of 5.56 Å was deemed unacceptable, especially when no significant 2θ deviation was observed on the XRD patterns. When deviation was deemed too large, the lattice parameters were fixed to values taken from literature or from a previous single-phase refinement that yielded reproducible values.

The data s*et al*so contains some parameters than can be refined, especially the *Q* dampening factor (Q_{damp}). Its value depends on the instrument (*Q* resolution) and is characterized by a loss of amplitude of *G(r)* at high *r*. In our case, refinement leads to values of 0.04 to 0.05. The value of Q_{damp} was set to 0.045 for all refinements for comparative purposes.

The quality of the refinement is characterized by the weighted R-value noted R_w. The R-value describes the difference between the experimental observation (data) and the calculated value (fit) for a single data point. The R_w is the R-value weighted for data points *i*, and is given by the formula:

$$R_w = \sqrt{\frac{\sum_{i=1}^{N} w(r_i)[G_{obs}(r_i) - G_{calc}(r_i)]^2}{\sum_{i=1}^{N} w(r_i)G_{obs}^2(r_i)}}$$

<div align="right">68.</div>

With G_{obs} and G_{calc} the observed (data) and calculated (fit) PDF and $w(r_i)$ the weight for each data point.

The R_w value under which the refinement can be considered good is subjective and dependant on the number of phase entering in consideration, but we can consider that values $R_w > 0.2$ indicate a bad refinement. For a single phase, well crystallized material with little defects, a R_w < 0.1 can even be expected. For a multiphased, nanocrystalline material, R_w < 0.1 are almost impossible to reach.

In general, $0.10 < R_w < 0.15$ suggest that the phase(s) considered are in good agreement with the observed PDF and that the refinement is sufficiently good.

It is worth noticing that PDFgui also gives the difference curve between the observed and calculated curves. A specific pattern in the difference curve can be revealing of an additional phase present in the material and careful consideration should be brought upon it.

Finally, it is crucial to remember that both XRD and PDF analysis are complementary. Determining by XRD the crystalline phases present in the material before carrying out PDF analysis is a necessity. Inversely, characterizing nanocrystalline/amorphized materials, or phases present in small amounts, will be impossible without PDF analysis.

$$R_w = \sqrt{\frac{\sum_{i=1}^{N} w(r_i)[G_{obs}(r_i) - G_{calc}(r_i)]^2}{\sum_{i=1}^{N} w(r_i)G_{obs}^2(r_i)}}$$

2. Characterization by electrochemical impedance spectroscopy

The term impedance refers to the frequency dependent resistance to current flow of a circuit element (capacitor, inductor and so on.)

Electrochemical Impedance Spectroscopy (EIS), sometimes referred as dielectric spectroscopy, is a powerful technique to probe the physical properties (e.g. electrical conductivity, formation of surface layers) of materials and the chemical processes (e.g. charge transfer, diffusion) that take place in electrochemical cells.

Consequently, the use of EIS is unavoidable in the modern study of solid-state systems as it provides a fast and reliable way to determine the conductivity of solid electrolytes[68]. It is also of crucial importance for the observation of the appearance and evolution of interface phenomena, such as the formation of solid electrolyte interface (SEI) taking place at the interface between the electrolyte and the electrode.

2.1. Principle

EIS can be considered as a non-destructive characterization technique as it does not significantly modify the electrochemical system (for experiments under open circuit conditions), unlike typical DC methods like voltammetry. Indeed, only a small amplitude perturbation in potential V_a (Potentiostatic EIS) or current I_a (Galvanostatic EIS) is applied to the cell. Considering that electrochemical systems generally present no linearity (i.e. linearity of the current-potential curve respecting Ohm's law), the use of small amplitude perturbations allows for the cell to locally achieve pseudo linearity.

In PEIS, the perturbation is typically of only few millivolts but can be increased for high impedance systems, as it is typically the case with solid-state cells, as long as pseudo linearity is conserved (**Figure 0.3**).
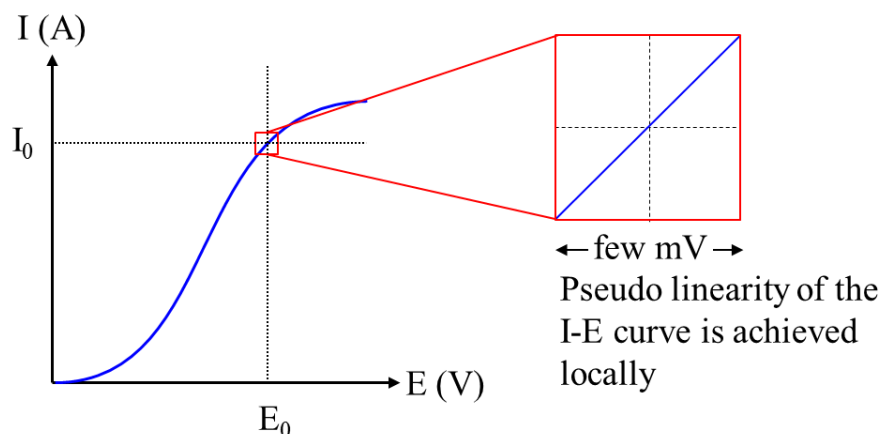
Figure 0.3. *Typical non linearity of a schematic I-E curve observed in electrochemical cells. The pseudo linearity is achieved locally as only a few millivolts excitation is applied to the cell.*

The sinusoidal excitation of amplitude V_a is applied at a fixed potential value E_0 and its current response I is measured, yielding a sinusoidal response I_a (**Figure 0.4**).
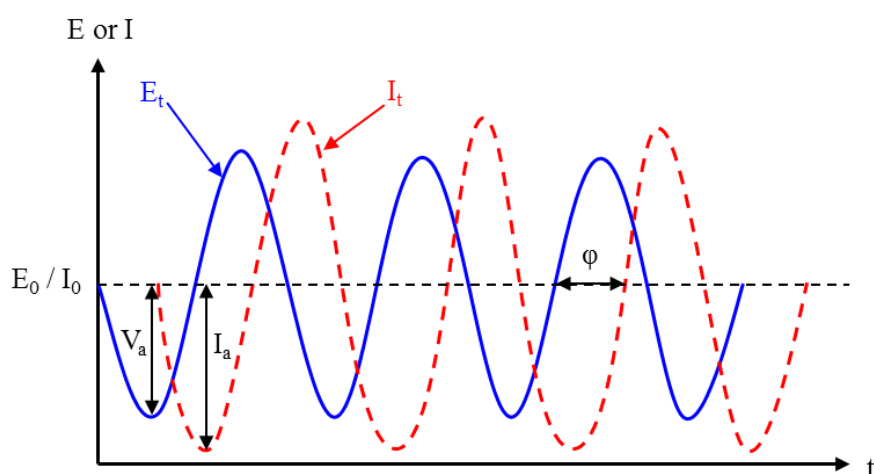
Figure 0.4. *Illustration of the phase-shift in the sinusoidal current response observed for a linear system.*

The current response can present a phase shift φ with the potential perturbation. The impedance Z of the system is given by the ratio of the potential perturbation on the current response:

$$Z = \frac{E}{I} = \frac{E_0 + V_a \sin(\omega t)}{I_0 + I_a \sin(\omega t + \varphi)} = Z_0 \frac{\sin(\omega t)}{\sin(\omega t + \varphi)}$$
69.

$$\omega = 2\pi f$$
70.

With ω the radial frequency and f the frequency of the perturbation. The impedance is generally expressed as a complex function $Z(\omega)$.

$$Z(\omega) = \frac{E}{I} = Z_0 e^{j\varphi} = Z_0[cos(\varphi) + j\,sin(\varphi)]$$ 71.

$$j = \sqrt{-1}$$ 72.

The frequency dependence of the impedance is measured on a specific range of frequency in order to reveal the relevant physical properties and chemical processes that take place in the electrochemical cell.

Impedance spectra are generally represented on a complex plot, or Nyquist plot, by reporting the opposite of the imaginary part of the impedance Z'' in function of the real part of the impedance Z'.

$$Z' = |Z|\,cos(\varphi)$$ 73.

$$Z'' = |Z|\,sin(\varphi)$$ 74.

With $|Z|$ the modulus of the impedance. The Nyquist plot for a single frequency is illustrated by **Figure 0.5**.
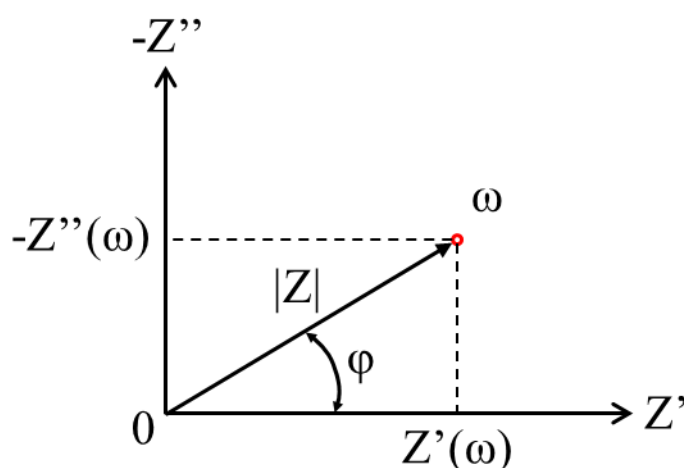
***Figure 0.5.*** *Complex plot or Nyquist plot illustrating the phase shift φ, impedance vector of length |Z| for a single point of angular frequency ω.*

The disadvantage of the Nyquist plot is that the frequencies are not explicit. To alleviate this issue, a few characteristic frequencies are generally indicated on the plot.

2.2. Modelisation of impedance spectra

The study of electrochemical systems by EIS requires the use of equivalent circuits. They are formed with circuit elements (e.g. resistor, capacitor) associated in series or in parallel to

adequately model and quantify the observed phenomena. **Figure 0.6** presents the circuit elements that will be relevant to the study of solid-state FIBs and their corresponding impedance spectra.
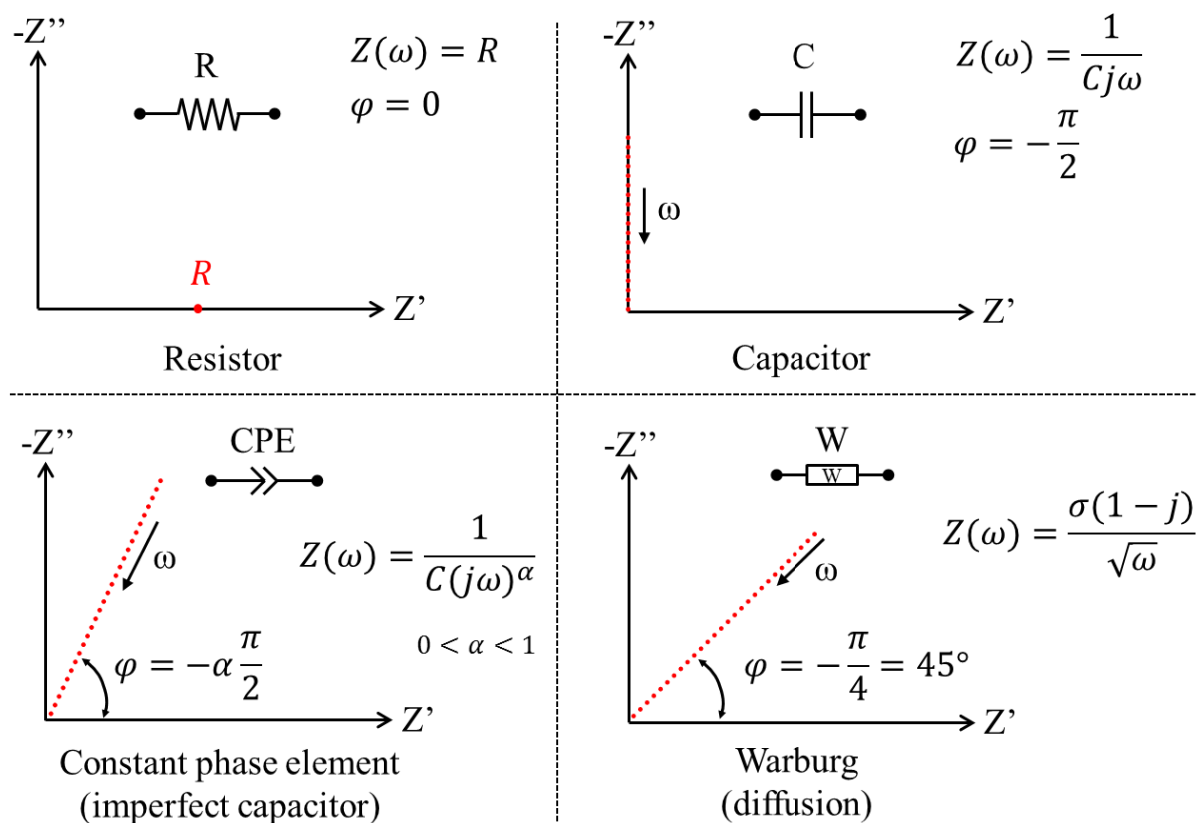

Figure 0.6. *Representation of typical circuit elements used to model impedance diagrams with their corresponding Nyquist plot. The expression of their respective frequency dependent impedance and phase shift is given.*

The most common circuit elements used in the study of solid-state systems are the resistor R (Ω) and the capacitor C (F). They often are at the basis of most equivalent circuits as their association in parallel (R//C or RC) can model the typical impedance response of a solid phase (e.g. electrolyte, surface layer) or diffusion process (e.g. charge transfer when associated with a Warburg impendance W).

The capacitor is used to model an ideal system, which is rarely sufficient to efficiently fit experimental data. The constant phase element (CPE) is of major importance in the practical study of electrochemical systems. Materials or interfaces often present surface roughness or defects inducing a continuous or discrete distribution of time constants around a mean value τ_m. This distribution of time constant is taken into account by the CPE through the α factor.

The Warburg impedance is used to model diffusion processes. It is also of importance in the practical study of electrochemical systems, particularly when charge transfer is involved. It is worth noticing that the Warburg impedance is a particular case of CPE with $\alpha = 0.5$.

Figure 0.7 shows the typical impedance spectra of a solid electrolyte placed between 2 ionically blocking electrodes. R represents the resistance of the electrolyte to the motion of ions, C1 the intrinsic geometrical capacitance of the electrolyte and C2 the capacitive tail due to the screening of charges at the surface of the blocking electrodes.
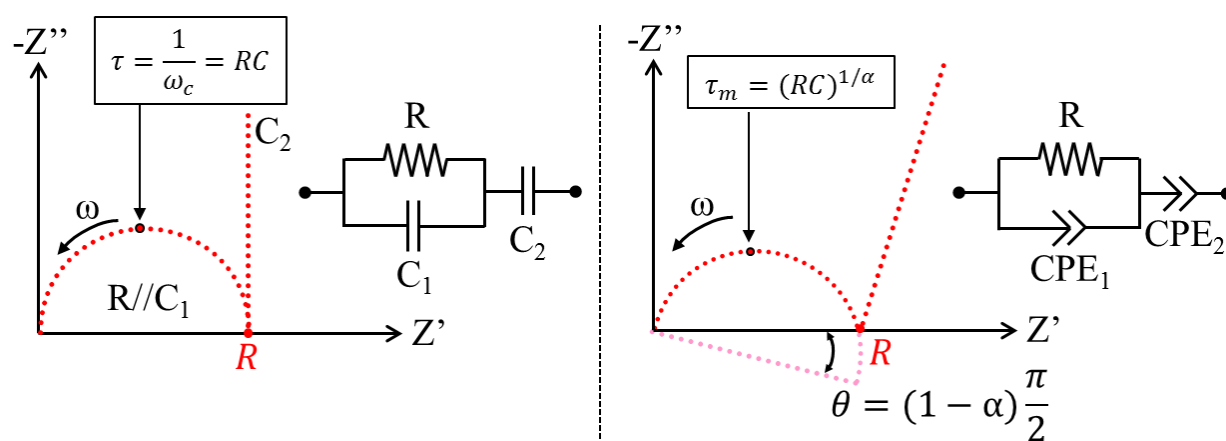
Figure 0.7. Nyquist plots representing the typical impedance spectra of the solid electrolyte placed between two ionicaly blocking electrodes, (left) in ideal conditions and (right) in most experimental conditions.

The association of the R and C (or R and CPE) elements in parallel yield Nyquist plots showing a semi-circle.

In the first example (left), the electrolyte presents a single time constant τ or characteristic frequency ω_c or f_c. The characteristic frequency of a RC circuit is located at the top of the semi-circle (maximum $-Z''$ of the semi-circle) and is related to the time constant of the process/material.

The second example (right) employs CPEs. This is the typical equivalent circuit used to model a polycrystalline solid electrolyte placed between 2 ionically blocking electrodes. In most impedance studies, the electrolyte sample contains defects and its surface is usually rather rough (on the micrometric scale), causing the RC semi-circle and C tail to shift/tilt. The angle θ by which the semi-circle is tilted is related to the width of the relaxation time distribution.[70] The CPE is then used in place of C to obtain a good fit.

The resistance contribution R of the electrolyte determined from the fitting is used to calculate the conductivity σ (S.cm^{-1}) of the electrolyte using the relation:

$$\sigma = \frac{1}{R}\frac{L}{A} = \frac{1}{\rho}$$ 75.

L (cm) is the thickness and A (cm²) the surface of the sample which is in contact with the blocking electrodes. The resistivity ρ (Ω.cm) is the inverse of the conductivity.

Depending on the electrical properties and microstructure of solid electrolytes, their impedance spectra can yield up to 3 semi-circles (3 time constants). Additional semi-circles can be due to the presence of grain boundaries which can give supplementary conduction pathways. A significant electronic conductivity (electrons or holes) in the sample can also bring additional RC time constants of characteristic frequency f_c. The value of f_c then depends on the phenomena responsible for the RC contribution and can be used to determine to assign each semi-circle (**Figure 0.8**). RC contributions present at very low frequencies (μHz) are generally phenomena related to electrode polarization and are often disregarded when the investigator's primary objective is the determination of the electrolyte's electrical properties.
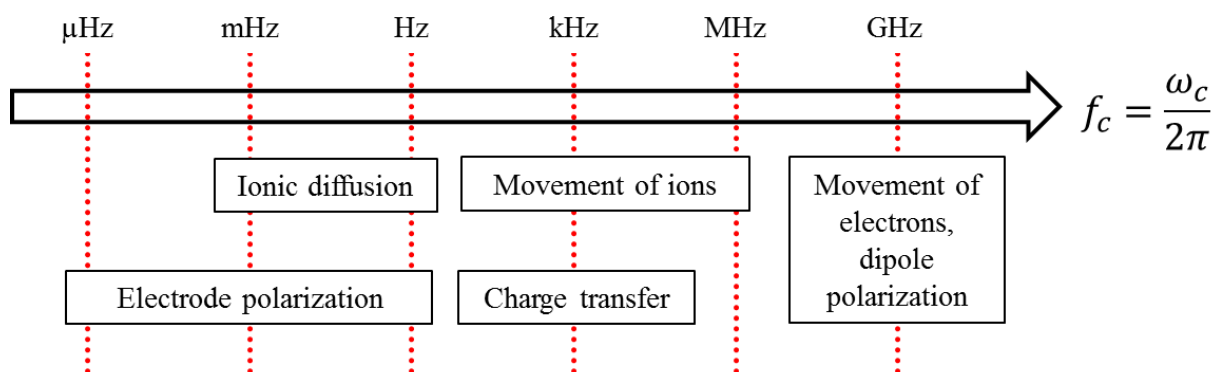
Figure 0.8. Frequency domains of different phenomena related to the study of solid conductors upon application of an electric field. Adapted from the thesis of Chable J.[43]

The presence of a significant electronic conductivity in the sample, as in mixed ionic/electronic conductors (MIEM), is hinted by the fact that the impedance spectra do not present the capacitive tail present at lower frequencies (C$_2$ on **Figure 0.7**). The electronic charges are not blocked at the electrolyte|electrode interface and no screening with ionic charges occur, yielding no capacitive effects.

Another complementary approach to assign the RC contributions observed on the impedance spectrum is the value of the capacitance of the said RC semi-circle.[68] When using CPEs, C

depends on the value of α and cannot be determined directly. It remains possible to calculate the effective capacitance of a RCPE element C_{eff} from the value of the CPE since:

$$(RC_{CPE})^{1/\alpha} = RC_{eff} \qquad\qquad\qquad 76.$$

$$C_{eff} = C_{CPE}^{1/\alpha} . R^{1/\alpha - 1} \qquad\qquad\qquad 77.$$